2016

Novel Terahertz Devices Based on Intersubband Transitions in Quantum Wells

Le Zhao
Lehigh University

Novel Terahertz Devices Based on Intersubband Transitions in Quantum Wells

by

Le Zhao

Presented to the Graduate Committee

of Lehigh University

in Candidacy for the Degree of

Doctor of Philosophy

in

Electrical Engineering

Lehigh University

(September 2016)

DISSERTATION SIGNATURE SHEET

Approved and recommended for acceptance as a dissertation in partial fulfillment of the requirements for the degree of Doctor of Philosophy.

_____
Date

_____
Dissertation Director

_____
Accepted Date

Committee Members:

_____
Prof. Sushil Kumar

_____
Prof. Michael, Stavola

_____
Prof. Jonathan Wierer

_____
Prof. Chao Zhou

Acknowledgment

I would like to express my sincere gratitude to my advisor Prof. Sushil Kumar, for his guidance and continuous support during my doctoral studies. He could always find a way to solve problems that I encountered during various stages of research. Several times, his valuable advice was similar to a light-house in dark ocean whenever I was lost or stuck on a project and was making little progress. Through numerous technical discussions, I benefited from his profound insights on the inner workings of THz QCLs, which provided me a strong foundation to develop my own understanding on the topic. From him, I learned how to solve problems in innovative ways with the use of clever techniques. Besides those I also learned various useful skills which will continue to benefit me in my future career. The skills include, but are not limited to, day-to-day organization of notes, files, and papers, and technical writing skills including elegant and informative ways to generate excellent scientific figures. Most importantly, he is someone whom I have learned to respect immensely, and whose humility and patience has left a lasting impression on my personality.

I would also like to thank my honorable committee members, Prof. Michael Stavola, Prof. Jonathan Wierer, and Prof. Chao Zhou for serving on my dissertation committee. I gained a lot from their knowledge, professionalism, academic experience. I am thankful to them for giving me useful advice during various stages and for their final comments on this thesis.

I also would like to thank Prof. Xiaofei Yang and Prof. Shi Chen from the HuaZhong University of Science and Technology. They taught me my first lessons in scientific research and provided me early encouragement to pursue a Ph.D. degree.

Many sincere thanks also go to my labmates at the QCL lab at Lehigh University for their collaboration, day-to-day discussions, friendship, and support in the past five years. Thanks are due to Sudeep Khanal, ChongZhao Wu, Liang Gao, Yuan Jin and Ji Chen. I would also like to express heartfelt thanks to all my other friends who provided me company at Lehigh University, and without whose support, it would not have been an easy journey. Those include Yaqing Ning, BeiBei Zeng, Yadan Tang, Hongliang Guo, Guanghai Ding, Peng Chen, Mengcen Qian, Chao Zhao, Dan You, Vahid Gholizadeh, Basel Alnajjab, Long Xu, Cong Liu, Cen Lin, Chang Wang, Zhuang Cai, Linlin Fan, Tianyi Luo, Xi Chen, Haolin Ma, Tingting Li, Yushi Tian, Yingyi Zhang, Wei Wang, Yuhua Chen, Xi Luo, Xinyue Shi, Lingzi Pan, Puxin Xu, Zhongqiu Feng. I also would like to acknowledge Mr. Tony Tarng from Texas Instruments for his generous help and advice about my career.

I would like to express my deepest appreciation for my parents and sister for their devotion and endless and unconditional love. They supported me and encouraged me to pursue my dreams, so that I did not have to worry. They have sacrificed a lot in their lives to make sure I succeed, for which I will remain eternally indebted. Finally, I would like to thank my fiancee Xiaofan Xiahou. She brings endless wonders to my life and lifts my sorrows during those hard times. Her love is my enduring source of strength and happiness.

Dedicated to my family who provided me endless love, help, and encouragement.

Contents

List of Figures

Novel Terahertz Devices Based on Intersubband Transitions in Quantum Wells

by
Le Zhao

Abstract

Since the fist demonstration of a terahertz (THz) semiconductor quantum cascade laser (QCL) in 2001, significant progress has been made towards development of THz QCLs. Among all solid-state sources of radiation, THz QCLs are the only type of coherent sources of THz radiation that can provide average optical power output of much greater than 1 mW. THz QCLs could be designed to emit in the frequency range of $\sim 1.2 - 5.4$ THz, and continuous-wave (cw) operation has been realized above the temperature of liquid-Nitrogen. Despite these developments, challenges still remain towards understanding the fundamental physics of intersubband transitions on which QCLs are based, and also towards further development of THz QCLs so that they could be readily used for various applications in THz chemical sensing and spectroscopy. This thesis describes four distinct technical contributions in the area of THz devices based on intersubband transitions in semiconductor superlattices: (a) design and experiments towards development of hole-based intersubband lasers, (b) demonstration of first electrically tunable THz QCLs that could operate at temperatures much greater than that of liquid-Helium, (c) theoretical work towards development of a THz QCL based spectroscopic sensing scheme, and (d) design and preliminary demonstration of a THz quantum-cascade intersubband photodetector utilizing a fast resonant-phonon depopulation scheme for relaxation of photo-excited electrons for high-temperature operation. The key aspects of each of the above contributions are briefly summarized below.

THz intersubband transitions within the conduction band of semiconductor superlattices have been widely studied in the past decade leading to development of THz QCLs. However, considerably few experimental studies have explored the properties of hole-hole intersubband transitions in the valence band. By taking into account the band mixing effect in the valence band, optical transitions between hole-subbands can occur with either the normal-to-plane polarized light or in-plane polarized light. This makes valence band intersubband transitions particularly interesting, because surface-emitting QCLs and normal-incidence THz detectors could potentially be developed. This work develops a density-matrix model of hole transport in p-type

quantum-wells that is suitable for numerical evaluation of intersubband gain or loss. Two hole-based intersubband laser designs are proposed and experimentally investigated. Sequential resonant-tunneling transport is demonstrated, which indicates effective quantum-transport for heavy-holes and is promising toward development of the first hole-based intersubband laser.

Many molecules have very strong characteristic THz rotational and vibrational transitions, and hence could be "fingerprinted" with THz spectroscopy. Such applications ideally require electrically tunable THz sources. For THz QCLs, mode pulling due to Stark-shift of the intersubband gain transition provides electrical tuning at low-temperatures. In this thesis, a new tuning technique based on detuned intersubband absorption is developed, which can efficiently modify electric-susceptibility of the semiconductor medium and thus tune the resonant-frequency of a THz microcavity. Utilizing a coupled microcavity architecture, this approach is then utilized to electrically tune THz QCLs, with a major advantage that such a mechanism works for QCLs operating at much higher temperatures compared to previously demonstrated methods.

Based on theory and finite-element electromagnetic simulations, this thesis also proposes a broadband THz spectroscopic sensing scheme that utilizes on-chip arrays of single-mode QCLs. Such a scheme could be utilized for sensing of the THz refractive-index of solids or liquids in a reflection geometry. No THz detectors or spectrometers are required because the active region of the QCL acts as a non-linear detection medium by itself. The sensing scheme is inherently immune to intensity fluctuations of QCLs' output or other interference effects because it relies on measurement of the shift in the resonant-frequency of the QCLs. Better than parts per million refractive-index-unit (RIU) sensitivities are estimated across the broad frequency range for the proposed sensing scheme.

In addition to high-power radiation sources, compact, low-cost, and high-sensitivity THz photodetectors are also essential components towards realization of THz sensing and spectroscopy systems. This thesis also proposes a novel type of sensitive THz photodetector, the quantum-cascade detector (QCD), which operates at non-zero electrical bias. The design scheme primarily utilizes a superlattice structure that utilizes ultrafast electron-phonon scattering in GaAs/AlGaAs for relaxation of photoexcited electrons in the conduction band, much like that in resonant-phonon depopulation based THz QCLs. Qualitative analysis about the detector's current-noise, responsivity ($\mathcal{R}^*$), and detectivity ($\mathcal{D}^*$) suggest that the newly proposed intersubband photodetector could potentially operate at higher temperatures than existing

zero-bias quantum-cascade detectors, and with higher responsivities. Preliminary experimental results are demonstrated, which show strong photo-response at a temperature of 50 K that is already comparable to the maximum operating temperature of conventional QCDs reported in literature.

Thesis supervisor: Sushil Kumar
Title: Associate Professor

Chapter 1

Introduction

The term "intersubband transitions" has been used to describe unipolar quantum-mechanical transitions between two-dimensional (2D) electronic states in semiconductors that are formed by one-dimensional potential confinement of charge carriers. Low-dimensional electronic systems have been a major topic in semiconductor physics since the 1970s [11], which lead to the concept of "bandstructure engineering". Epitaxial growth techniques allowing accuracy of grown layers at the level of atomic-layer thicknesses in the semiconductors, such as molecular beam epitaxy (MBE) [28], triggered intensive experimental investigation into the properties of such 2D electronic systems. Research activity in the field has resulted in development of novel devices and functionalities that could have never been realized with bulk semiconductors.

The most widely used bandstructure engineered electronic systems are the ones consisting of quantum-wells, which consist of thin semiconductor layers embedded between two similar semiconductor layers but with a with larger bandgap. If the quantum-well thickness is less than the electrons' de Broglie wavelength, then the electronic properties are dominated by quantum-mechanical principles. Depending on the relative band-offset of the two materials, both electrons and holes can be confined in one direction (semiconductor layer growth direction) within conduction-band and

valence-band respectively. One can obtain quantized energy levels (subbands) along the potential confinement direction, and their energy could be tuned by quantum-well width and barrier height. Optical and electronics transitions can take place between the conduction-band and valence-band as well as among quantized levels solely in either the conduction-band or valence-band. The former transition is named as "interband" transitions, and the latter type transitions is called "intraband" or "intersubband" transitions. In this thesis the term "intersubband" is chosen to describe interaction between carriers among discrete quantized energy levels in quantum-wells.

GaAs and AlAs are all Zinc Blende crystal structures and they have almost identical lattice constant ($\sim$ 5.653 Å) allowing one grow high quality arbitrary thick $Al_xGa_{1-x}As$ with aluminum fraction from $0-1$. Compared to other III-V ternary or quaternary compound semiconductors, GaAs is most common and cheapest. Most importantly the epitaxy growth technique for GaAs/AlGaAs multiple quantum-wells on GaAs substrate is very mature. All research included in this thesis are done in GaAs/AlGaAs material system.

Some of the important pioneer works of intersubband transitions in the GaAs/AlGaAs material system are summarized in this paragraph. Quantized states in GaAs/AlGaAs heterostructure was first experimentally observed in 1974 by Dingle et al. through optical absorption spectrum. [35]. Three years later in 1977, Esaki and Sakaki at IBM presented the possibility to use intersubband transitions in quantum-wells for detecting infrared photon. [38] More than 10 years after Dingle's paper, West and Eglash first showed intersubband absorption in GaAs/AlGaAs quantum-wells. [131] This work was referred as the start of intersubband spectroscopy. Besides quantum-wells, intersubband absorption in inversion layer of an GaAs/AlGaAs interface was carried out by Schlesinger at 1983. [114] After middle the 1980s, the number of papers published about intersubband transitions in quantum-wells and semiconductor superlattice had grown dramatically. The research as focus on intersubband

detectors, intersubband lasers as well as nonlinear optical elements. This research has successfully lead to devices which are commercially available now.

1.1 Terahertz radiation and its applications

Terahertz regime of the electromagnetic spectrum lies between microwave and Far-infrared radiation. There is a lack of a strict definition of the lower and upper boundary of THz regime. Typically, it is supposed to extend from about 0.3 THz to around 10 THz (wavelengths from 1 mm to 30μm). Radiation at 1 THz has a period of 1 ps, a wavelength of 300 μm, a wavenumber of 33 cm^{-1} and a photon energy of 4.1 meV. It has long been known that the THz region of the spectrum is ideal in many ways for chemical and biological sensing, imaging, and spectroscopy. [123, 113] Many molecular species have very strong THz rotational and vibrational transitions, (and hence could be fingerprinted with THz spectroscopy.

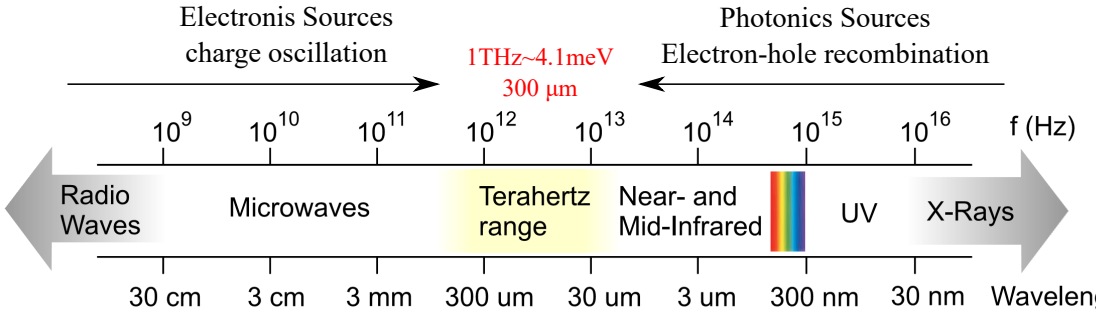

Figure 1.1: Electromagnetic spectrum ranging from radio waves to x-rays. In lower frequency end, electromagnetic wave is generated by charged carrier oscillation while in higher frequency end photon is generated by electron hole recombination. In between is so called "Terahertz gap".

There is a advantage to use Terahertz radiation because they can penetrate a wide variety of nonconducting materials. THz wave can pass through paper, wood, clothing, cardboard, plastic and ceramics. However, metals behave like a mirror for terahertz waves and it is strongly attenuated in water.

When terahertz waves propagate through a nonconducting material, they interact with the material via a number of different mechanisms. These mechanisms involve material bond vibrations and deformations or phonons, and thus are unique to the exact chemical and physical composition of the material. As a consequence, any variations in density, thickness or chemical composition in THz wave optical path affect the THz wave itself in the form of intensity (absorption) and phase (refractive index) variations. Absorption and refractive index information in the THz regime can be used alone or together to reconstruct two- and three-dimensional images of objects that are opaque to visible or infrared light. Additionally, measuring absorption as a function of wavelength enables spectroscopic imaging to map chemical composition. Additionally terahertz radiation is non-ionizing, due to their photon energies that are four orders of magnitude smaller than that of x-rays. This means it is safe for imaging human tissues in vivo.

Figure 1.2 illustrates a THz image for cancer tissue done by Nakajima and et al. [102] The cancer tissue, identified by optical microscope, is indicated on the photographs as hatched areas. The second and the third columns show the images of the absorbance and the refractive index at 1.7 THz, respectively, at the same scale as the photographs.

1.2 Motivation

There are several important requirements that have to be fulfilled to develop low cost high, sensitivity THz sensing and imaging system. Many spectroscopy or sensing technology require radiation frequency to tune across the characteristic absorption linewidth. This enables frequency tuning for high power THz QCLs, while simultaneously achieving an optimum spectral characteristics and beam profile an ideal source. This is another primary limitation for THz applications. Among THz detectors, differ-

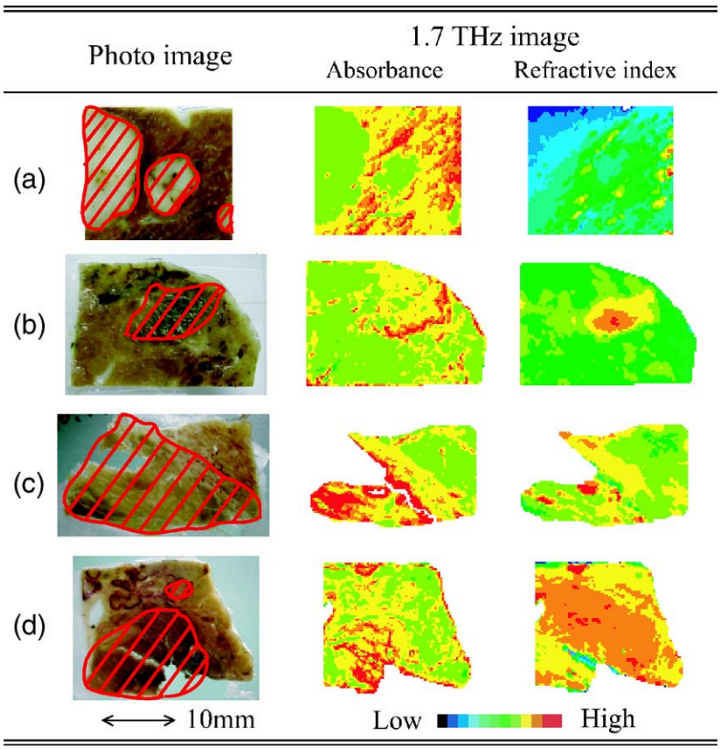

Figure 1.2: Terahertz spectroscopic images of paraffin-embedded cancer tissues have been measured by a terahertz time domain spectrometer. [102]

ent types of bolometers (all working at or below temperatures of liquid-Helium) [4, 5] are typically utilized for sensitive detection of THz radiation. THz detectors working at higher temperatures (such as pyroelectric detectors [1] and transistor or diode-based detectors) are considerably less sensitive, which makes it difficult to develop low-cost THz sensing and imaging systems, even if the THz source power is as large as few milliwatt. The motivation of thesis work is to develop new technologies that can bridge the gap between application requirements and currently limited technology.

1.3 Organization of this thesis

This thesis includes four research areas: (a) development of hole-based intersubband lasers, (b) demonstration of the first electrically tunable THz laser operating at high temperatures, (c) theoretical work of a THz laser based sensing scheme (d) develop-

ment of a THz intersubband photodetector utilizing fast phonon scattering to extract the photo excited electron. Each research area is included in an individual chapter.

Chapter 2 is about developing a hole based intersubband laser. I start from the theoretical aspects mainly divided into two parts. The first part is about the $k \cdot p$ model of valence subband electronics states and a formulas to calculate the hole - LO phonon scattering rate model is derived. The second part describes how to model resonant tunneling processes between hole subbands by applying the density matrix formalism. With these two tools, I proposed two quantum cascade emitter structures utilizing hole intersubband transitions. Finally, pulsed current versus voltage are shown for proposed structure demonstrating effective quantum transport.

Chapter 3 is regarding the topic of electrical tuning of THz QCLs. In this chapter a novel electrical tuning mechanism is proposed and theoretically analyzed. The new tuning technique employs detuned intersubband absorption to introduce a susceptibility change and a coupled optical cavity. A innovative antenna coupled distributed feedback scheme is adopted to obtain favorable far field beam patterns as well as facilitate lateral optical coupling. Experimental results demonstrate tuning of the THz QCL at high operation temperatures cannot be realized by other electrical tuning techniques.

Chapter 4 propose a THz refractive index sensor. The sensor is based on the fact that if an analyte is placed close to THz QCL facet, an impedance mismatch between analyte and its ambient environment will occur. The THz radiation will be reflected at interface and partially coupled back into optical cavity of QCL. This additional feedback will change the resonant frequency. In the proposed sensor scheme another THz QCL behaves like a local oscillator in heterodyne detection. Nonlinear mixing within the QCL active region itself down converts the THz frequency to radio frequency and the frequencies shift of the RF signal is detected by a commercially available spectrum analyzer. The relation between frequency shift to analyte's refrac-

tive index at THz frequency is investigated numerically. Since the proposed sensor works in reflection mode, such a sensor is suitable for sensing the refractive index of materials with high absorption coefficient.

Chapter 5 aims to develop a new type of narrowband THz quantum-well photodetector (QWP) called a quantum cascade detector (QCD), that works similar to the principal of a THz QCL but in a reverse fashion by provide a photocurrent response for absorbed THz photons due to intersubband optical transitions. Very limited early work has been performed previously on THz QCDs . The general understanding of QCL transport has improved considerably since then, which will be utilized for development of significantly improved THz QCDs in this project. We propose a design scheme that utilizes ultrafast electron-phonon scattering in GaAs/AlGaAs superlattices to achieve almost a two orders of magnitude better responsivity than achieved previously for such a detector. Different noise mechanisms as well as how they can be affected by the number of cascaded states are discussed. Experimental result indicate that the proposed detector shows strong photon response at ~ 50 K which is already comparable to existing best performance devices.

Chapter 2

Hole-based THz intersubband lasers

Intersubband transitions in the conduction band of semiconductor superlattice have been under extensive study during the last three decades and lead to applications like Mid-infrared (Mid-IR) [39], and Terahertz (THz) quantum cascade lasers [72],quantum well infrared photo-detectors (QWIPs) [84] and quantum cascade detectors (QCDs) [48]. In contrast, much less work has been done both theoretically and experimentally on hole transport in superlattices as well as intersubband laser based on inter-valence subband transitions. Intersubband transition of holes is particularly interesting and important in both scientifically and practically. Most of the research about hole intersubband transitions has been done in the Si/SiGe material system due to an interest in demonstrating a Si-based laser that has the capability of integration with highly maturated CMOS technology. Intersubband electroluminescence of both Mid-IR and THz photons has been reported in Si/SiGe heterostructures [32, 95]. Intersubband absorption in multiple quantum wells (MQW) and photocurrent measurements have also been explored in the same material system [44]. However Si and Ge's lattice constant have a mismatch of four percents thus the Si/SiGe material system suffers

from challenges related to the growth of high quality pseudo-morphic Si/SiGe superlattice containing hundreds or even thousands quantum wells on various substrates. Compared to Si/SiGe, the GaAs/AlGaAs material system is virtually strain-free since the lattice mismatch between GaAs and AlAs is less than 0.2 percent. MBE epitaxial growth of thick GaAs/AlGaAs superlattices on GaAs substrates is very mature and has been verified by the success of electron-based quantum cascade lasers. Thus, this material system allows researchers separate materials issues from fundamental hole transport properties. Up to today, carbon-doped p-type GaAs/AlGaAs quantum cascade structures had been successfully grown. Absorption and spontaneous emission in the Mid-IR range has been experimentally demonstrated in such structure [97, 98]. Although electron based Mid-IR QCL have been commercialized and THz QCL is the strongest solid state THz source till today. Laser oscillation utilizing hole intersubband transition has not yet to be demonstrated. The hole intersubband transitions are particularly interesting because the polarization of the light emitted is not restricted to normal to quantum well growth direction due to the valence band mixing effect. Moreover, temperature degrade mechanisms of THz QCLs have yet to be clarified [103, 68], the hole based quantum cascade lasers would offer a new tool to study temperature degradation phenomena of THz QCLs.

The purpose of this chapter is develop a design technique which can theoretically analyze quantum transport of holes, and thus predict gain within these semiconductor superlattice. This chapter is divided into five parts. Part I gives overview of the hole subband eigen-energy, dispersion and wavefunction in GaAs/AlGaAs superlattice In part II a theoretical study of LO phonon scattering that accounts for nonparabolicity and anisotropy of valence subband is given. The derivation of the expressions is suitable for numerical evaluation. A simple density matrix in combination with tight binding wavefunction modeling of resonant tunneling of holes in a superlattice is presented in section III. Part IV involves numerical simulation of a THz waveguide for

a p-type superlattice. Finally, two hole based QCL active region designs are presented and analyzed. Experimental results show effective quantum-transport for heavy holes and is promising toward the development of the first hole-based intersubband laser.

2.1 Hole Subbands in GaAs/AlGaAs Superlattices

2.1.1 $k \cdot p$ approximation for hole states in cubic semiconductors

Time independent Schrodinger equation can describe the quantum states of holes in an external potential. In a semiconductor superlattice, layers of two (or more) materials are stacked one by one, and carriers are only confined in the growth direction. Quantum states in a semiconductor superlattice can be found by solving the 1D Schrodinger equation:

$$H(z)\Psi(z) = (-\frac{\hbar^2}{2m}\frac{\partial^2}{\partial\ z^2} + V(z))\Psi(z) = E\Psi(z) \tag{2.1}$$

In perturbation theory, the exact Hamiltonian H is considered as a summation of unperturbed quantum system H_0 whose eigen energy E_n^0 and eigenfunction ϕ_n are known, plus an additional "perturbing" Hamiltonian H'.

$$H = H_0 + H' \tag{2.2}$$

The eigenfunction for Hamiltonian H is expressed in the form of linear superposition of all ϕ_n. H'.

$$\Psi = \sum_n c_n\phi_n, \tag{2.3}$$

where the Coefficient, c_n, can be obtained by substituting 2.3 back to 2.1, multiplying by ϕ_n^* and integrate respect with z. The c_n for a given eigenvalue E then can be

written in matrix form as

$$\|H_0 - IE + H'\|\|c\| = 0 \tag{2.4}$$

where c is a column formed by c_n, I is an identity matrix and each matrix element is

$$H_{nn'} = \langle \phi_{n'} | H_0 + H' | \phi_n \rangle = \int \phi^*_{n'} (H_0 + H') \phi_n dz \tag{2.5}$$

The eigenvalues E are the roots of the determinant, expressed as

$$|H_0 - IE + H'| = 0 \tag{2.6}$$

Determination of the eigenfunctions Ψ and eigenvalues E by reducing the matrix $H_0 + H'$ as a diagonal. Diagonalize matrix $H_0 + H'$ in general can be unrealistic, however the problem is solved by further approximations. The eigen energy is corrected from E^0_m determined from 2.6, and the correction to the wavefunction ϕ_n of a given state m,i.e., the coefficients $c_n(E_m)$, are determined from 2.4.

If the quantum state m is not degenerate then the expression for such a correction can be obtained in serious form. If there are several states $\phi_m, \phi'_m, ...$ corresponding to one eigenenergy E^0_m, it is common first to determine the eigenfunctions and eigenenergies in the zeroth approximation, that is to say all matrix elements in the matrix $H'_{nn'}$ are to vanish except the element $H_{mm'}$, between the function ϕ_m and ϕ'_m corresponding to a given energy. Then high order corrections to the eigenfunction and eigenenergy are found in sequence. However, it is not always possible to accurately evaluate the solution of 2.6 even in the zeroth approximation. This problem may be addressed by constructing a Hamiltonian in the effective mass approximation for degenerate bands or for several close-lying bands.

To solve the problem, the Hamiltonian 2.4 can be partially diagonalized using a unitary matrix S in the sense that S does not contain off-diagonal elements $\overline{H_{ml}}$

between the N given states and the other states $l, l', ...$:

$$\overline{H} = e^{-S} H e^{S} \tag{2.7}$$

The transformation formulated in 2.7 corresponds to a transition from the representation c to the representation $\bar{c}$ defined by

$$\bar{c} = e^{-S} c \tag{2.8}$$

It is shown in [107] the new representation the of correction of matrix element $\overline{H_{mm'}}$ between degenerate state $m, m', ..., m^{(N)}$ up to third order can be expressed as:

$$\begin{aligned}\overline{H_{mm'}} =& H_{mm'} - \sum_{s} \frac{H'_{ms} - H'_{sm'}}{E^0_s - E^0_m} - \frac{1}{2} \sum_{m''s} \frac{H'_{ms} H'_{sm''} H'_{m''m'} + H'_{mm''} H'_{m''s} H'_{sm'}}{(E^0_s - E^0_m)^2} \\ &+ \sum_{ss'} \frac{H'_{ms} H'_{ss'} H'_{s'm'}}{(E^0_s - E^0_m)(E^0_{s'} - E^0_m)}\end{aligned} \tag{2.9}$$

and $H_{mm'}$ is defined as

$$H_{mm'} = E^0_m \delta_{mm'} + H'_{mm'} \tag{2.10}$$

In semiconductors where the most important region in k space is around the extremum point $\overrightarrow{k_0}$. The Luttinger-Kohn representation is most common one used to investigate dispersion in an ideal crystal, especially in regard to the behavior of carriers in slow varying electric and magnetic fields. In Luttinger-Kohn representation the wavevector $\overrightarrow{k}$ is measured from the extremum point $\overrightarrow{k_0}$, i.e., $\overrightarrow{k} = \overrightarrow{K} - \overrightarrow{k_0}$, where $\overrightarrow{K}$ is the wavevector of the point in k space. Instead of Bloch functions

$$\Psi_{nk} = e^{ikz} u_{nk}(z) \tag{2.11}$$

the following functions φ_{nk} are used as a basis

$$\varphi_{nk} = \frac{1}{\sqrt{V_c}} e^{ikz} u_{nk_0} \tag{2.12}$$

where Ψ_{nk_0} is the Bloch function at the extremum point k_0, which is the eigenfunction corresponding to operator H_0 with eigen energy $E_n(k_0)$ and V_c is normalization factor which is the crystal volume. The wavefunction Ψ_{nk} can be expanded in the function φnk in the following way:

$$\Psi_{nK} = \sum_{n'} c_{n'} \varphi_{n'k} \tag{2.13}$$

The coefficient c'_n defines the transformation from the Bloch representation to the Luttinger-Kohn representation. Substituting the expansion of 2.13 into the Schrodinger equation $(H_0 - E)\Psi = 0$, and multiplying φ^*_{nk} integrate with z and applying the relation:

$$H_0(p)e^{ikz} = e^{ikz} H_0(p + \hbar k) \tag{2.14}$$

we can obtain a system of equations

$$\sum_{n'} \left\{ (E_n(k_0) + \frac{\hbar^2 k^2}{2m} - E)\delta_{nn'} + \frac{\hbar k \cdot p_{nn'}}{m} \right\} c_{n'} = 0 \tag{2.15}$$

where $p_{nn'}$ is the momentum matrix element between Bloch function Ψ_{nk_0} and $\Psi_{n'k_0}$ expressed as

$$p_{nn'} = p_{nk_0,n'k_0} = \frac{1}{V_c} \int \Psi^*_{nk_0} \; p \; \Psi_{n'k_0} dr \tag{2.16}$$

For a small volume of k , both $H_1 = \frac{\hbar^2 k^2}{2m}$ and $H_2 = \frac{\hbar k \cdot p}{m}$ terms can be considered as perturbation. We can apply the transformation 2.7, and according to 2.9 this gives, to second order correction, in k.

$$\sum_{n'} \left\{ \left(E_n(k_0) + \frac{\hbar^2 k^2}{2m} - E \right) \delta_{nn'} + \frac{\hbar k}{m} p_{nk_0,n'k_0} + \frac{\hbar^2}{m^2} \sum_{\alpha\beta} \sum_{n'' \neq n} k_\alpha k_\beta \frac{p^\alpha_{nk_0,n''k_0} p^\beta_{n''k_0,n'k_0}}{E_n(k_0) - E_{n''}(k_0)} \right\} c_{n'} = 0 \tag{2.17}$$

In the case of degenerate at k_0 we have to take into account all states which have eigen

energy equals to E_0 into account. We can denote the degenerate states as $i, j = 1, 2, ...m$ where m is the degeneracy of the band at k_0. Now the equation 2.17 has the form

$$\sum_j H_{ij}(k_0, k)c_j = Ec_j \tag{2.18}$$

where Hamiltonian H_{ij} can be expressed as

$$\begin{aligned} H_{ij}(k_0, k) = &\sum_\alpha \frac{\hbar}{m} k_\alpha p^\alpha_{ik_0, jk_0} + \frac{\hbar^2}{2m}\delta_{ij}k^2 \\ &+ \frac{\hbar^2}{2m^2}\sum_{\alpha\beta} k_\alpha k_\beta \sum_{n' \neq i,j} \frac{p^\alpha_{ik_0,n'k_0}p^\beta_{n'k_0,jk_0} + p^\beta_{ik_0,n'k_0}p^\alpha_{n'k_0,jk_0}}{E_n(k_0) - E_{n''}(k_0)} \end{aligned} \tag{2.19}$$

2.1.2 Luttinger-Kohn Basis and Hamiltonian

For III-V semiconductors like GaAs or AlGaAs, the most important region in k space is the center of the Brillouin zone which is known as the Γ point. As a cubic semiconductor with zinc-blende structure, the band is three fold degenerate at the Γ point if spin is disregarded. In order to construct matrix 2.19 one can choose Bloch functions for the top of the valence band X, Y, Z, which transform under operation of the cubic group as x, y, z respectively. Linked to this basis the Hamiltonian is

$$H = \begin{vmatrix} Lk_x^2 + M(k_y^2 + k_z^2) & nk_xk_y & Nk_xk_z \\ Nk_xk_y & Lk_y^2 + M(k_x^2 + k_y^2) & Nk_yk_z \\ Nk_xk_z & Nk_yk_z & Lk_z^2 + M(k_x^2 + k_y^2) \end{vmatrix} \tag{2.20}$$

Where L,M,N are independent constants

$$L = \frac{\hbar^2}{2m} + \frac{\hbar^2}{m^2}\sum_n \frac{|\langle X|p^x|n\rangle|^2}{E_0 - E_n} \tag{2.21}$$

$$M = \frac{\hbar^2}{2m} + \frac{\hbar^2}{m^2}\sum_n \frac{|\langle X|p^y|n\rangle|^2}{E_0 - E_n} \tag{2.22}$$

$$N = \frac{\hbar^2}{m^2}\sum_n \frac{\langle X|p^x|n\rangle\langle n|p^y|Y\rangle + \langle X|p^y|n\rangle\langle n|p^x|Y\rangle}{E_0 - E_n} \tag{2.23}$$

When spin of holes are included the threefold degeneracy at Γ point is doubled and becomes sixfold. The basis function now becomes

$$X_\alpha, Y_\alpha, Z_\alpha, X_\beta, Y_\beta, Z_\beta \tag{2.24}$$

where α and β are the spin function of holes corresponding to positive and negative spin projection. When spin-orbit coupling is neglected, the matrix H relative to basis 2.24 is diagonal as

$$H = \begin{vmatrix} H_1 & 0 \\ 0 & H_1 \end{vmatrix} \tag{2.25}$$

in which H_1 is expressed in 2.20. Spin orbit coupling is expected to remove the sixfold degeneracy of the band at the Γ point for semiconductor with zinc-blende structure. The Schrodinger equation includes spin orbit coupling is

$$H\Psi = \left\{ \frac{p^2}{2m} + V(z) + \frac{\hbar}{4m^2c^2} \left(\sigma \left[\Delta V \times P\right]\right) - \frac{i\hbar}{4m^2c^2} \left(\Delta V \times P\right) - \frac{p^4}{8m^3c^2} \right\} \Psi = i\hbar \frac{\partial \Psi}{\partial t} \tag{2.26}$$

where $p = -i\hbar\Delta$ and σ is Pauli spin matrices. The equation describes a system of two spin components, which refer to two spin state of the holes with different spin projection. One can conclude from 2.26 that the only term which mixes the two spin states of holes is the so-called spin orbit coupling term expressed as:

$$H_{SO} = \frac{\hbar}{4m^2c^2} \left(\sigma \left[\Delta V \times P\right]\right) \tag{2.27}$$

The spin-orbit term 2.27 describes the interaction between the spin and orbit angular momenta in atoms. In this thesis we assume that the spin orbit coupling is dramatically less than the separation to the nearest band (which is the bandgap between conduction band and valence band). This approximation is fairly true for III-V semiconductors like GaAs and AlGaAs. In this case spin-orbit coupling is only considered within the valence band. In the Luttinger-Kohn representation a linear combination of basis 2.24 are chosen to describe wavefunction around the Γ point and to diagonalize the matrix H_{so}. Physically this means

we are solving the system of equations 2.18 with matrix H_{so} instead of H. When solving the equation we obtain 6 solutions. We have a fourfold degenerate wavefunction (heavy hole and light hole) at Γ point and another twofold degenerate wavefunction (split-off hole) separate by Δ_i which is the strength of spin-orbit coupling splitting. The Luttinger-Kohn representation [94] for which H_{SO} 2.27 is diagonal is

$$\Psi_{\frac{3}{2},\frac{3}{2}} = \frac{1}{\sqrt{2}}(X+iY)\alpha \tag{2.28}$$

$$\Psi_{\frac{3}{2},\frac{1}{2}} = \frac{i}{\sqrt{6}}[(X+iY)\beta - 2Z\alpha] \tag{2.29}$$

$$\Psi_{\frac{3}{2},-\frac{1}{2}} = \frac{i}{\sqrt{6}}[(X-iY)\alpha + 2Z\beta] \tag{2.30}$$

$$\Psi_{\frac{3}{2},-\frac{3}{2}} = \frac{i}{\sqrt{2}}[(X-iY)\beta \tag{2.31}$$

$$\Psi_{\frac{1}{2},\frac{1}{2}} = \frac{i}{\sqrt{3}}[(X+iY)\beta + Z\alpha] \tag{2.32}$$

$$\Psi_{\frac{1}{2},-\frac{1}{2}} = \frac{i}{\sqrt{3}}[-(X-iY)\alpha + Z\beta] \tag{2.33}$$

The first four states have angular momentum $J = \frac{3}{2}$ and last two state have angular momentum $J = \frac{1}{2}$. Under the Luttinger-Kohn representation the Hamiltonian H 2.25 undergoes a transformation and becomes:

$$H' = SHS^{-1} \tag{2.34}$$

where S is a unitary matrix transform 2.24 to 2.28 to 2.30 defined as

$$S = \begin{vmatrix} \frac{1}{\sqrt{2}} & \frac{i}{\sqrt{2}} & 0 & 0 & 0 & 0 \\ 0 & 0 & -i\sqrt{\frac{2}{3}} & \frac{i}{\sqrt{6}} & -\frac{1}{\sqrt{6}} & 0 \\ \frac{1}{\sqrt{6}} & -\frac{i}{\sqrt{6}} & 0 & 0 & 0 & \sqrt{\frac{2}{3}} \\ 0 & 0 & 0 & \frac{i}{\sqrt{2}} & \frac{1}{\sqrt{2}} & 0 \\ 0 & 0 & \frac{1}{\sqrt{3}} & \frac{1}{\sqrt{3}} & \frac{i}{\sqrt{3}} & 0 \\ -\frac{i}{\sqrt{3}} & -\frac{1}{\sqrt{2}} & 0 & 0 & 0 & \frac{i}{\sqrt{3}} \end{vmatrix} \tag{2.35}$$

Direct evaluation of the matrix element $H'_{j'm',jm}$ yields the matrix H^{LK}:

$$H^{LK} = \begin{vmatrix} F & H & I & 0 & \frac{iH}{\sqrt{2}} & -i\sqrt{2}I \\ H^* & G & 0 & I & \frac{i(G-F)}{\sqrt{2}} & \frac{i\sqrt{3}H}{\sqrt{2}} \\ I^* & o & G & -H & -i\frac{\sqrt{3}H^*}{\sqrt{2}} & \frac{i(G-F)}{\sqrt{2}} \\ 0 & I^* & -H^* & F & -i\sqrt{2}I^* & -\frac{iH^*}{\sqrt{2}} \\ -\frac{iH^*}{\sqrt{2}} & -\frac{i(G-F)}{\sqrt{2}} & \frac{i\sqrt{3}H}{\sqrt{2}} & i\sqrt{2}I & \frac{F+G}{2}+\Delta & 0 \\ i\sqrt{2}I^* & -i\frac{\sqrt{3}H^*}{\sqrt{2}} & -\frac{i(G-F)}{\sqrt{2}} & \frac{iH}{\sqrt{2}} & 0 & \frac{F+G}{2}-\Delta \end{vmatrix} \tag{2.36}$$

where

$$F = \frac{L+M}{2}(k_x^2 + k_y^2) + Mk_z^2 \tag{2.37}$$

$$G = \frac{F}{3} + \frac{2}{3}(M(k_x^2 + k_y^2) + Lk_z^2) \tag{2.38}$$

$$I = \frac{1}{\sqrt{12}}[(L-M)(k_x^2 - k_y^2) - 2iNk_xk_y] \tag{2.39}$$

$$H = -\frac{N}{\sqrt{3}}(k_yk_z + ik_xk_z) \tag{2.40}$$

where L, M, N are defined in 2.21 to 2.23, and Δ is the spin orbit splitting of the valence band.

2.2 Hole-LO-Phonon Scattering Process

In order to design a laser utilizing intersubband transitions, energy levels and wavefunctions have to be carefully designed to overcome scattering rates and provide population inversion. A proper understanding of inter- (and intra-) subband scattering is essential for the design and understanding of quantum cascade structures. In III-V semiconductors, it has been well established both theoretically and experimentally that polar LO-phonon scattering is the dominant intersubband scattering mechanism for subband separations greater than the LO-phonon energy E_{LO} [43, 54, 126]. For intrawell transitions, these scattering times tend to be less than 1 ps. In THz quantum cascade laser based on electron intersubband transitions, most of the work has been in the GaAs/AlGaAs material system due to its

maturity in terms of MBE epitaxy. Electrons only occupy quantum states very close to Γ point in k space because the quantum cascade structure is very lightly doped and can only operate at cryogenic temperature. Thus, all subbands' dispersion can be safely assumed as parabolic and isotropic with identical curvature, and a universal effective mass can be used for all subbands. This approximation makes the calculation of scattering rate in the conduction band very convenient. In the case of valence band, one has to obtain dispersion relation for all of the subbands involved in hole transport, because of the Bloch functions around the valence band Γ point are less symmetric than that of conduction band Γ point, and hole subband dispersion are generally highly non-parabolic and an-isotropic.

A lot of attempts had already been made to model the hole phonon scattering in quantum wells [64, 9, 63]. Due to computational limitation, all these works make some significant approximation in order to derive either analytical expressions or formula which is over simplified limiting their applicability. In this section a formula calculate hole-polar LO phonon scattering rate which suitable for numerical evaluation is derived based on Fermi's golden rule.

A commercially available $k \cdot p$ solver NEXTNANO3 is used to calculate wavefunction and eigen energy of GaAs/AlGaAS superlattices under slow varying electric fields[15]. In quantum cascade structures holes are only confined in growth direction and can freely move parallel to growth plane. By solving the $k \cdot p$ Hamiltonian, the wavefunction can be expressed as

$$\Psi_{n,k_\rho} = e^{ik_\rho \cdot \rho} \sum_{\nu} f_n^{\nu}(z, k_\rho) \upsilon_{v0}(r) \tag{2.41}$$

where the z direction is defined as the superlattice growth direction and $k_\rho(k_x, k_y)$ and $\rho(x, y)$ are the in plane component of the wave vector and position vector, respectively. $f_n^{\nu}(z, k_\rho)$ is wavefunction envelop along growth direction as a result of the potential different between the GaAs and AlGaAs, as well as applied electric field. In general, the envelop function has in-plane momentum dependency. $\upsilon_{v0}(r)$ is the Brillouin zone center Bloch function. Six Bloch functions, namely $|\frac{3}{2}, \pm\frac{3}{2}\rangle$, $|\frac{3}{2}, \pm\frac{1}{2}\rangle$,$|\frac{1}{2}, \pm\frac{1}{2}\rangle$ corresponding to the heavy hole, light hole and split-off hole, are considered as basis in this case. This Bloch functions are eigen

wavefunctions for the angular momentum operator. Under the 6 *band* $k \cdot p$ scheme, the normalization condition is formulated as

$$\sum_{\nu} |f_n^{\nu}(z, k_\rho)|^2 = 1 \tag{2.42}$$

since all Bloch functions are normalized and orthogonal to each other. During phonon scattering process, both momentum and energy have to be conserved. This requires a relationship between momentum and eigen energy. In quantum cascade structures due to periodic potential confinement in growth direction, momentum in direction k_z is discrete and fixed. Thus k_z can drop from conservation relation and we only need to take care of the in-plane momentum conservation. As shown in 2.36, the eigen energy can solved by finding the determinant of H^{LK} with specified k_x and k_y. If k_x and k_y are over all of the interesting regions in k space, the dispersion of different subbands are then obtained. Figure 2.1 illustrates the conduction band and valence band dispersion different for a single quantum well. Valence subband includes both the heavy hole subband and light hole subband.

Following Fermi's golden rule, scattering rate from an initial state $|i\rangle$ to a final state $|f\rangle$ for an elastic perturbation scatter H' is evaluated by

$$W_{i\to f}^{ems,abs}(k_i, k_f) = \frac{2\pi}{\hbar} |\langle f, k_f, n_{f,q}|H'|i, k_i, n_{i,q}\rangle|^2 \delta(E_f(k_f) - E_i(k_i) \pm E_{LO}) \tag{2.43}$$

where $\hbar$ are reduced Planck's constant, $E_f(k_f)$ and $E_i(k_i)$ are finial and initial state eigen energy corresponding to their momentum. $n_{i,q}$ and $n_{f,q}$ are the crystal phonon modes. The carrier-phonon interaction Hamiltonian takes the form of

$$H' = \sum_{q} [\alpha_q (e^{iq\cdot r} b_q + e^{-iq\cdot r} b_q^{\dagger})] \tag{2.44}$$

where α_q measures carrier-phonon interaction strength, b_q and $b_q^{\dagger}$ are phonon creation and annihilation operator for a phonon mode q. The interaction Hamiltonian is summation over all possible phonon modes. For polar LO phonon the scattering interaction is given by the Frohlich interaction strength in SI units as [133]

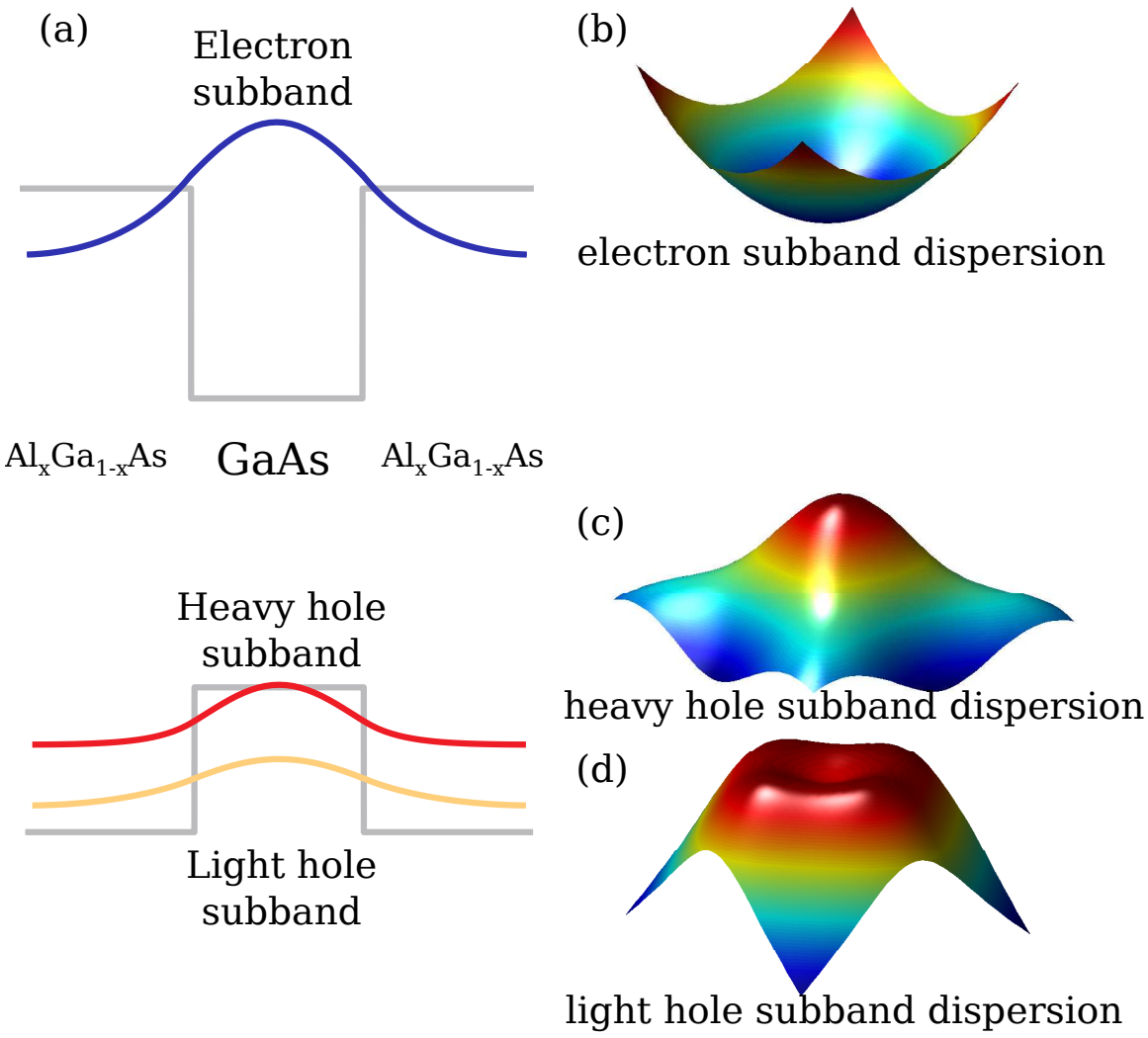

Figure 2.1: In order to illustrate the dispersion difference between conduction band subband and valence band subband, a single quantum well which formed by a 3.4 nm thick GaAs layer sandwiched between two 3.4 nm $Al_{0.2}Ga_{0.8}As$ barrier is used as an example. Luttinger-Kohn Hamiltonian H^{LK} is used for calculating valence band subband dispersion as well as wavefunction. (a) Conduction band and valence band probability density function of the GaAs/ $Al_{0.2}Ga_{0.8}As$ single quantum well. (b) conduction subband (c) heavy hole subband dispersion (d) light hole subband dispersion Calculated relation between in-plane momentum and energy clearly indicate that electron has a parabolic and isotropic dispersion, on the contrary both heavy hole and light hole's dispersion is anisotropic and nonparabolic thus. even within one subband effective mass can not defined.

$$|\alpha(q)|^2 = \frac{E_{LO}}{2}\frac{e^2}{Vq^2}(\frac{1}{\varepsilon_\infty} - \frac{1}{\varepsilon_s}) \tag{2.45}$$

where ε_∞ and ε_0 are the electrical permittivity of the semiconductor at optical frequencies and DC, respectively. The crystal volume is large enough that the phonon mode volume in k space can be considered to be infinitesimal, thus the summation over all phonon modes can convert to an integral. The phonon spectrum available for scattering is approximated to be the phonon spectrum of the GaAs bulk sample. Assumption is also made that the bulk crystal LO phonon is dispersion-less, which is true if 1D infinity atom chain model is applied[69]. Dispersion-less phonon assumption is equivalent to a case regardless of momentum all phonon modes have identical constant energy $E_{LO} = \hbar\omega_{LO}$.

Plugging the hole LO phonon interaction Hamiltonian H' into 2.43 and replace the summation with integral:

$$W_{i\to f}^{ems,abs}(k_i, k_f) = \frac{L^6}{(2\pi)^6}\frac{2\pi}{\hbar}|\iiint dq\alpha(q)M_q|^2\delta(E_f(k_f) - E_i(k_i) \pm E_{LO}) \tag{2.46}$$

We define the matrix element M_q in a standard way and expand out the state vector into independent dimensions

$$\begin{aligned} M_q^{ems,abs} =& \frac{(2\pi)^2}{L^2}\sqrt{n_{i,q} + \frac{1}{2} \pm \frac{1}{2}}\langle\sum_{f=1}^{6} g_v^f(k_f, z)|e^{\mp iq_z z}|\sum_{i=1}^{6} g_v^i(k_i, z)\rangle \\ & \delta(k_{f,x} \pm q_x - k_{i,x})\delta(k_{f,y} \pm q_y - k_{i,y}) \end{aligned} \tag{2.47}$$

We can conclude from 2.47 that the in-plane momentum of the phonon involving in scattering process equals to the in-plane momentum difference between the initial and final states. This requirement can always be fulfilled under dispersion-less assumption. Applying orthogonality of Bloch function we can write the scattering rate between an initial state to a

final state as

$$W_{i\to f}^{ems,abs} = \frac{1}{8\pi}\frac{e^2}{\hbar}(n_{LO}+\frac{1}{2}\pm\frac{1}{2})E_{LO}(\frac{1}{\varepsilon_\infty}-\frac{1}{\varepsilon_s})\int_0^{2\pi}d\theta\int_0^{\infty}k_f dk_f \delta(E_f(k_f)-E_i(k_i)\pm E_{LO})$$
$$\times\int dz\int dz'(\sum_{m=1}^{6}g_m^{(i)^*}(k_i,z)\cdot g_m^{(f)}(k_f,z))(\sum_{n=1}^{6}g_n^{(f)^*}(k_f,z')\cdot g_n^{(i)}(k_i,z'))\frac{1}{q_{||}}e^{-q_{||}|z-z'|} \tag{2.48}$$

where $g_m^{(i,f)}$ and $g_n^{(i,f)}$ are 6 envelop function corresponding to each basis function for Luttinger-Kohn Hamiltonian. Above mentioned formula can be further simplified by taking use of Delta function's property.

$$\int_{\infty}^{\infty} f(x)\delta(g(x))dx = \sum_i \frac{f(x_i)}{|g(x_i)|} \tag{2.49}$$

where x_i satisfying $g(x_i)=0$. Inserting 2.49 into 2.48 the integration over all final states' momentum can be calculated out, now 2.48 becomes

$$W_{i\to f}^{ems,abs} = \frac{1}{8\pi}\frac{e^2}{\hbar}(n_{LO}+\frac{1}{2}\pm\frac{1}{2})E_{LO}(\frac{1}{\varepsilon_\infty}-\frac{1}{\varepsilon_s})\int_0^{2\pi}d\theta\frac{k_{f,s}}{|E'(k_{f,s})|}$$
$$\times\int dz\int dz'(\sum_{m=1}^{6}g_m^{(i)^*}(k_i,z)\cdot g_m^{(f)}(k_f,z))(\sum_{n=1}^{6}g_n^{(f)^*}(k_f,z')\cdot g_n^{(i)}(k_i,z'))\frac{1}{q_{||}}e^{-q_{||}|z-z'|} \tag{2.50}$$

where $k_{f,s}$ satisfying the equation $E_f(k_{f,s})-E_i(k_i)\pm E_{LO}=0$ and $q_{||}$ is in-plane transferred momentum. The total scattering rate between initial subband to finial subband need average all possible initial states in subbands before scattering.

$$\frac{1}{\tau_{i\to f}} = \frac{\int_0^{\infty}dE_k f_i(E_k)W_{i\to f}(E_k)}{\int_0^{\infty}dE_k f(E_k)} \tag{2.51}$$

Formula 2.50 is suitable for evaluate hole phonon scattering rate numerically.

As an example, we will apply the formula to calculate hole phonon scattering rate of a $GaAs/Al_{0.2}Ga_{0.8}As$ single quantum well. The structure is illustrated in Fig.2.1. For each subband probability density function is plotted and shifted corresponding to sub band's

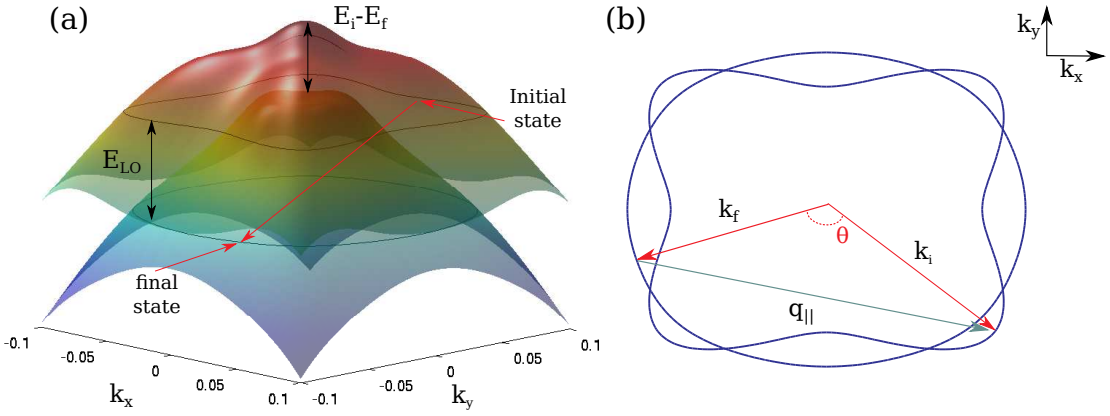

Figure 2.2: Figure 2 illustrate how energy and momentum conserved during hole phonon scattering process in a phonon emission process. (a) $E_i + E_{ki}(k_i) = E_f + E_{kf}(k_f) + E_{LO}$ where E_i and E_f are the eigen energy of initial and final subband at Γ point. $E_{ki}(k_i)$ and $E_{kf}(k_f)$ are kinetic energy of initial and final states. (b) Projection to momentum plane (k_x-k_y plane). Transferred in-plane momentum between initial and final hole states equals to the phonon in-plane momentum involving in scattering process.

eigen energy. At point which in plane wave vector is zero, all off-diagonal terms in H^{LK} are zero leading to each valence subband either "pure" heavy hole or "pure" light hole. Split off hole is not play an role here because in GaAs spin orbit splitting Δ is 0.3 eV while valence band offset between GaAs and $Al_0.2Ga_0.8As$ is only about 0.1 eV. That is to say split off hole is too far away in terms of energy to the region we are interested in for THz quantum cascade structure. In the case of nonzero in plane wave vector, off-diagonal terms in matrix 2.36 are not zero any more resulting in all states are a mixture among all basis of Luttinger-Kohn Hamiltonian. Thus the label heavy hole or light hole do not make physical sense any more. However for the sake of convenience, in this chapter valence subbands are still labeled as either heavy hole (HH) or light hole (LH) based on property of subband at Γ point. Both HH to HH and LH to HH types of hole-phonon scattering are investigated in this section. Permittivity for optical frequency and static Permittivity of bulk GaAs is used when evaluating the Hole-phonon scattering rate. Screening effect is ignored here since THz quantum cascade structure are generally grown with very light

doping ($\sim 5 \times 10^{15}/cm^3$) density. Although wavefunction for each subband depend on in-plane momentum, to balance accuracy and calculation speed we pick a wavefunctions corresponding to a specific in-plane momentum. This assumption is fair since at cryogenic temperature ($\ll 77$ K) with very light doping density only quantum states close to Γ point can be occupied.

When calculating scattering rate lattice temperature is assumed to be 4 K therefore only phonon emission process should be considered. Qualitatively speaking LO phonon scattering rate is proportional to carrier effective mass, local effective mass of holes which is related to second derivative of dispersion in all k space area are heavier than electron effective mass ($0.067\mathrm{m}_0$). The fact explains why HH to HH subband LO phonon scattering rate is generally higher than that of scattering rate between electron subbands. There is also another important difference between conduction and valence subband phonon scattering origin from band mixing effect. The wavefunction overlap between different subband can be measured by following integral

$$O_{mn} = \int dz \int dz' (\sum_{m=1}^{6} g_m^{(i)*}(k_i, z) \cdot g_m^{(f)}(k_f, z))(\sum_{n=1}^{6} g_n^{(f)*}(k_f, z') \cdot g_n^{(i)}(k_i, z')) \tag{2.52}$$

At Γ point, heavy-hole subband envelop function for light hole and split-off hole Bloch function is zero and for light-hole subband only envelop function of light-hole Bloch function is nonzero. Thus at Γ point wavefunction overlap integral between different type valence subbands is zero. Only when in-plane wave vector is non-zero and Luttinger-Kohn Hamiltonian H^{LK} basis start to mix then scattering process between HH and LH subband is allowed. As in-plane wavevector becomes larger band mixing is more significant, thus the scattering between HH and LH subbands is getting more efficient . This phenomenon is illustrated in Figure 2.3 (c)-(f) Two single quantum well structure composed by GaAs/$\mathrm{Al}_{0.2}\mathrm{Ga}_{0.8}$Asare simulated, the first one is correspond to Figure 2.3(c) and (e) layer thickness in monolayer (ML, 2.825Å for GaAs)start from first barrier are 12ML/12ML/12ML where separation between HH1 and LH1 is 34.6 meV; the second one is correspond to Figure2.3 (d) and (f) layer thickness in ML start from first barrier are 12ML/16ML/12ML where separation

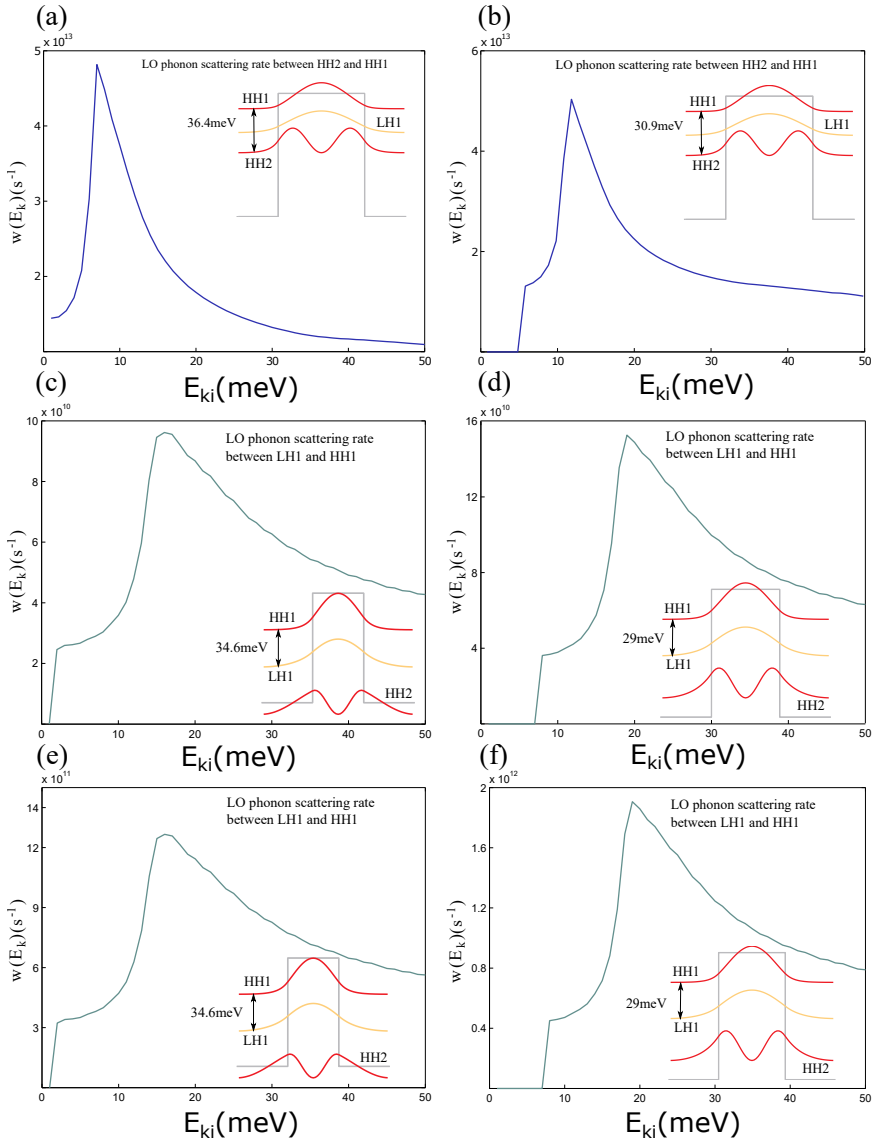

Figure 2.3: Hole-LO phonon scattering rate vs Kinetic energy of Initial state for single quantum well composed by GaAs/$Al_{0.2}Ga_{0.8}As$ (barrier height 101 meV) with different well thickness. (a)(b) HH to HH intra-well hole phonon scattering for subband separation both above (a) and below (b) E_{LO}. Layer thickness is 12ML/25ML/12ML and 12ML/28ML/12ML for (a) and (b) respectively. The raw scattering rate is in the order of 10^{13} which is a direct result of heavier mass of heavy holes. (c)(d) Hole phonon scattering rate between LH1 and HH1. Layer thickness is 12ML/12ML/12ML and 12ML/16ML/12ML for (c) and (d) respectively. Wavefunction for $k_x = k_y = 0.002$Å is used. (e) Wavefunction correspond to inplane momentum $k_x = k_y = 0.008$Å is used when calculating hole phonon scattering between HH1 and LH1 for same structure as (c). (f) Wavefunction corresponding to inplane momentum $k_x = k_y = 0.008$Å is used when calculating hole phonon scattering between HH1 and LH1 for same structure as (d). Phonon scattering rate increase dramatically as in-plane momentum increase and band mixing become significant.

between HH1 and LH1 is 29 meV. As mentioned previous, when calculating hole phonon scattering rate a wavefunction corresponding to a specific in-plane momentum is picked instead of using in-plane momentum depended wavefunction to comprise model accuracy with simulation speed. Figure 2.3(c) (d) are use wavefunction correspond to $k_x = k_y = 0.002$Å while (e) and (f) are use wavefunction correspond to $k_x = k_y = 0.008$Å. Results clearly showing that the choice of wavefunction does not change the curve trend however as band mixing become more significant scattering rate increase dramatically due to scattering rate is proportional to overlap integral.

2.3 Tight-Binding Model to Describe Coherent Tunneling of Holes

In quantum cascade structures, sequential resonant tunneling (RT) is a critical transport mechanism[23]. The effect of resonant tunneling and dephasing are important for describing the transport between two energy states which are weekly couple i.e. tunneling through thick injector barrier[21]. Nonphysical results can be leaded when localization of wavefunction due to dephasing scattering is omitted[22]. Although Non-equilibrium Green function (NGE) simulation have shown some promising results[83], the computationally intensive nature of this method limits its utility of obtaining an intuitive picture of carrier transport in quantum cascade structures. On the other hand density matrix approach offers an easily accessible way describing coherent transport[132], and is successfully used in modeling electron transport in THz QCLs[21, 77]. In a simple coupled quantum well structure as shown in Figure2.4. Only two heavy-hole subbands in each well participated in transport process as holes tunnel from right well to left well under a certain bias. The resonant tunneling process can be descried in either semi-classical or tight binding scheme. Under semi-classical model the entire coupled quantum well is described by a single Hamiltonian. In this picture the hole wavefunction is correspond to a stationary eigenstates. Under resonant bias condition the ground state in one well is aligned with ground state in adjacent well, these

two subbands form a doublet extended through the whole coupled quantum well system with symmetric wavefunction as the lower energy state and anti-symmetric wavefunction as the higher energy state. The tunneling transport is modeled as in and out scattering between the symmetric and anti-symmetric eigen-states by applying Fermis golden rule. Since no coherent oscillatory time evolution among the subband hole populations included, the current density under resonant bias is independent of tunneling barrier thickness in semi-classical scheme.

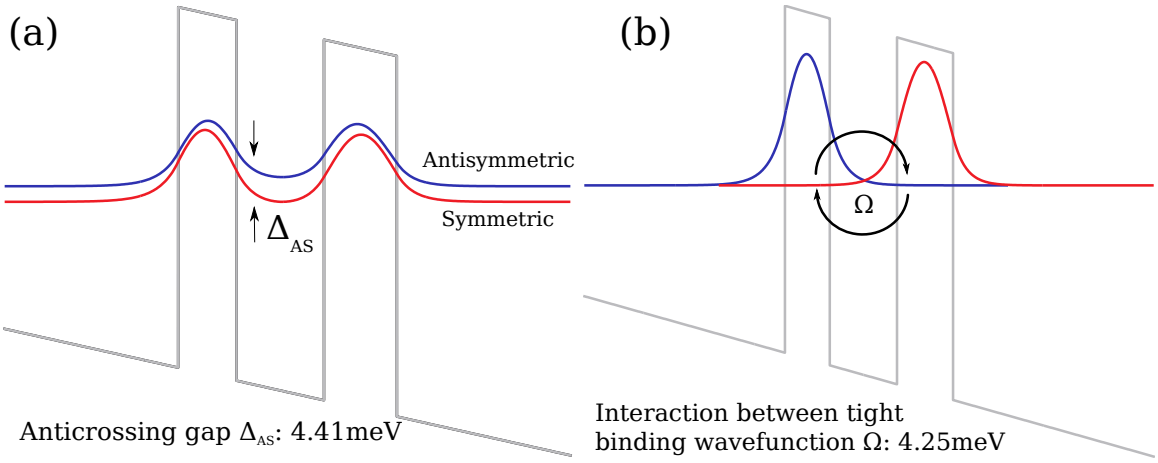

Figure 2.4: Schematic illustrate the difference between semi-classical and tight binding picture of hole tunneling in coupled quantum well. (a) Semi-classical picture of resonant tunneling, wavefunctions are extended. Transport process happened as soon as holes enter either of the states. Tunneling is treated as scattering process between "symmetric" and "anti-symmetric" states. (b) Tight binding picture, hole wave packet is initially localized in right well and oscillate across barrier at Rabi frequency Ω due to interaction between tight binding wavefunctions until the oscillation is dumped by scattering or other dephasing process.

When tight binding approach is applied, the localized basis states is only eigen state of single quantum well instead of coupled quantum well system. The tunneling transport through the barrier takes place via a coherent time evolution thus the hole wave packet oscillates between tunneling barrier at Rabi oscillation frequency Ω. Without pure dephasing Rabi oscillation only damped when holes scattered out from localized eigen state. In contrast with dephasing scattering Rabi oscillation is damped even in absence of intersubband scattering. When pure dephasing time is short enough, Rabi oscillation can be views

as over-damped thus tunneling barrier becomes the bottleneck of current transport. By choosing spatial localized basis one more advantage lies in the fact that such basis are less sensitive to bias which keep the form factors for various intramodule scattering rate kind of independent of applied bias.

Calculating anticrossing from localized wave packet for conduction band was described in [21]. Since effective mass model no longer can be used for hole wave packet, formula (16) and (17) described in [21] need to be modified. To find the localized wavefunctions $\Psi_{TB}(z)$, we consider a single, isolated module under bias, embedded in material with the same composition as the barriers. Mathematically the term "localized" requires probability density decay to zero before it reach boundary of barriers on both side. The wavefunctions in the subsequent (n=1) and previous (n=1) modules are then shifted as

$$\Psi^n_{iTB}(z) = \sum_{m=1}^{6} g^0_m(z - n \cdot l_{mod}); \tag{2.53}$$

where i is subband notation, n is module label. Eigen-energy is shifted as $E_{in} = E_{i0} + nqV_{bias}$, where $q = 1.6 \cdot 10^{19}C$ is the elementary electron charge, l_{mod} is the module length, and V_{bias} is the applied voltage per module. The anticrossing ΔV_{ij} between the tight binding wavefunctions Ψ^m_{iTB} and Ψ^n_{jTB} with respective in-plane momentum $k_{||} = k_i = k_j$ is then determined with a tight binding model similar to equation (16) in [21]:

$$\Delta V_{ij}(k_i, k_j) = \int_{\infty}^{\infty} \sum_{m,n=1}^{6} g_i^{m*}(z) \Delta V(z) g_j^n(z) dz \delta_{k_i,k_j} \delta_{m,n} \tag{2.54}$$

The delta function δ_{k_i,k_j} denotes that in-plane momentum is conserved during coherent resonant tunneling process while the other delta function $\delta_{m,n}$ due to the fact basis functions of Luttinger-Kohn Hamiltonian H_{LK} are orthogonal to each other. Here ΔV_{ij} is the difference of the confining potential between a single module with extended barrier in both ends and

a superlattice composed of a repetition of the module:

$$\begin{aligned}
\Delta V(z) &= V_{barr} - \sum_{m<0} V_{mod}(z - ml_{mod}), \quad z < 0 \\
\Delta V(z) &= 0, \quad 0 < z < l_{mod} \\
\Delta V(z) &= V_{barr} - \sum_{m>0} V_{mod}(z - ml_{mod}), \quad z > l_{mod}
\end{aligned} \tag{2.55}$$

This approach yields a direct estimate of anticrossing gap between two tight binding states. Under six band $k \cdot p$ scheme wavefunction is correspond to certain transverse momenta thus anticrossing gap now has in-plane momentum dependence. When tunneling is happened between two heavy hole subbands anticrossing gap is reduced as in-plane momentum becomes larger and larger. Anticrossing gap change in opposite direction when tunneling is happened between light hole and heavy hole. This phenomena can explained by valence band mixing effect. At Γ point thus transverse momenta is zero, there is no band mixing effect [27]. Delta function $\delta_{m,n}$ in expression 2.54 forbid tunneling between light hole to heavy hole happen. Valence band mixing become more significant as in-plane wave vector become larger, as a consequence amplitude of light hole Bloch function envelops in heavy hole subbands start to become larger. This leads to the fact anticrossing gap between same type of subbands decrease and anticrossing gap between different types of subbands increase. Figure 2.5 illustrate this effect. A coupled quantum well system composed by $GaAs/Al_{0.2}Ga_{0.8}As$ is simulated using commercially available $k \cdot p$ solver NEXTNANO^3 [15]. The layer thickness start from left most barrier is 24ML/24ML/12ML/10ML/24ML. Anticrossing between ground heave hole state in narrow well HH1$'$ and first excited heavy hole state in wide well HH2 is calculated based on formula 2.54. Anticrossing is decreased from 3.15 meV to 0.9 meV when in-plane momentum increasing from 0 to 0.01 Å along 11 direction on transverse momentum plane ($k_x - k_y$ plane). In-plane momentum depended anticrossing between HH1$'$ and ground light hole state in wide well LH1 is illustrated in Figure 2.5 (b). At Γ point there is no interaction between LH1 and HH1$'$ since both subbands are "pure". Tunneling become more strong as in-plane momentum are larger as a result of more significant band mixing. The anticrossing finally reaches 3.9 meV when

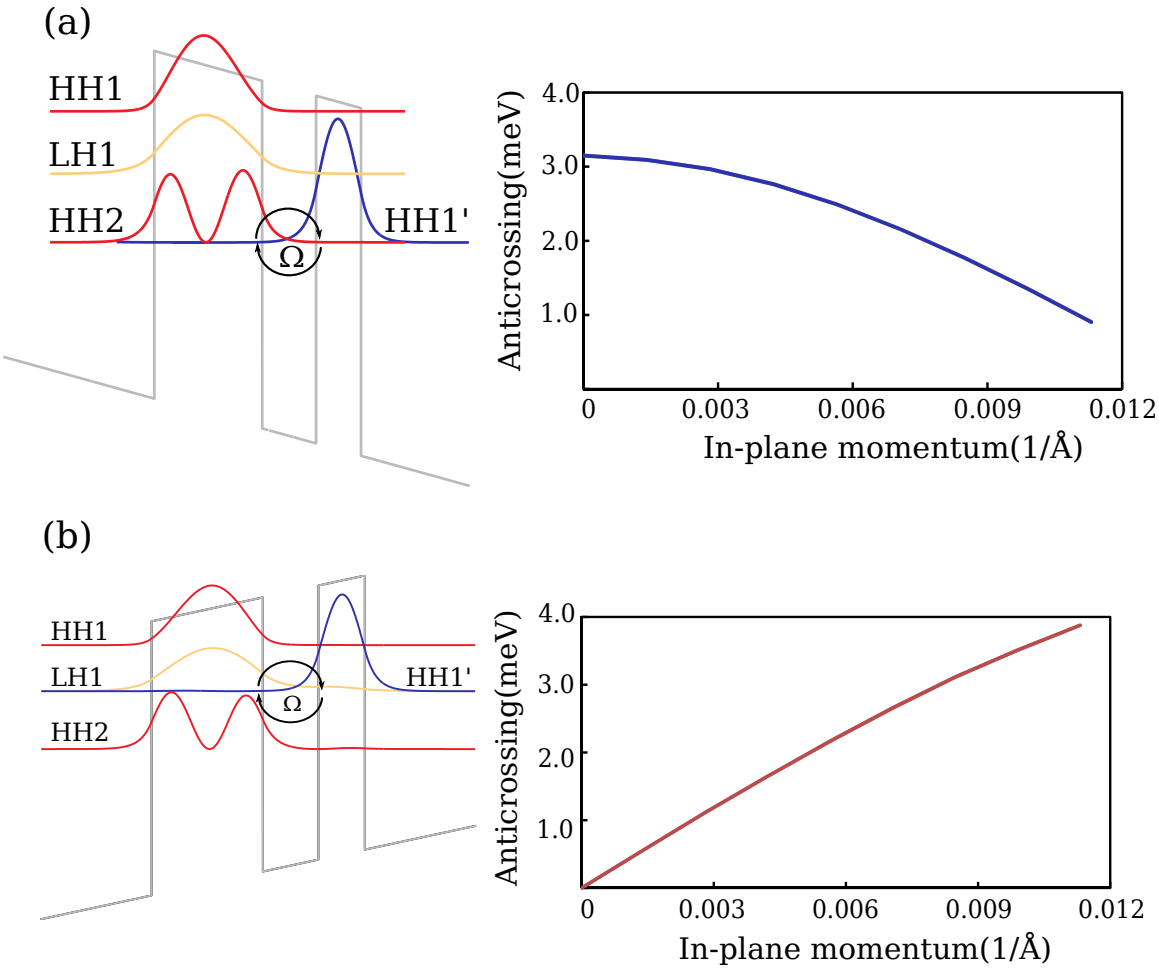

Figure 2.5: Tunneling between heavy hole to heavy hole and light hole to heavy hole in a coupled quantum well system composed by GaAs/$Al_{0.2}Ga_{0.8}As$. The layer thickness start from barrier is 24ML/24ML/12ML/10ML/24ML. (a) Anticrossing gap between HH1′ and HH2 is decreased from 3.15 meV to 0.9 meV when in-plane momentum increasing from 0 to 0.01 Å along 11 direction on transverse momentum plane ($k_x - k_y$ plane). (b) Holes tunneling between LH and HH subbands are forbidden when in-plane momentum is zero. When transverse momentum increase along 11 direction, band mixing becomes more significant at mean while anticrossing between LH1 and HH1′ also becomes larger. The anticrossing reaches 3.9 meV when $k_x = k_y = 0.01$ Å.

$k_x = k_y = 0.01$ Å.

2.4 Hole Transport in GaAs/AlGaAs Superlattices Modeled by Density-Matrix Method

There are several different approaches to understand quantum evolution of a large number of particles. The most straight forward way with physical intuition would be to use Schrodinger picture where all wavefunction for each particle are been tracked. These wavefunctions include all quantum information thus we can easily find macroscopic quantities like optical gain, current density from summing over contributions of all these particles. In Schrodinger picture quantum transport of holes among different states are treated as either radiative transitions or non-radiative transitions of various scattering mechanism. These scattering mechanisms include but not restrict to optical phonon scattering, acoustic phonon scattering, interface roughness scattering, impurities scattering, alloy scattering and carrier-carrier scattering. Rates for all types quantum transitions under certain perturbation are given by Fermi's golden rule.[81] However due to essentially statistical nature of these macroscopic quantities, much of the information from all these wavefunction is averaged out. Since what we interested in are those macroscopic quantities instead of states of all individual particles, it is not necessary and sometimes not practical to gather all wavefunctions.

Density matrix is another more elegant and efficient approach to describe statistical distribution of quantum states in a system[81]. Density matrix formalism allow us treat the properties of large ensembles of carriers without worrying about individual wavefunction. Not only that for phenomenon like resonant tunneling in which phase plays an important role, it allows a phenomenological description of time evolution for phase sensitive interaction. There is a state (Hilbert) space, with orthonormal basis $|\phi_n\rangle$, where n is an integer. If the quantum system is in state $|\psi(t)\rangle$ at time t, the following expression is the expansion in this state space

$$|\psi(t)\rangle = \sum_n c_n(t)|\phi_n\rangle \tag{2.56}$$

where expansion coefficient c_n can be found as $c_n = \langle\phi_n|\psi\rangle$. For an observable operator $\widehat{O}$

, the matrix elements of $\widehat{O}$ in basis $|\phi_n\rangle$ can be written as

$$O_{mn} = \langle\phi_m|\widehat{O}|\phi_n\rangle \tag{2.57}$$

In the same representation, the operator O$\widehat{O}$ can also be written as a matrix form$\overline{\overline{O}}$with the above mentioned elements. For an observable operator the matrix must be a Hermitian matrix. The expectation value of operator $\widehat{O}$ for the system in state $|\psi(t)\rangle$ becomes

$$\langle\widehat{O}\rangle(t) = \langle\psi(t)|\widehat{O}|\psi(t)\rangle = \sum_n \sum_m c_m^*(t)c_n(t)O_{mn} \tag{2.58}$$

We can define density operator in the form of projection operator as following [142]

$$\rho(t) = |\psi(t)\rangle\langle\psi(t)| \tag{2.59}$$

The density operator can be explained as probability distribution in a system. For an ensemble of particles, the density matrix element can be defined as ensemble average.[81]

$$\rho_{mn}(t) = \langle\phi_m|\rho(t)|\phi_n\rangle = \langle c_m^* c_n\rangle \tag{2.60}$$

The diagonal term of density matrix element ρ_{ii} is a real number and describe the probability of finding the system in state $|i\rangle$. This number is proportional to probability density of the state. The off-diagonal term ρ_{ij} describe the polarization interaction between states $|i\rangle$ and $|j\rangle$. Since the total population density is conserved thus [142]

$$Tr(\rho) = \sum_{i=1}^{N}(\rho_{ii}) = 1 \tag{2.61}$$

There is another important property of density matrix the square of off-diagonal term is not larger than the product of corresponding diagonal term. This property is named as Schwartz inequality.

$$\rho_{ii}\rho_{jj} \geq |\rho_{ij}|^2 \tag{2.62}$$

Equality correspond a case the state is "pure", physically pure means the states is described by a single wavefunction. This "pure" state is not necessary a single carrier instead it can also describe an ensemble of particles. Naturally speaking inequality of equation 2.62 refer to a "mixed " state which in general can be broken up into

$$\rho^{mixed} = \sum_i |\psi_i\rangle\langle\psi_i| \tag{2.63}$$

A mixed state cannot describe by a single wavefunction instead it consist of an ensemble of independently evolution pure state. Actually this fact can be understand as a mixed state is ensemble of ensembles. In this picture, dephase case the carrier remove from its original pure state and subsequently add to a mixed state in a constituent of pure states, with a phase have no relation of its original phase. Mathematically, the net effect is total population remain unchanged as 2.61 while average coherence ρ_{ij} decrease. We need equation of motion to capture time evolution of density operator thus the population distribution and coherence. This equation of motion (Quantum Liouville) can be written as [20, 81],

$$\frac{\partial \rho}{\partial t} = \frac{i}{\hbar}[H, \rho] \tag{2.64}$$

where $H = H_0 + H'$, H' represent a perpetuation. The density matrix, unlike the state vector, does not have phase ambiguity and it remains the same under a phase transformation $|\psi(t)\rangle \rightarrow e^{i\theta}|\psi(t)\rangle$. In our case H' only consist difference of the potential ΔV_{TB} due to the coupling between localized states in one module of quantum cascade structure to the state in adjacent module. Ideally 2.64 can be rewrite in the way its expression is formally identical to the one calculation wavefunction.[21]. Considering right hand side of equation 2.64 that density matrix can undergo a transformation and we can define a linear operator $\mathcal{L}$

$$\frac{\partial \rho}{\partial t} = \frac{i}{\hbar}\mathcal{L}\rho \tag{2.65}$$

where $\mathcal{L}$ is called Liouville operator. The result when Liouville operator operate on density

matrix should be identical to the commutation relation $[H, \rho]$. Thus $\mathcal{L}$ is defined as [20]

$$\mathcal{L}_{ij,mn} = H_{im}\delta_{jn} - H^*_{jn}\delta_{im} \tag{2.66}$$

$\mathcal{L}$ is a super-operator with dimension $N^2 \times N^2$ and ρ has dimension N^2. Dimension of $\mathcal{L}$ scales with fourth power of N as a consequence matrix $\mathcal{L}$ easily becomes too large to calculate. Simplifications and approximations are discussed later in this section. Making this full quantum description in combine with semi-classical picture lead to a model vastly simplified for numerical implementation. Note that 2.65 has the same form as time dependent Schrodinger equation the fact enable us apply same formalism in both Hilbert (Schrodinger) and Liouville (density) space. This analogy may allow us apply the technique developed in Hilbert space to Liouville space.

Up to now only we are only consider coherent time evolution of a carrier wavefunction for H_0 with perturbation Δ_{TB} defined in 2.55 representing interaction between neighboring modules. Interaction is forbidden between states with different in-plane momentum in this approximation[59]. Transport between states with different in-plane momentum are treated independently as semi-classical scattering mechanism. A full quantum descriptions like nonequilibrium green functions (NEGF) of the many interactions as phonon scattering, carrier-carrier scattering *et al.* are computational intensive and time consuming[128, 129]. Thus it it more convenient to describe these scattering mechanism in semi-classical way which is Fermi's golden rule. In general injector barrier and collector barrier is much thicker than other barrier thickness in THz QCL designs. Thus interactions across injector barrier and collector barrier are much weaker and more sensitive to various dephasing process than other interaction within one module. Only these two interaction is describe by 2.65.

The scattering affect the transport of the carriers and distribution of population with a scattering time T_1. In addition to this scattering time, the effect from all other mechanism which can affect phase are include in one phenomenological "pure dephasing " time T_2 without changing population. More specifically, this "pure dephasing" time accounts for effect of the environment in system on the electron as well as scattering events that are not

explicitly included in the simulation model. Both "pure dephasing" and scattering time contribute to the dephasing time $\tau_{dephase}$ [20, 77]

$$\frac{1}{\tau_{dephase}} = \frac{1}{2T_1} + \frac{1}{T_2} \tag{2.67}$$

The factor 2 for the contribution of relaxation scattering due to the fact T_1 is probability decay rate reduce with $\rho_{ii} \propto |\rho_{ij}|^2$, thus $\rho_{ii} \propto e^{-t/T_1} \rightarrow \rho_{ij} \propto e^{-t/2T_1}$ on the contrary T_2 describes relaxation of coherence ρ_{ij} which proportional to the amplitude of the oscillation ($\rho_{ij} \propto e^{-t/T_2}$). In the equation of motion 2.65 scattering and pure dephasing add additional terms to the expression for ρ_{ii} and ρ_{ij}. Incorporate these terms in the density matrix formalism with another super-operator denote as $\mathcal{F}$.[20]

$$\frac{\partial \rho_{\mathrm{ij}}}{\partial \mathrm{t}} = \sum_{m,n} \left(\mathcal{L}_{ij,mn} + \mathcal{F}_{ij,mn}\right) \rho_{mn} \tag{2.68}$$

$$\mathcal{F}_{ij,mn} = -\frac{1}{2}\left(\gamma_i + \gamma_j\right)\delta_{im}\delta_{jn} - \Gamma_{ij}^{pure}\gamma_{im}\gamma_{jn}, \qquad i \neq j \tag{2.69}$$

$$\mathcal{F}_{ii,jj} = \gamma_{ji}(1 - \delta_{ij}) - \gamma_i\delta_{ij} \tag{2.70}$$

where γ_i and γ_j correspond to the total scattering rates out of i and j levels, γ_{ij} is the net scattering rate from level j to i and Γ_{ij}^{pure} is pure dephasing time $= T_2^{-1}$ for the coherence ρ_{ij}

2.5 Momentum-matrix element from $k \cdot p$ model

This chapter closely follows Helm's chapter [57]. Optical transitions' strength can be measured by momentum matrix elements. During optical transitions, in plane momentum should be conserved. Thus, matrix element of momentum operator between the complete wavefunctions Ψ_{nk} can be expressed as

$$\frac{\hbar}{m_0} e \cdot p_{nn'} = \langle \Psi_{nk} | \frac{\hbar}{m_0} e \cdot p | \Psi_{n'k} \rangle \tag{2.71}$$

Due to analogy of the expression $e \cdot p$ with $k \cdot p$, the matrix elements can be expressed through the Luttinger-Kohn Hamiltonian elements. Elements in Luttinger-Kohn Hamiltonian can take the form:

$$H^{LK}_{\nu\nu'} = E_{\nu 0}\delta_{\nu\nu'} + \sum_{\alpha,\beta} D^{\alpha\beta}_{\nu\nu'} k_\alpha k_\beta \tag{2.72}$$

where $D^{\alpha\beta}$ plays the role of an inverse effective-mass tensor. The value of $D^{\alpha\beta}$ is related to widely used Luttinger parameter γ_i. Luttinger parameter of III-V semiconductors can be found in literature.[29] Express momentum matrix element in terms of $D^{\alpha\beta}$ yields:

$$\frac{\hbar}{m_0}\langle u_{\nu k}|e \cdot p|u_{\nu' k}\rangle = \sum_{i,j}(D^{ij}_{\nu\nu'} + D^{ji}_{\nu\nu'})e_i k_j \tag{2.73}$$

where i,j denote x, y or z directions. Assuming the semiconductor growth direction is along z direction, separating terms containing k_z which actually becomes $-i\frac{d}{dz}$ from the rest, it can be shown that equation 2.71 can be written in the form

$$\frac{\hbar}{m_0} e \cdot p_{nn'} = e \cdot \sum_{\nu\nu'}(I_{\nu\nu'}Q^{nn'}_{\nu\nu'} + J_{\nu\nu'}R^{nn'}_{\nu\nu'}) \tag{2.74}$$

where the indices ν and ν' go over all basis and n, n' indicate the subbands. $Q^{nn'}_{\nu\nu'}$ and $R^{nn'}_{\nu\nu'}$ are related to envelop of each Bloch function. They can be expressed as:

$$Q^{nn'}_{\nu\nu'} = \int dz F^*_\nu(n, k_{||}, z)F_{\nu'}(n', k_{||}, z) \tag{2.75}$$

and

$$R^{nn'}_{\nu\nu'} = \int dz F^*_\nu(n, k_{||}, z)(-i\frac{d}{dz})F_{\nu'}(n', k_{||}, z) \tag{2.76}$$

In GaAs, spin-orbit interaction Δ is about 0.3eV which is far away enough from heavy hole and light hole subbands, thus, it is fair to calculate momentum matrix according to four valence bands (heave hole and light hole, each band have double degeneracy due to spin). Now momentum matrix element can be expressed in matrix form containing Luttinger parameter γ_i
x polarization

	HH(3/2)	HH(-3/2)	LH(1/2)	LH(-1/2)
HH(3/2)	$\hbar k_x(\gamma_1+\gamma_2)Q^{nn'}$	0	$-\sqrt{3}\hbar\gamma_3 R^{nn'}$	$-\sqrt{3}\hbar(\gamma_2 k_x - i\gamma_3 k_y)Q^{nn'}$
HH(-3/2)	0	$\hbar k_x(\gamma_1+\gamma_2)Q^{nn'}$	$-\sqrt{3}\hbar(\gamma_2 k_x + i\gamma_3 k_y)Q^{nn'}$	$\sqrt{3}\hbar\gamma_3 R^{nn'}$
LH(1/2)	$-\sqrt{3}\hbar\gamma_3 R^{nn'}$	$-\sqrt{3}\hbar(\gamma_2 k_x - i\gamma_3 k_y)Q^{nn'}$	$\hbar k_x(\gamma_1-\gamma_2)Q^{nn'}$	0
LH(-1/2)	$\sqrt{3}\hbar(\gamma_2 k_x - i\gamma_3 k_y)Q^{nn'}$	$\sqrt{3}\hbar\gamma_3 R^{nn'}$	0	$\hbar k_x(\gamma_1-\gamma_2)Q^{nn'}$

z polarization

	HH(3/2)	HH(-3/2)	LH(1/2)	LH(-1/2)
HH(3/2)	$\hbar(\gamma_1 - 2\gamma_2)R^{nn'}$	0	$-\sqrt{3}\hbar\gamma_3(k_x + ik_y)Q^{nn'}$	0
HH(-3/2)	0	$\hbar(\gamma_1 - 2\gamma_2)R^{nn'}$	0	$-\sqrt{3}\hbar\gamma_3(kx - ik_y)Q^{nn'}$
LH(1/2)	$-\sqrt{3}\hbar\gamma_3(kx - ik_y)Q^{nn'}$	0	$\hbar(\gamma_1 + 2\gamma_2)R^{nn'}$	0
LH(-1/2)	0	$\sqrt{3}\hbar\gamma_3(kx + ik_y)Q^{nn'}$	0	$\hbar(\gamma_1 + 2\gamma_2)R^{nn'}$

The terms containing $J_{\nu\nu'}R^{nn'}_{\nu\nu'}$: $R^{nn'}_{\nu\nu'}$ is expressed in 2.76. It is nonzero only when two envelops have different parity. All these terms do not depend on in-plane momentum (k_x or k_y), thus, they are allowed at Γ point. These terms are similar to "usual" intersubband transitions, like in the conduction band. The terms containing $I_{\nu\nu'}Q^{nn'}_{\nu\nu'}$: overlap integral $Q^{nn'}_{\nu\nu'}$ is defined in 2.75. Thus, these terms are non zero when envelops have identical parity. Furthermore they are proportional to in-plane momentum, and thus, only allowed for nonzero $k_{||}$

2.6 Design of a Hole-Based THz Intersubband Laser

Terahertz QCLs with resonant-phonon depopulation and resonant-tunneling injection show superior performance when designed for emission, typically above $\sim$ 2.5 THz for conduction band[74]. In this type of RTRP design, electron LO phonon scattering at sub-picosecond timescales and resonant tunneling for both injection and depopulation are the two dominant electron-transport mechanisms through the quantum cascade structure. The highest operating temperature of $\sim$ 200K was recently realized for a 3.2 THz QCL [41]. This experimental result is a good proof that RTRP design strategy result in robust THz QCL with high optical gain for electrons.

In order to take full use of experience people gained during the process developing high performance electron based THz quantum cascade laser as well as reduce complexity for modeling we choose resonant tunneling injection and resonant phonon depopulation scheme. There are several import design considerations firstly although bound to continuum design leads to lower threshold current density, resonant tunneling injection resonant phonon depopulation design showing supreme temperature per-

formance among all designs [134]. Since in semiconductor superlattice , non-radiative lifetime is much shorter than spontaneous lifetime even shorter than stimulated lifetime when above threshold, thus threshold current density no longer a good figure of merits when comparing optical gain versus loss. On the contrary maximum operation temperature becomes better quantity when comparing gain for different active region design. Hence RTRP design offers higher optical gain as well as more robust temperature performance.

Due to more complex situation in valence band, first hole based intersubband design desire a structure as simple as possible. The most simplest QCL design need three subbands and two quantum wells to individually engineer separation among these subbands [75]. There is another type of QCL design only have three subbands involved in electron quantum transport namely "ground state QCL" [24] Thus attempts to design valence band intersubband laser similar to two well QCL and ground state QCL are made. The simplicity of band diagram make it much more convenient to model quantum transport and analysis experimental result.

Although hole intersubband transition between different type hole subbands offers new physical perspective, tunneling between light hole and heave hole is forbidden at Γ point. It is very difficult to determine in-plane momentum of holes at cryogenic temperature in real device, thus both upper and lower radiative subbands are chosen to be heave hole subband. There is another reason why light hole is not been chosen. Valence band diagram showing that light hole subband is less confined due to smaller "effective" mass. Hence, light hole is more easier to escape to continuum states. This only contribute to parasitic current channel and reduce optical gain.

2.6.1 Valence-band two-well QCL design

We design a valence band two well QCL by resonant tunneling injection and intrawell phonon depopulation [146]. While unlike conduction band two well QCL, there will

be always exist a light hole subband between HH2 and HH1. The effect of light hole subband is twofold. First, since energy spacing between LH1 and HH1 is much smaller than LO phonon energy phonon depopulation from LH1 is less efficient than that from HH2 this leads some holes will stuck in LH1 subband. Second, light hole subbands are not confined in one module therefore scattering between subband in different module should be considered.

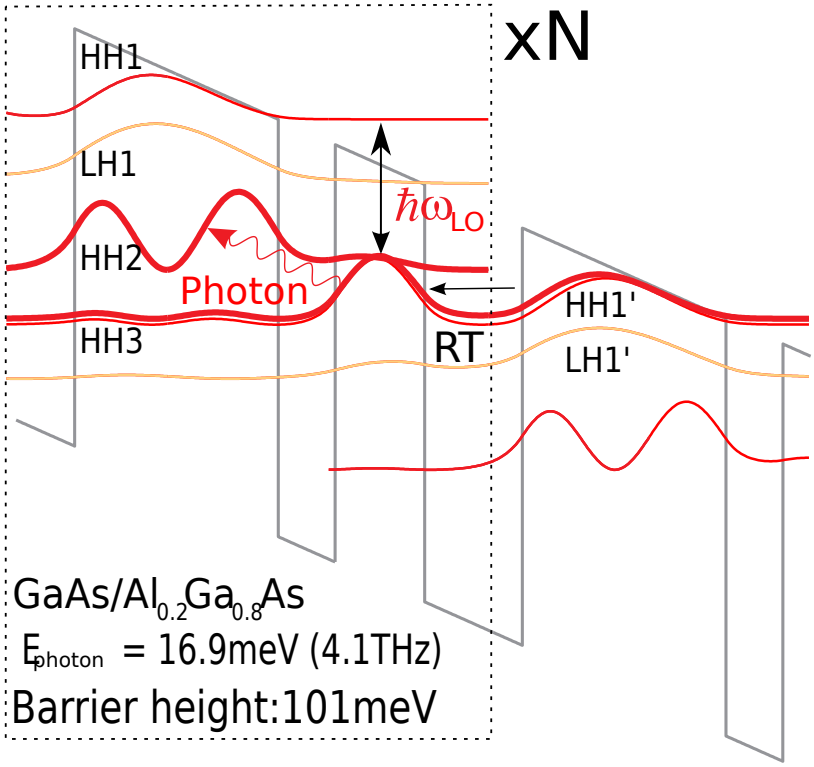

Figure 2.6: Valence band diagram of two well (four level) QCL design utilize GaAs/$Al_{0.2}Ga_{0.8}As$. Holes are injected into upper level HH3 by resonant tunneling, optical gain is due to radiative transition between HH3 and HH2 while depopulation from lower lasing level HH2 by direct hole-LO phonon scattering to HH1 to complete transport process in cascade scheme. The layer thickness start from injector in monolayer(ML) is 12/ 27 /5/ 11. At design bias 32 kV/cm the spacing between HH2 and HH1 is 31.2 meV and $E_{photon} = 16.9$ meV (4.1 THz)

Figure 2.6 shows the designed bandstructure at HH1-HH3 resonant bias. The radiative transition strength is proportional to square of momentum matrix element [142]. Calculation of momentum matrix element is implemented by follow-

ing the way in reference [141, 25, 122]. A value of momentum matrix element of 2.55×10^{-26} kg $\cdot$ J is chosen to keep the HH3 to HH2 transition diagonal while make sure the coupling between lasing levels are strong enough. The following values are obtained for subbands lifetime only attributed to hole-LO phonon scattering: $\tau_{HH3-HH1} \sim 0.8$ ps,$\tau_{HH2-HH1} \sim 0.12$ ps, $\tau_{HH3-HH2} \sim 4.5$ ps and $\tau_{LH1-HH1} \sim 0.7$ ps. In terms of predict optical gain in hole based QCLs, DM is used to calculate hole distribution for each subbands. Label the four subbands which are involved in transport as $1'$, 2, 3, 4 for HH1, LH1,HH2,HH3 respectively. Expanding equation 2.68 to 2.70 we then obtain following equations:

$$\frac{\mathrm{d}}{\mathrm{d}t}\begin{pmatrix} \rho_{1'1'} & \rho_{1'4} & \rho_{1'3} & \rho_{1'2} \\ \rho_{41'} & \rho_{44} & \rho_{43} & \rho_{42} \\ \rho_{31'} & \rho_{34} & \rho_{33} & \rho_{32} \\ \rho_{21'} & \rho_{24} & \rho_{23} & \rho_{22} \end{pmatrix} = -\frac{i}{\hbar}\left[\begin{pmatrix} E_{1'} & -\hbar\Omega_{1'4} & -\hbar\Omega_{1'3} & 0 \\ -\hbar\Omega_{1'4} & E_4 & 0 & -\hbar\Omega_{42} \\ -\hbar\Omega_{1'3} & 0 & E_3 & -\hbar\Omega_{32} \\ 0 & -\hbar\Omega_{42} & -\hbar\Omega_{32} & E_2 \end{pmatrix}, \bar{\bar{\rho}}_{(1',4,3,2)}\right]$$
$$+\begin{pmatrix} \frac{\rho_{22}}{\tau_{21}}+\frac{\rho_{33}}{\tau_{31}}+\frac{\rho_{44}}{\tau_{41}} & -\frac{\rho_{1'4}}{\tau_{d14}} & -\frac{\rho_{1'3}}{\tau_{d13}} & -\frac{\rho_{1'2}}{\tau_{d12}} \\ -\frac{\rho_{41'}}{\tau_{d14}} & -\frac{\rho_{44}}{\tau_{43}}-\frac{\rho_{44}}{\tau_{42}}-\frac{\rho_{44}}{\tau_{41}} & -\frac{\rho_{43}}{\tau_{d43}} & -\frac{\rho_{42}}{\tau_{d42}} \\ -\frac{\rho_{31'}}{\tau_{d13}} & -\frac{\rho_{34}}{\tau_{d43}} & -\frac{\rho_{33}}{\tau_{31}}-\frac{\rho_{33}}{\tau_{32}}+\frac{\rho_{44}}{\tau_{43}} & -\frac{\rho_{32}}{\tau_{d32}} \\ -\frac{\rho_{21'}}{\tau_{d12}} & -\frac{\rho_{24}}{\tau_{d42}} & -\frac{\rho_{23}}{\tau_{d32}} & -\frac{\rho_{22}}{\tau_{21}}+\frac{\rho_{33}}{\tau_{32}}+\frac{\rho_{44}}{\tau_{42}} \end{pmatrix} \tag{2.77}$$

Equation 2.77 only include intramodule scattering time as conduction band case. However it is very obvious in figure 2.6 that LH1 wavefunction is extended across two module. One consequence from extended wavefunction is light hole is very easy escape to continuum, thus this is a carrier leakage channel. However this mechanism is neglected in current model, this is due to the fact that cascade structure require conservation of particles $\sum_{i=1}^{4} \rho_i = 1$. This escape break the conservation thus difficult

include in current model. Second consequence of extended wavefunction is offer anther transport channel than resonant tunneling between two modules. This effect can included in the model by adding inter-module scattering terms to second line of equation 2.77. These inter-module scattering can either change carrier distribution or contribute to total current density. Denote LH1 in previous module as $2'$, now the matrix becomes

$$\begin{pmatrix} \frac{\rho_{22}}{\tau_{2'1}} + \frac{\rho_{22}}{\tau_{21}} + \frac{\rho_{33}}{\tau_{31}} + \frac{\rho_{44}}{\tau_{41}} & -\frac{\rho_{1'4}}{\tau_{d14}} & -\frac{\rho_{1'3}}{\tau_{d13}} & -\frac{\rho_{1'2}}{\tau_{d12}} \\ -\frac{\rho_{41'}}{\tau_{d14}} & -\frac{\rho_{44}}{\tau_{43}} - \frac{\rho_{44}}{\tau_{42}} - \frac{\rho_{44}}{\tau_{41}} + \frac{\rho_{22}}{\tau_{2'4}} & -\frac{\rho_{43}}{\tau_{d43}} & -\frac{\rho_{42}}{\tau_{d42}} \\ -\frac{\rho_{31'}}{\tau_{d13}} & -\frac{\rho_{34}}{\tau_{d43}} & -\frac{\rho_{33}}{\tau_{31}} - \frac{\rho_{33}}{\tau_{32}} + \frac{\rho_{44}}{\tau_{43}} + \frac{\rho_{22}}{\tau_{2'3}} & -\frac{\rho_{32}}{\tau_{d32}} \\ -\frac{\rho_{21'}}{\tau_{d12}} & -\frac{\rho_{24}}{\tau_{d42}} & -\frac{\rho_{23}}{\tau_{d32}} & -\frac{\rho_{22}}{\tau_{21}} + \frac{\rho_{33}}{\tau_{32}} + \frac{\rho_{44}}{\tau_{42}} - \frac{\rho_{22}}{\tau_{2'}} \end{pmatrix} \tag{2.78}$$

Where $\frac{1}{\tau_{2'}} = \frac{1}{\tau_{2'4}} + \frac{1}{\tau_{2'3}} + \frac{1}{\tau_{2'2}} + \frac{1}{\tau_{2'1}}$. To obtain carrier distribution in steady state, just set left hand side of 2.77 to be zero and solve this equation system. Current density can be obtained after knowing population in each subband.

$$J = eN_{3D}(\frac{\rho_{44}}{\tau_{41}} + \frac{\rho_{33}}{\tau_{31}} + \frac{\rho_{22}}{\tau_{21}} + \frac{\rho_{22}}{\tau_{2'4}} + \frac{\rho_{22}}{\tau_{2'3}} + \frac{\rho_{22}}{\tau_{2'2}} + \frac{\rho_{22}}{\tau_{2'1}}) \tag{2.79}$$

where e is elementary charge, ρ_{ii} is normalized population, N_{3D} is 3D doping density. Simulate eigen-energy and wavefunction for two well valence band QCL design at different bias and apply density matrix formalism, we can obtain a curve of how current density and population inversion change with bias . Simulated peak current density is about $\sim$ 1200A/cm^2 which is higher comparing to conduction band two well structure. The reason is due to generally hole-phonon scattering rate is faster than electron-phonon scattering rate (this is especially true for heave hole due to heavier mass). Scattering between LH1 and LH1 is fast, this leads to extra current density even though this wont change hole distribution. Following [73] at design bias 32 kV/cm, population difference between upper and lower lasing level is about 10^{15}/cm^3 correspond to peak optical gain of about 14.7 /cm.

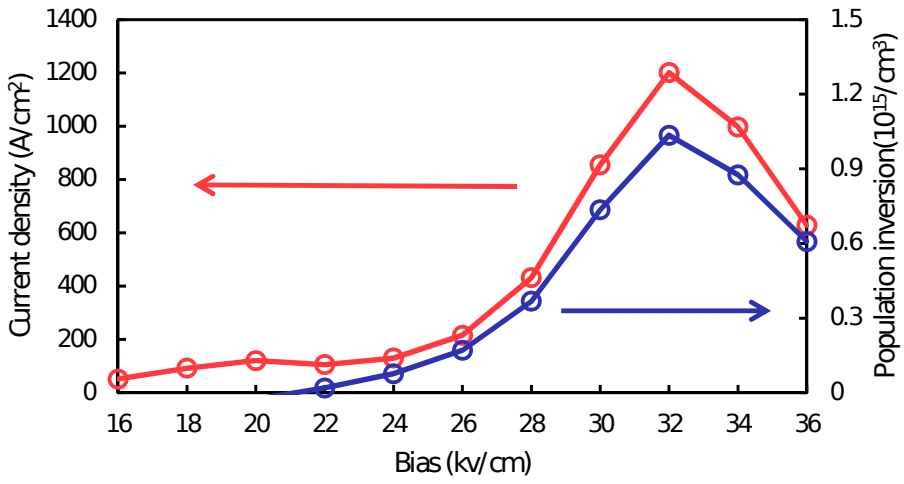

Figure 2.7: Current density and population inversion for design proposed in Figure 2.6 at different bias by assuming bulk doping density as $8 \times 10^{15}/\text{cm}^3$ and device size a 1 mm $\times$ 100 μm.

2.6.2 Valence-band ground-state QCL design

Electrical power consumed in device is proportional to square of current pass though the device. If current density at design bias is too high, heat dissipation can become a problem and thus degrade the performance of QCL. Intrawell phonon depopulation is ultra fast $\sim$ 100 fs thus two well design have very high current density. For this purpose a three well design using inter-well depopulation is introduced. [145] In order to keep lifetime of lower lasing level short $<$ 0.5ps a thin barrier have to used then lifetime of upper laser level can preserved only by spatially separate upper and lower lasing subbands. This trade-off is also implemented in similar design in conduction band [24].

At design bias scattering rate is obtained following the method described in section 2.3, $\tau_{HH3-HH1} \sim 1.52$ ps, $\tau_{HH2-HH1} \sim 0.21$ ps, $\tau_{HH3-HH2} \sim 3.5$ ps and $\tau_{LH1'-LH1} \sim 0.7$ ps. Even though an extra well is inserted, however in this design still there is only four subbands involved in hole transport thus2.77,2.79 is still valid when analysis hole distribution in this design. Again, current density and population inversion versus

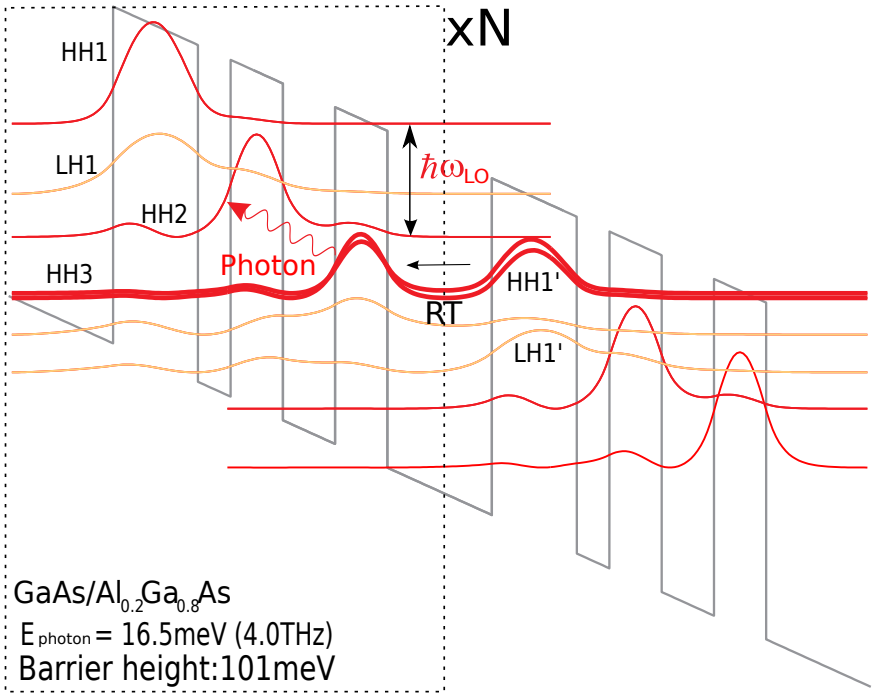

Figure 2.8: Valence band diagram of three well ground state (four level) QCL design utilizeGaAs/$Al_{0.2}Ga_{0.8}As$. Unlike two well structures, inter-well phonon depopulation is utilized instead of intra-well phonon scattering. The layer thickness start from injector in monolayer (ML) is 16/13/5/8/8/8. Design bias is 31.7 kV/cm and $E_{photon} = 17$ meV (4.1 THz)

bias are simulated. Due to all transitions are more diagonal peak current density is reduced to about $\sim$ 800A/cm^2 . At design bias 31.7 kV/cm, population difference between upper and lower lasing level is about 1.8×10^{15}/cm^3. The momentum matrix element for radiative transition is 2.114×10^{16}kg $\cdot J$, yield to peak optical gain as 16.2/cm.

2.6.3 Experimental Results: Demonstration of Sequential Resonant Tunneling

Length of one module is less than half of electron based design using similar strategy. A thicker active region gives lower waveguide loss [73] however voltage across device which equals to electric field times total length of active region will beyond pulse

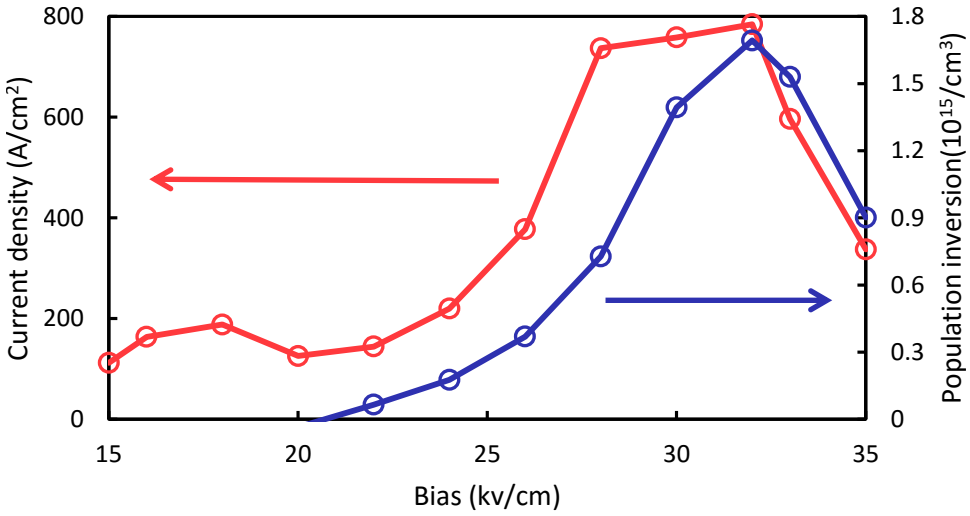

Figure 2.9: Current density and population inversion for design proposed in Figure 2.8 at different bias by assuming bulk doping density as $8 \times 10^{15}/\text{cm}^3$ and device size a 1 mm $\times$ 100 μm.

supply capability. Thus two well design is repeated 320 time and ground state design is repeated 305 times yield an active region about $\sim 5\mu$m thick. Two wafers were grown by MBE for each design (VB0721 and VB0722 for VB2W320 design and VB0723 and VB0724 for VBGS305 design)

Metal-metal waveguide ridge lasers were processed by wet-etching using the method outlined in ref [67, 66]. Ti/Cu are deposit on QCL active region and a GaAs receptor by electron beam evaporation. After thermo-compression wafer bonding, GaAs subtract for QCL active region is then removed by lapping and chemical etching ($NH_4OH : H_2O_2$ 1:19). Doped contact layer is defined by photo lithograph (microposit S1813) subsequent wet etching using $H_2SO_4 : H_2O_2 : H_2O$ equals 1 : 8 : 80. Grating structure is defined by using image reversal photo resist AZ5214. Ti/Cu/Au top metal grating is then fabricated by lifting-off. QCL lase ridge is finally defined by another lithograph followed by wet etching using ($H_2SO_4 : H_2O_2 : H_2O$ 1 : 8 : 80).

Pulsed IV of VB2W320 design are measured for both VB0721 and VB0722 wafer. Sample size is about $100\mu\text{m} \times 500\mu\text{m}$. Sample is mounted on a copper mount, a temperature sensor is also mounted on the same mount to monitor mount temperature in

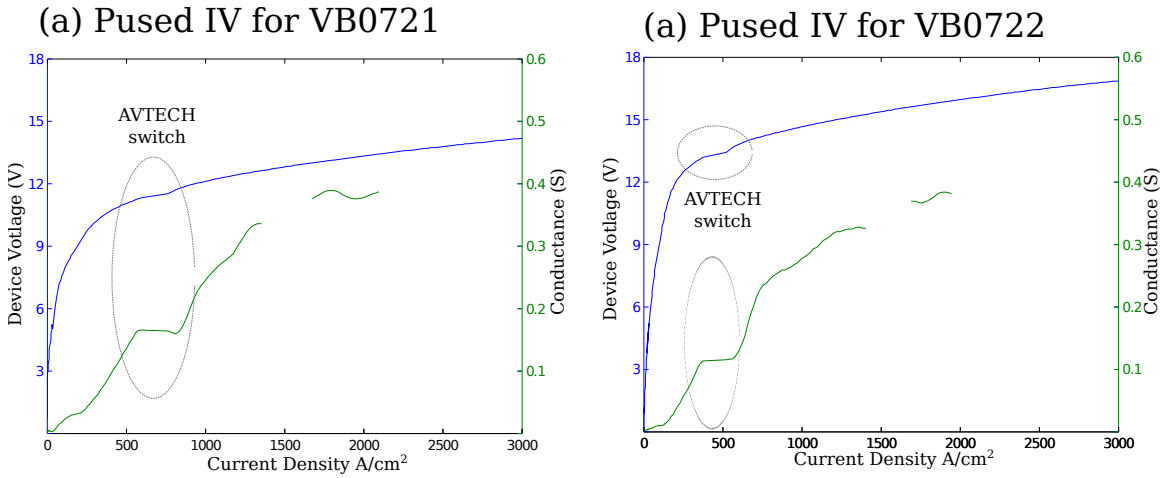

Figure 2.10: Pulsed IV and differential conductance for VB2W320 design measured at 47 K

real time. Pulsed width is 200 ns while repetition rate is 10 KHz in order to minimize heat generated within sample. Voltage step during measurement is 1 V Illustrated in figure 2.10, both sample showing similar IV characteristic. Measured current density is more than doubled than what is predicted by density model. Possible reason are listed below. First possibility is escape rate from light hole to continuum is very high, this leakage current is not included in density matrix model. Real doping density may higher than what is expected. Since current density is proportional to doping density, this could be second possibility. Another uncertainly in quantum transport is resonant tunneling between LH subband to HH subband. Experimental result and theoretical analysis suggest that with enough large in plane momentum, this tunneling could be very rapid. Since it is hard to determine in-plane momentum experimentally, contribution from this tunneling channeling to total current density cannot evaluated explicitly.

Although current density is higher than predicted value from out model, measured IV clearly showing change of differential conductance/resistance suggesting quantum transport of holes. Differential conductance is broken because this curve is plot after a moving average. Voltage step is too rough, leads to broken line after using "smooth"

function in MATLAB. Though differential conductance curve is broken, some useful information can still be obtained. Conductance curve is keep increasing without drop, suggest that we have not bias up to design bias until pulse supply reach its own limit. Sampled fabricated from two wafer for VBGS305 design are also tested in pulsed

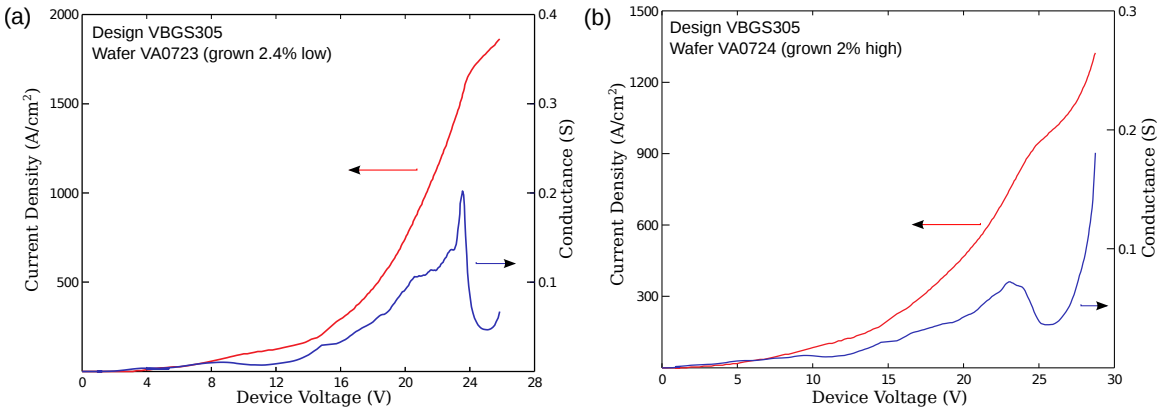

Figure 2.11: (a) Current-density and differential-conductance versus voltage of ridge-cavity devices with metal-metal waveguide fabrication for MBE grown wafers for design VBGS305. The plot in (a) is from wafer VA0723, which was undergrown from the designed specification by 2.4 %. The plot in (b) is from a second wafer VA0724, which was overgrown by 2.0 %. All data are obtained from cavities of dimensions 5 μm $\times$ 100 μm $\times$ 500 μm in pulsed mode of operation. No lasing was observed. However, a plateau is observed in the I-V characteristics of voltage of about 23.5 V, with a corresponding peak in the conductance plot, which is a signature of the sequential resonant-tunneling in the GaAs/AlGaAs superlattice for the desired HH1'-HH3 tunneling transition. The reduction in the current-density at desired alignment in (b) with respect to (a) is representative of reduction in efficiency of resonant-tunneling due to thicker injector barrier.

mode. The structure was tested in pulsed-mode with 200 ns pulser-width and 10 kHz repetition-rate. Ground state design showing much lower current density comparing to VB2W320 design, verifying that inter-well phonon depopulation do increase hole-phonon scattering time thus reduce current density. Figure2.11 illustrates current-voltage (I-V) and conductance-voltage (G-V) characteristics of a 100 μm $\times$ 500 μm ridge. While no lasing was observed, a plateau is observed in the I-V characteristics of voltage of about 23.5 V, with corresponding peaks in the conductance plot, which is a signature of the sequential resonant-tunneling in the GaAs/AlGaAs superlattice

for the desired HH1'-HH3 tunneling transition. The reduction in the current-density at desired alignment for the thicker-grown wafer is representative of reduction in efficiency of resonant-tunneling due to thicker injector barriers in that growth. The VA0723 wafer device shows a sharp conductance peak while it is not observed for VA0724 wafer. The reasons for this are not entirely well understood. However, such sharp conductance peaks bode well for a specular resonant-tunneling transport in the superlattice structure, which is likely to establish the desired population inversion between HH3 and HH2 subbands. With proper design of low-loss optical cavities, lasing could potentially be realized in such a quantum-cascade structure.

2.7 Conclusions and Summary

In conclusion, we have reported on design and experimental results from a hole-based terahertz quantum-cascade laser structure. we have derived an expression for calculating hole-LO phonon scattering rate taking account for nonparabolicity and anisotropy of valence subband. Density matrix approach is reviewed and used to predict hole distribution. The effect of valence band mixing is clarified and anticrossing gap for HH to HH tunneling decrease with increasing in-plane momentum while anticrossing gap for LH to HH tunneling change in opposite way. Two hole based THz QCLs with only four subbands involved in transport is designed and analyzed. VB2W320 design is based on intersubband transitions between heavy-holes in two-well GaAs/AlGaAs superlattices with resonant-tunneling injection and intrawell hole-phonon scattering-assisted depopulation. VBGS305 design is based on intersubband transitions between heavy-holes in three-well GaAs/AlGaAs superlattices with resonant-tunneling injection and interwell hole-phonon scattering-assisted depopulation. Experimental results show signatures of sequential resonant-tunneling transport in such a superlattice for the first time, which indicates effective hole quantum-transport and is promising to-

ward development of the first hole-based intersubband laser.

Chapter 3

Electrical Tuning of THz QCLs at High Temperatures

Many molecules have strong and distinct spectral "fingerprint" signatures at THz frequencies owing to their low-energy vibrational and rotational modes that couple strongly to electromagnetic radiation [100]. This makes THz frequencies important for both scientific and commercial applications in sensing by imaging or spectroscopic analysis. One important application of THz QCLs is investigation of well defined molecular lines in radio astronomy [120] by high-resolution heterodyne spectroscopy [46]. Fabrication of THz QCL device emitting at exact desired frequency is impractical; limited by lithographic accuracy and variation of both material composition and layer thickness during semiconductor superlattice epitaxy. This concern as well as many spectroscopy techniques require sweeping the frequency of the laser across the molecular absorption line, making frequency tunability highly desirable for THz QCLs.

3.1 Tunability of THz QCLs and Existing Techniques

To tun a THz quantum cascade laser either refractive index of ambient where electric field extended to is modified or waveguide (lasing cavity) geometry is changed. Different mechanisms for tuning THz QCLs have been proposed and experimentally implemented. Tuning by temperature variation [79], external-cavity [82], MEMS [108], material-condensation [124], coupled-cavity [80], three-terminal schemes [104], and cavity-pulling [125] have already demonstrated while each method is affiliated with some drawbacks. MEMS tuning and external-cavity tuning require mechanically movable components. These methods can achieve very large tuning range at the cost of slow tuning speed and a relatively bulky and complex system. Temperature change can tune up to $\sim$ 20 GHz but optical output power drops significantly during the process and the tuning speed is inherently slow. 25 GHz mode-hop free tuning range is achieved by gas condensation approach. Such technique modifies the refractive index of medium surrounding QCL laser ridge which subsequently alters resonant frequency. However additional gas flow control requires a more complicated system moreover the nature of this method rules out fast tuning possibility. Mechanisms which modifies resonant frequency by purely changing injection current are always preferred due to their compactness, speed and simplicity [79, 36, 144] .

3.2 Cavity-pulling induced by detuned intersubband absorption

The active gain medium in a laser's cavity contributes to both real (χ') and imaginary (χ'') components of the electrical susceptibility $\chi = \chi' + i\chi''$ of the medium. Intersubband gain or intersubband loss which are proportional to imaginary part of complex

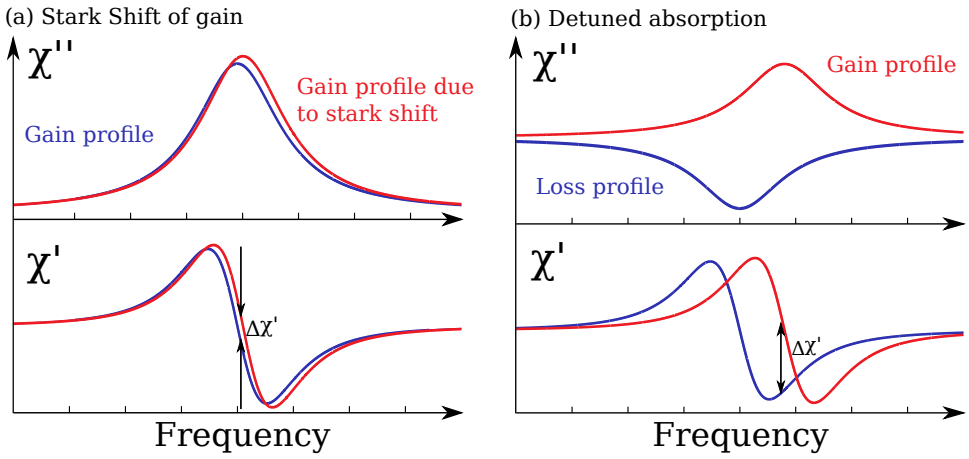

Figure 3.1: Schematic explanation of the different origin of susceptibility change induced by stark shift and detuned absorption. (a) By increasing the bias on QCL, frequency corresponding for peak gain is blue-shift. The blue-shift induce a modification on the real part of intersubband susceptibility thus tuning cavity mode. (b) Similar to that of Stark shift, detuned intersubband absorption can also lead to modification of electric-susceptibility. The change of χ' can be engineered by choosing frequency separation between emission peak and absorption peak.

susceptibility χ'' is a function of bias applied upon gain medium. Real part χ' and imaginary part χ'' of electrical susceptibility are associated with each other through Kramers-Kronig relation [142]. Owing to that fact, refractive index ($= n\sqrt{1+\chi'}$) of the medium turns out to have bias dependence, as a result the laser's emission frequency is tuned and this effect is terms as "cavity-pulling" [142]. For QCLs, contribution of gain medium to χ' is negligible at the lasing frequency due to symmetric atomic-like Lorentzian lineshape of gain spectrum $\chi''(\omega)$ for the intersubband transitions, where $\chi' \approx 0$. However when radiative subbands also interact coherently with other subbands via resonant-tunneling as well as non-radiative transitions, exact spectrum of $\chi''(\omega)$ is no longer Lorentzian[77]. Cavity-pulling effect based tuning comes be a very attractive method since it relies purely on an electrical drive mechanism with no moving parts and essentially instantaneous

Cavity-pulling effect is much stronger in THz QCLs than that in mid-infrared QCLs because of the use of metallic-cavities with almost unity optical confinement-

factor and larger values of refractive-index change accompanying the intersubband gain. These facts indicate that sole THz QCL active region could cause sufficient refractive index change enable cavity-pulling effect based tuning promising. In order to achieve large tuning range by cavity-pulling effect, QCL's injection current is varied by at least 50 % [125, 36, 144, 56]. Such variation of injection current requires a large dynamic range; thus, to our best knowledge, all tunable THz QCLs based on cavity-pulling effect operate at very low temperature ($\leq$ 10 K). Similar to the change in susceptibility induced by the Stark-shift of the laser's intersubband emission, a *detuned* intersubband absorption between subbands can also result in modification of electric susceptibility. In this case, the amount of tuning is controlled by the strength of intersubband absorption. Opposite to intersubband gain, which require active region to be biased above lasing threshold, utilizing intersubband absorption induced electrical susceptibility change urge THz QCL active region to be biased below threshold. This naturally result in eliminating the demand for large dynamic range. Thus the tuning device could work at significantly higher temperature. Maximum operating temperature of QCLs would be the theoretical limit for the operation of such tunable device.

Detuned absorption can be achieved with identical active region for lasing. When change the bias of active region, subband alignment as well as carrier distribution will change accordingly. By carefully checking band diagram at different bias, we can choose bias when absorption close to lasing frequency happened. This detuned absorption can modify susceptibility hence shift resonant frequency. To enable lasing and absorption happened at same time, a optical coupled while electrical isolate cavity need to demonstrated. Showing in latter sections, such kind of cavity could be two very closely mounted THz QCL ridges with metal-metal waveguide or two laterally adjacent specially designed distributed feedback THz QCL facilitating optical coupling. Procedure to numerical predict intersubband susceptibility is following: firstly

eigen-energy and wavefunction for each subband are found by solving Schrodinger equation, secondly electron-LO phonon scattering as well as interface roughness scattering are calculated based on information obtained in step one, thirdly density matrix formalism describe in section 2.4 are used to simulation carrier distribution among different subbands. Finally intersubband susceptibility is calculated from subbands separation, carrier distribution as well as dipole matrix element between two subbands by assuming Lorentzian line-shape.

3.3 Electrical tuning of a Fabry-Pérot cavity 2.1 THz QCL at 78 K

A comprehensive check was performed of a variety of existing THz QCL designs in our lab by evaluation of their bandstructures at different bias. Afterwards, a scattering-assistant injection design for 2.1 THz named as SARP172 was chosen for demonstration of detuned intersubband absorption induced tuning concept. Details of this QCL design are described elsewhere [67]. There are mainly three reason why SARP172 design is preferred. Firstly and most important reason is theoretical analysis indicating that SARP172 design allow absorption about 1 THz away from peak emission frequency. Analysis procedure will describe explicitly later. Second reason is SARP172 design aim for lasing at low frequency ~ 2 THz, the lower lasing frequency the easier lasing mode leak laterally for a specific QCL ridge width. Third reason is this design have relatively high current density at bias which absorption suppose to happen. The fact suggest that there are enough electrons distribute among excited subband thus potentially contribute to absorption.

3.3.1 Detuned absorption in a scattering-assited THz QCL design

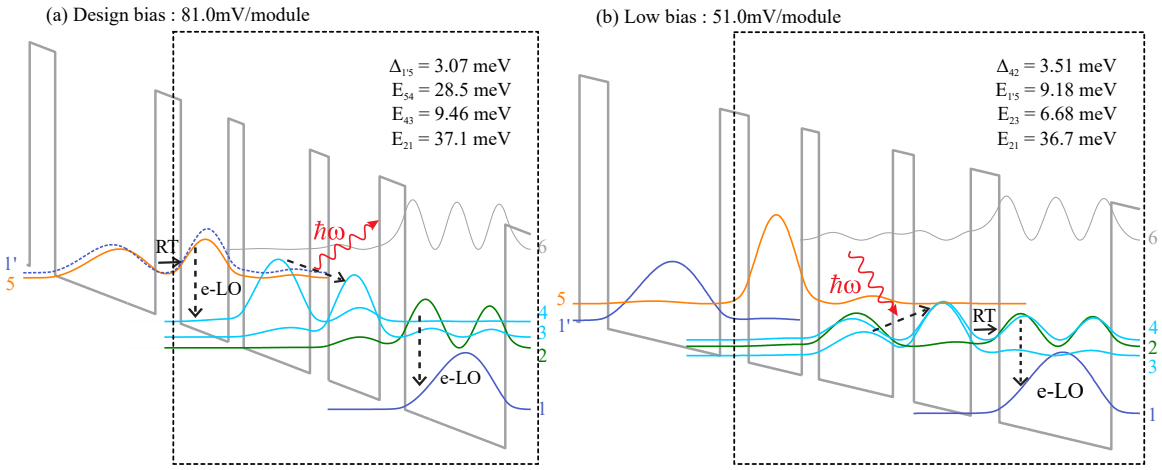

Figure 3.2: (a) Conduction-band diagram at bias corresponding to peak gain for a THz QCL structure named SARP172 that achieves gain from $2 - 2.5$ THz [67]. Starting from the injector barrier on the left, layer thickness for the GaAs/$Al_{0.15}Ga_{0.85}As$ superlattice in nm are 4.2/7.9/2.5/11.0/3.1/8.5/4.2/16.7. The average doping in the active region is 5.4×10^{15} cm^{-3}. (b) Conduction-band diagram at lower bias for the same QCL structure. At such bias, upper radiative subband 4 is aligned to phonon subband 2 in depopulation well. Fast LO-phonon scattering depopulates the doublet resulting in intersubband absorption from $3 \rightarrow (2, 4)$, at a frequency that is detuned from QCL's emission frequency.

The scattering assistant (SA) injection scheme requires a large operating electric-field across the QCL superlattice in contrast with the RT scheme for design of THz QCLs. It it difficult to implement the SA scheme with $Al_{0.15}Ga_{0.85}As$ barriers (barrier-height$\sim$ 135meV) when the QCL is designed for emission at higher frequencies. Consequently, initial demonstration for THz QCLs with SA scheme utilized superlattices with taller barriers. However, designs with high barriers have to choose thinner barriers to maintain optimum carrier transport, the increase in barrier height result in enhanced interface-roughness scattering that may worsen the QCLs performance [68]. Hence, for this implementation, $Al_{0.15}Ga_{0.85}As$ barriers is chosen.

Figure 3.2 shows the conduction-band diagram of the design named SARP172 (wafer VA0344) at two relevant bias conditions in which intersubband gain and loss are realized respectively. The structure was grown in the GaAs/ $Al_{0.15}Ga_{0.85}As$ material system with 172 cascaded periods yielding an overall active region thickness of ~ 10 μm. Structure SARP172 is a modification of the first reported THz QCL with SA scheme in [76]. It utilizes similar design scheme of four-wells per period, in which predominantly five subbands take part in carrier transport. The carriers are injected from an

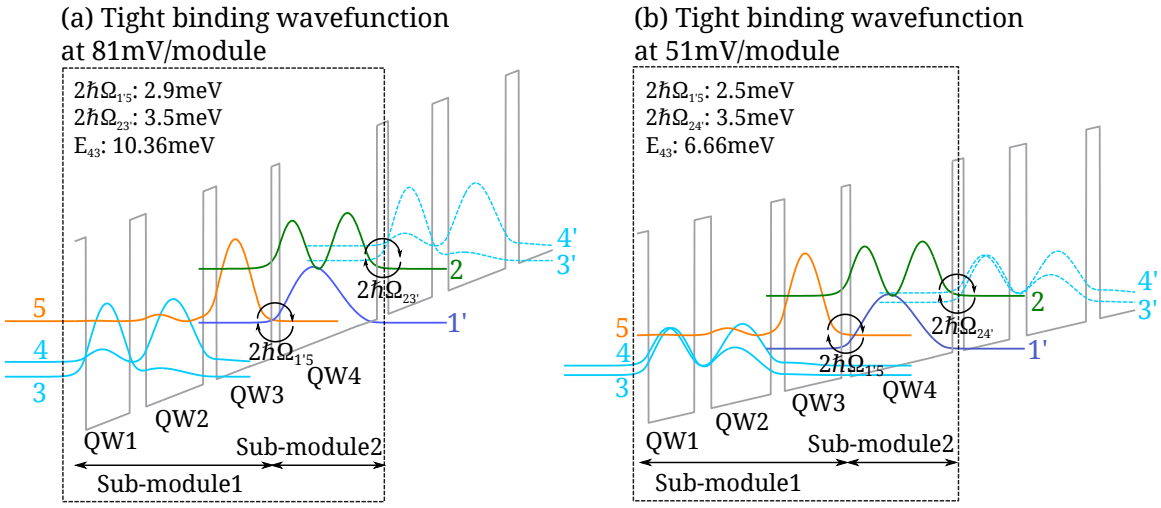

Figure 3.3: (a) Tight binding wavefunction of five level scattering assistant terahertz QCL SARP172 at its design bias. One QCL module is split into two sub-modules across injector barrier and collector barrier. First sub-module starts from collector barrier (CB) consisting quantum well 1, 2 and 3 and ends with injector barrier (IB). The other sub-module includes injector barrier, quantum well 4 and collector barrier. (b) Tight binding wavefunction of SARP172 at low bias. One QCL module is splitted into two sub-modules across injector barrier and collector barrier in the same way as in figure 3.3(a).

anticrossed doublet of $1', 5($ anticrossing at resonance $E_{1'5} = 3.1$ meV) into the upper radiative subband 4 by electron-LO-phonon scattering ($E_{54} =\sim 28.5$ meV). The radiative transition is from subband 4 to 3 ($E_{43} =\sim 9.5$ meV at the designed bias), and the lower radiative subband 3 is depopulated by the resonant-phonon scattering. Figure 3.2(b) illustrates the conduction-band diagram for low-bias at which the upper laser subband is in alignment with excited subband in the wide phonon-depopulation well. Wavefunction overlap between subband 3 and subband 1 is smaller than wavefunction overlap between subband 4, 2 and subband 1, moreover E_{31} is detuned from LO phonon energy while E_{41} and E_{21} are in resonance with LO phonon energy. Both factors indicate LO phonon scattering rate between subband 4, 2 to subband 1 are faster than that between subband 3 to subband 1. At this resonance, there is intersubband absorption in the active region due to $3 \rightarrow (2, 4)$ at a frequency of ~ 1.7 THz, since electrons primarily get localized in subband 3.

Density matrix model in ref [77] is expanded to describe quantum transport behavior of SARP172 design in which five subbands are involved. In a first order approximation, we assume RT to be independent of the electron momentum in the plane of the quantum wells (QWs). The subband lifetimes are assumed to be thermal averaged over the electron distribution within a subband and are to be calculated from Fermi's golden rule. Formula to calculate electron-LO phonon scattering, interface roughness scattering can be found in [133] and [126] respectively. At design bias, electrons are

transport from level 1' to level 5 by RT and scattered into both upper and lower lasing levels, electrons locate in level 3 resonant tunnel to level 2 and depopulate back to ground state 1' by fast LO phonon scattering. The time-evolution of DM for SARP172 at design bias is then written as:

$$\frac{\mathrm{d}}{\mathrm{d}t}\begin{pmatrix} \rho_{1'1'} & \rho_{1'5} & \rho_{1'4} & \rho_{1'3} & \rho_{1'2} \\ \rho_{51'} & \rho_{55} & \rho_{54} & \rho_{53} & \rho_{52} \\ \rho_{41'} & \rho_{45} & \rho_{44} & \rho_{43} & \rho_{42} \\ \rho_{31'} & \rho_{35} & \rho_{34} & \rho_{33} & \rho_{32} \\ \rho_{21'} & \rho_{25} & \rho_{24} & \rho_{23} & \rho_{22} \end{pmatrix} = -\frac{i}{\hbar}\left[\begin{pmatrix} E_{1'} & -\hbar\Omega_{1'5} & 0 & 0 & 0 \\ -\hbar\Omega_{1'5} & E_5 & 0 & 0 & 0 \\ 0 & 0 & E_4 & 0 & -\hbar\Omega_{42} \\ 0 & 0 & 0 & E_3 & -\hbar\Omega_{32} \\ 0 & 0 & -\hbar\Omega_{42} & -\hbar\Omega_{32} & E_2 \end{pmatrix}, \bar{\bar{\rho}}_{(1',5,4,3,2)}\right]$$

$$+\begin{pmatrix} \frac{\rho_{22}}{\tau_{21}}+\frac{\rho_{44}}{\tau_{41}} & -\frac{\rho_{1'5}}{\tau_{d15}} & -\frac{\rho_{1'4}}{\tau_{d14}} & -\frac{\rho_{1'3}}{\tau_{d13}} & -\frac{\rho_{1'2}}{\tau_{d12}} \\ -\frac{\rho_{51'}}{\tau_{d15}} & -\frac{\rho_{55}}{\tau_{54}}-\frac{\rho_{55}}{\tau_{53}} & -\frac{\rho_{54}}{\tau_{d54}} & -\frac{\rho_{53}}{\tau_{d53}} & -\frac{\rho_{52}}{\tau_{d52}} \\ -\frac{\rho_{41'}}{\tau_{d14}} & -\frac{\rho_{45}}{\tau_{d54}} & \frac{\rho_{55}}{\tau_{54}}-\frac{\rho_{44}}{\tau_{43}}-\frac{\rho_{44}}{\tau_{41}} & -\frac{\rho_{43}}{\tau_{d43}} & -\frac{\rho_{42}}{\tau_{d42}} \\ -\frac{\rho_{31'}}{\tau_{d13}} & -\frac{\rho_{35}}{\tau_{d53}} & -\frac{\rho_{34}}{\tau_{d43}} & \frac{\rho_{55}}{\tau_{53}}+\frac{\rho_{44}}{\tau_{43}} & -\frac{\rho_{32}}{\tau_{d32}} \\ -\frac{\rho_{21'}}{\tau_{d12}} & -\frac{\rho_{25}}{\tau_{d52}} & -\frac{\rho_{24'}}{\tau_{d42}} & -\frac{\rho_{23}}{\tau_{d32}} & -\frac{\rho_{22}}{\tau_{21}} \end{pmatrix} \tag{3.1}$$

Tight binding wavefunction for SARP172 design at 51 meV/module is shown in figure 3.3 (b). Electrons are transport from subband 1' to subband 5 by tunneling between detuned subbands and scattered into both subbands 4 and 3, electrons locate in subband 4 resonant tunnel to subband 2 and scattered back to ground state 1' efficiently through LO phonon scattering. Time-evolution of DM for tight-binding

biases at such bias then expressed as:

$$\frac{\mathrm{d}}{\mathrm{d}t}\begin{pmatrix} \rho_{1'1'} & \rho_{1'5} & \rho_{1'4} & \rho_{1'3} & \rho_{1'2} \\ \rho_{51'} & \rho_{55} & \rho_{54} & \rho_{53} & \rho_{52} \\ \rho_{41'} & \rho_{45} & \rho_{44} & \rho_{43} & \rho_{42} \\ \rho_{31'} & \rho_{35} & \rho_{34} & \rho_{33} & \rho_{32} \\ \rho_{21'} & \rho_{25} & \rho_{24} & \rho_{23} & \rho_{22} \end{pmatrix} = -\frac{i}{\hbar}\left[\begin{pmatrix} E_{1'} & -\hbar\Omega_{1'5} & 0 & 0 & 0 \\ -\hbar\Omega_{1'5} & E_5 & 0 & 0 & 0 \\ 0 & 0 & E_4 & 0 & -\hbar\Omega_{42} \\ 0 & 0 & 0 & E_3 & -\hbar\Omega_{32} \\ 0 & 0 & -\hbar\Omega_{42} & -\hbar\Omega_{32} & E_2 \end{pmatrix}, \bar{\bar{\rho}}_{(1',5,4,3,2)}\right]$$

$$+\begin{pmatrix} \frac{\rho_{22}}{\tau_{21}}+\frac{\rho_{33}}{\tau_{31}} & -\frac{\rho_{1'5}}{\tau_{d15}} & -\frac{\rho_{1'4}}{\tau_{d14}} & -\frac{\rho_{1'3}}{\tau_{d13}} & -\frac{\rho_{1'2}}{\tau_{d12}} \\ -\frac{\rho_{51'}}{\tau_{d15}} & -\frac{\rho_{55}}{\tau_{54}}-\frac{\rho_{55}}{\tau_{53}} & -\frac{\rho_{54}}{\tau_{d54}} & -\frac{\rho_{53}}{\tau_{d53}} & -\frac{\rho_{52}}{\tau_{d52}} \\ -\frac{\rho_{41'}}{\tau_{d14}} & -\frac{\rho_{45}}{\tau_{d54}} & \frac{\rho_{55}}{\tau_{54}}-\frac{\rho_{44}}{\tau_{43}} & -\frac{\rho_{43}}{\tau_{d43}} & -\frac{\rho_{42}}{\tau_{d42}} \\ -\frac{\rho_{31'}}{\tau_{d13}} & -\frac{\rho_{35}}{\tau_{d53}} & -\frac{\rho_{34}}{\tau_{d43}} & \frac{\rho_{55}}{\tau_{53}}+\frac{\rho_{44}}{\tau_{43}}-\frac{\rho_{33}}{\tau_{31}} & -\frac{\rho_{32}}{\tau_{d32}} \\ -\frac{\rho_{21'}}{\tau_{d12}} & -\frac{\rho_{25}}{\tau_{d52}} & -\frac{\rho_{24'}}{\tau_{d42}} & -\frac{\rho_{23}}{\tau_{d32}} & -\frac{\rho_{22}}{\tau_{21}} \end{pmatrix} \tag{3.2}$$

In order to obtain carrier distribution between different subbands steady state solution of equation 3.1 and equation 3.2 are calculated by set left hand side of the equations equals to 0. Diagonal terms of matrix $\bar{\bar{\rho}}$ represent populations in each subband. Optical gain/loss profile is phenomenologically approximated to be Lorentzian shape, gain/loss coefficient due to intersubband transition between subband i and subband f, where $E_i > E_f$ are considered as [73]:

$$g_{mat}(\omega) = \frac{\pi e^2 \omega}{\epsilon_0 n_r c}|\mathrm{z_{if}}|^2 \Delta \mathrm{N_{3D}} \frac{\frac{\Delta \mathrm{E}}{2\pi}}{(\mathrm{E_f}-\mathrm{E_i}+\hbar\omega)^2+\left(\frac{\Delta \mathrm{E}}{2}\right)^2} \tag{3.3}$$

Where z_{if} is dipole matrix element between initial and final subbands determined by their wavefunction overlap and ΔN_{3D} is population difference between final and initial subbands obtained from steady-state solution of DM equation. The optical

gain/loss coefficient g_{mat} is related to $\chi''(\omega)$ by:

$$g_{mat}(\omega)|_{\chi'\chi''\ll n_r^2} = \frac{\chi''(\omega)}{n_r}\frac{\omega}{c} \tag{3.4}$$

combining equation equation 3.3 and equation 3.4 $\chi''(\omega)$ can be expressed as:

$$\chi''(\omega) = \frac{\pi e^2 |z_{if}|^2 \Delta N_{3D}}{\epsilon_0} \frac{\frac{\Delta E}{2\pi}}{(E_f - E_i + \hbar\omega)^2 + \left(\frac{\Delta E}{2}\right)^2} \tag{3.5}$$

Real part and imaginary part of electrical susceptibility is related with each other by Kramers-Kronig relation. *P.V.* is the Cauchy principal value [142].

$$\chi'(\omega) = \frac{1}{\pi} P.V. \int_{-\infty}^{\infty} \frac{\chi''(\omega')}{\omega' - \omega} d\omega' = \frac{1}{\pi}\left(\int_{\omega^+}^{\infty} \frac{\chi''(\omega')}{\omega' - \omega} d\omega' + \int_{-\infty}^{\omega^-} \frac{\chi''(\omega')}{\omega' - \omega} d\omega'\right) \tag{3.6}$$

Density matrix corresponding to figure 3.1 (a) and (b) are run and intersubband electrical susceptibility induced by $4 \rightarrow 3$ transition in (a) and $3 \rightarrow 4, 2$ transition in (b) are calculated.

Figure 3.4(c) reveals intersubband gain profile correspond to Fig 3.1(a) and intersubband loss profile associated with Fig 3.1(b) by assuming Lorentzian shape linewidth with FWHM of 2 meV. The absorption frequency is detuned ~ 0.8 THz away from lasing frequency, thus the χ' induced by detuned absorption is negative when χ' induced by lasing transition in lasing cavity is zero. As suggested in lower subplot in Figure 3.4(c), the absorption can lead to large change in real-part of susceptibility (refractive-index) at the QCL's emission frequency in lasing cavity.

3.3.2 Experimental setup and measurement results

As shown schematically in figure 3.5, we investigate tunable THz laser consists of two optical coupled while electrical isolated ridges with identical active region design.

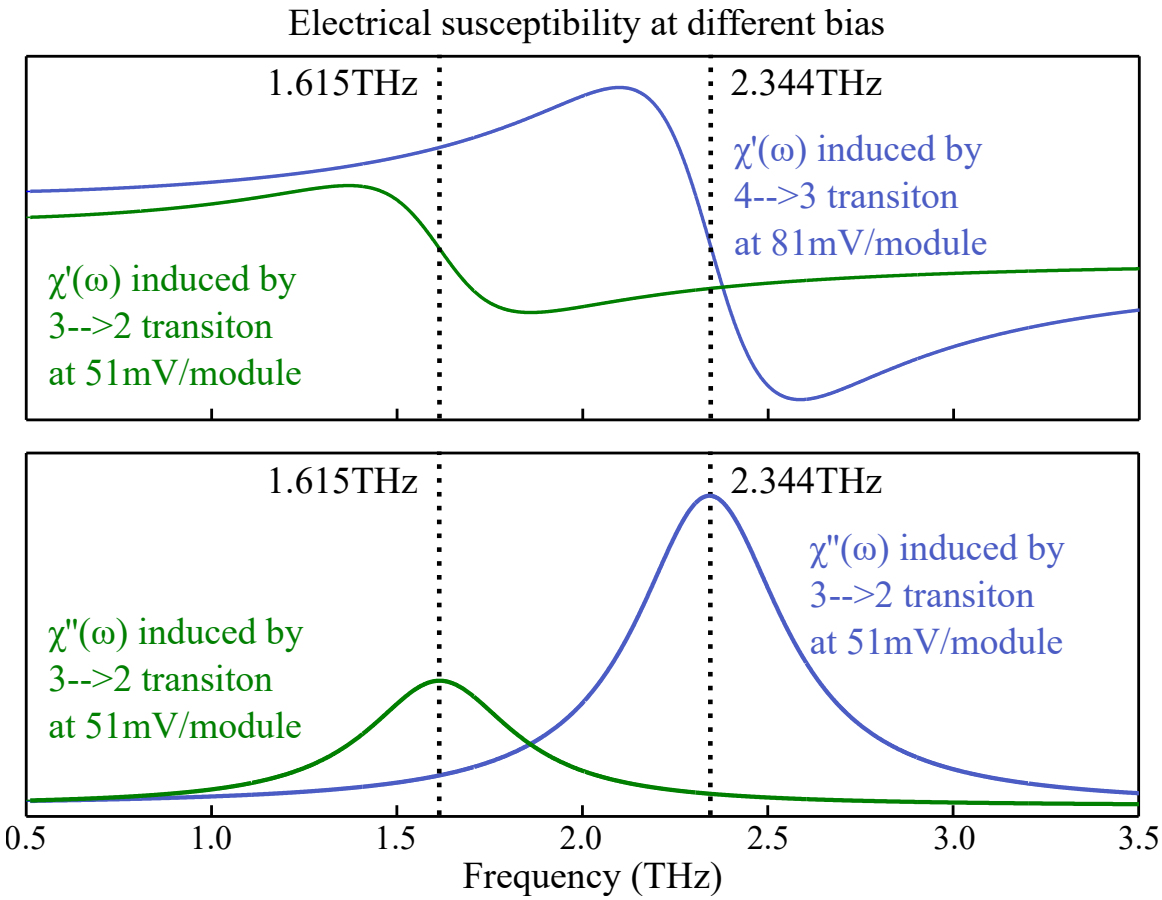

Figure 3.4: Calculated complex electrical susceptibility corresponding to bias conditions illustrated in Figure 3.1 (a) and (b). A Lorentzian shape linewidth is assumed for intersubband transition with full-width-half-maximum (FWHM) of 2 meV.

Metal-metal waveguide ridge lasers were processed by wet-etching using the method outlined in ref [67] with a Ti/Au layer sequence for the top metal and Ti/Cu for the bottom metal of the finally processed ridge waveguides. Such kind of THz QCL lase up to 141 K [66]. The fabricated devices were cleaved twice. First cleaving forms front and back facets (with back facets left uncoated). Following cleaving is along the middle of wet etching defined ridge, after cleaving one ridge along with bottom GaAs substrate separate into two parts. Silicon dioxide is deposit on cleaved lateral section by PECVD. After that cleaved QCL ridges are indium-soldered laterally adjacent to each other on a copper chip, wire bonded, and mounted on the cold plate of a dewar for measurements. The QCL laser ridge which is biased above its threshold is

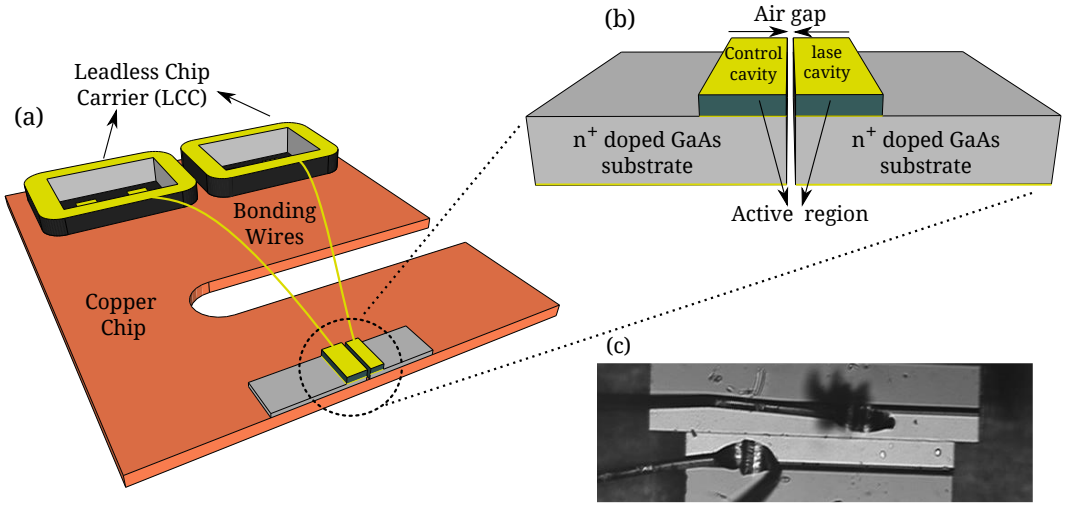

Figure 3.5: (a) Schematic of mounted tunable THz QCL device, two QCL ridges with identical active region are mounted laterally adjacent to each other on copper chip. Each QCL laser ridge is wire bond to different leadless chip carrier (LCC) thus they can be biased independently.
(b) Zoom in at mounted THz QCL ridges. Two Fabry-Pérot cavities laser ridges are fabricated with metal-metal waveguide. The one bias above threshold is referred as lasing cavity while the other one which bias below threshold correspond to control cavity with narrow air gap in between.
(c) Optical image of mounted device, device dimensions of QCL ridge 1 is 775 μm $\times$ 60 μm , while QCL ridge 2 dimensions are 685 μm $\times$ 60 μm. The width of air gap between two ridges is about few microns. Two gold bonding wires and pads for bias purpose are also visible in the image.

referred as "lasing cavity" while the other ridge which is biased below threshold is labeled as "control cavity" since it contributes to intersubband absorption inducing electrical susceptibility change. It should to be pointed out that considering the fact that two ridges are fabricated from identical active region, actual role of each laser ridge essentially relies on its bias condition. The function of each laser ridge can be simply exchanged by swapping their bias condition.

Optical power was detected from a single facet when collected with a Winston cone (with a circular opening of 1.7 mm diameter) and the pyroelectric detector (Gentec) was placed face to the dewar window. The device was operated in pulsed mode with 200 ns pulses repeated at 100 kHz. A 1 kHz gate signal from arbitrary function generator (Agilent 33500B) act as external trigger for both pulser and lock-in

amplifier (SR810) connected to pyroelectric detector. Device spectra were measured at a resolution of 1.8 GHz in linear scan mode with a Bruker Vertex 70 V infrared spectrometer that was pumped to about 3 hPa limiting any atmospheric water absorption. Absolute power measurements were carried out separately with a calibrated thermopile power meter (ScienTech, model AC2500) placed face to the dewar window, at a duty cycle of 3 % (300 ns pulses repeated at 100 kHz). The power detected by the power meter is reported without any corrections.

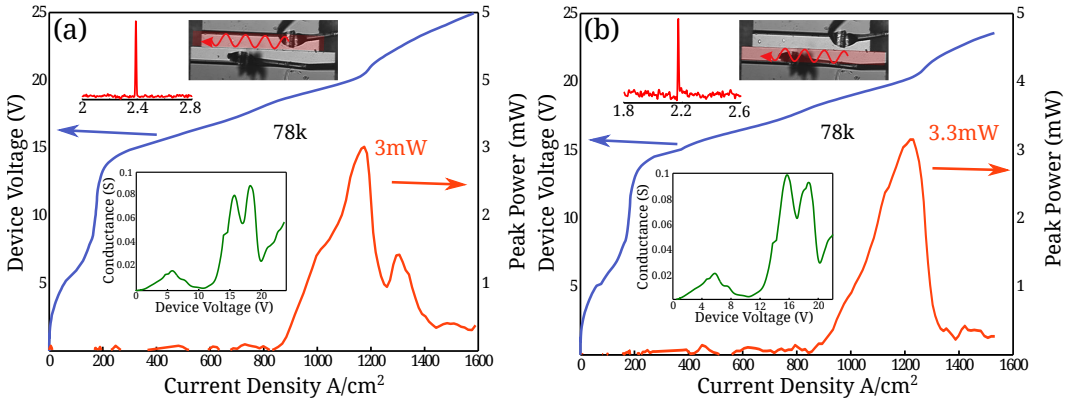

Figure 3.6: (a) Illustrated device characteristics of QCL ridge 1 as shown in inset of Figure 3.6(a) when it is solely biased. At liquid nitrogen temperature threshold current density is 840 A/cm^2 and peak current density is 1180 A/cm^2. The peak optical power emitted from QCL ridge 1 is 3 mW. Inserted spectrum correspond to a device bias of 18.6 V. At such bias condition QCL ridge 1 is lasing at single mode of 2.390 THz. (b) Illustrated device characteristics of QCL ridge 2 as shown in insert of Figure 3.6(b) when it is solely biased. At liquid nitrogen temperature threshold current density is 850 A/cm^2 and peak current density is 1230 A/cm^2. The peak optical power emitted from QCL ridge 1 is 3.3 mW. Lasing at 2.173 THz is observed at device bias of 18.5 V

The measurements are performed in pulse mode in order to prevent large change of device temperature and the failure of bonding wire, at a heat sink temperature of 77 K. Single mode operation is enabled by choosing device bias. The light emitted from QCL ridge is collected via a Winston cone and detected by a pyroelectric detector then peak output power is calibrated through an absolute power meter. The spectra are characterized by a commercial Fourier-transform-infrared spectrometer (FTIR) equipped with a DTGS pyroelectric detector and a Silicon beamsplitter. The mea-

sured spectrum resolution is limited by 0.0618 cm^{-1} (1.856GHz). Two Fabry-Pérot cavities are mounted laterally adjacent to each other with a narrow gap (< 5 μm) to form optically coupled-cavities, facilitated by the large lateral mode extent at THz frequencies. The two ridges are electrically isolated and can be biased independently. As shown in Fig 3.6, the width of both two ridges are 60 μm, and the lengths are 685 mm and 775 mm respectively. The 685 μm long ridge is referred as "ridge 1" while the 775 μm long ridge is referred as the "ridge 2". Before measuring lasing peak shift due to cavity-pulling induced by detuned intersubband absorption, both QCL ridges are separately applied bias to characterize their performance respectively. LIV curves and spectra of individual laser ridges measured at 78 K are shown in fig 3.6. Inset spectra indicate that both QCL ridges can lase at single mode by specifying proper bias. QCL ridge 1 is lasing at 2.39 THz under a device voltage of 18.6 V and emitting 3 mW peak optical power when current density is 1180 A/cm^2. Resonant frequency of QCL ridge 2 is 2.173 THz when applying 18.5 V bias. THz power radiating out from facet is 3.3 mW at a current density of 1230 A/cm^2.

Figure 3.7 depicts schematic of spectrum measurement set-up. Tunable THz QCL device is mounted inside dewar filled with liquid nitrogen (LN) while the dewar itself is fixed to FTIR (customized Bruker Vertex) through vacuum adapter. Through out measurement both FTIR and dewar are continuously pumped. A temperature sensor (Lakeshore) is mounted neighboring to the device to monitor temperature in real time. During tuning experiment a pulse generator (AVTECH) generate a pulse chain of 100 kHz repetition rate and 200 ns pulse width supplies constant voltage upon lasing cavity. Simultaneously, a home made pulser generate another pulse chain whose repetition rate is also 100 kHz however its pulse width is doubled to 400 ns. By properly adjusting relative phase between these two pulse chains, each 200 ns wide pulse will embedded inside the 400 ns wide pulse. Bias conditions are visualized and monitored by oscilloscope (Agilent) throughout all measurements.

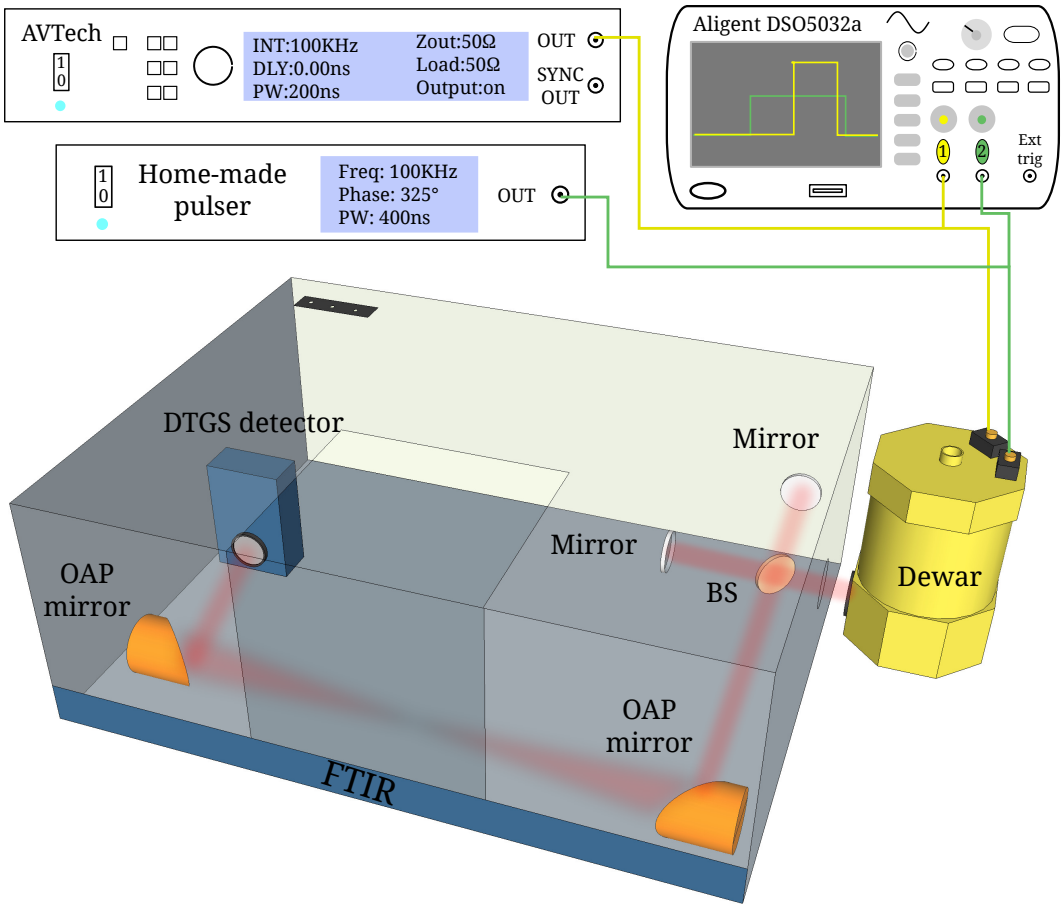

Figure 3.7: Schematic of spectrum measurement set-up. The tunable THz QCL device is mounted inside vacuum chamber on top of cold plate of LN dewar. A temperature sensor (Lakeshore) is mounted neighboring to the device to monitoring device temperature in real time. A commercial pulser (AVTECH) is used to bias lasing cavity at a pulse repetition rate of 100 kHz and pulse width of 200 ns. Meanwhile a home-made pulser generating a pulse chain at 100 kHz with 400 ns pulse width is used to apply voltage upon control cavity.

During tuning experiments initially 685 μm long ridge act as lasing cavity while the adjacent 775 μm laser ridge perform as control cavity. The bias of of the lasing cavity is kept at 18.6 V where it lases at single mode as shown in Figure 3.6(a) inset. The control-cavity is biased below lasing threshold throughout all experiments, thus it only contributes to intersubband absorption. If control cavity bias is around 14 V, conduction-band diagram will correspond to the case shown in Fig 3.2(b). Emission mode hop from 2.39 THz to 2.208 THz when electric field inside control

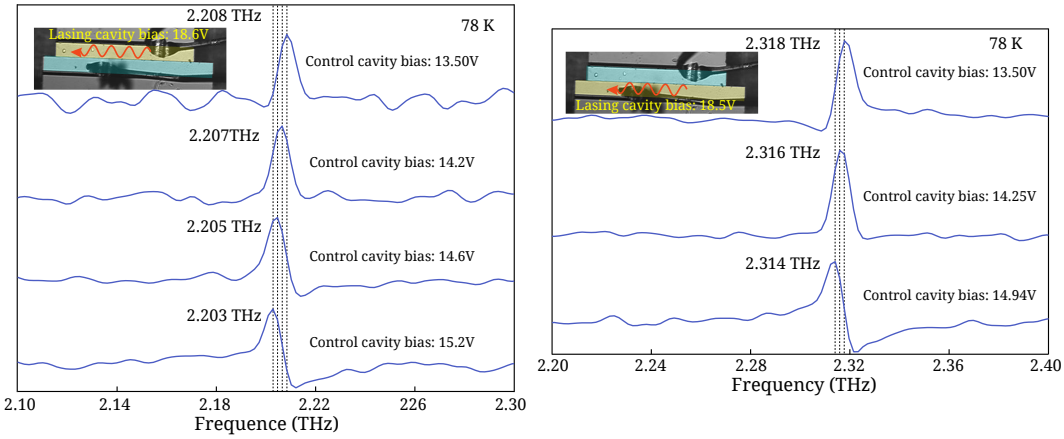

Figure 3.8: (a) Spectrum taken when QCL ridge 1 act as lasing cavity while QCL ridge 2 perform as control cavity. Resonant frequency shift from 2.208 THz to 2.203 THz during control cavity bias increase from 13.5 V to 15.2 V while lasing cavity bias maintained as 18.6 V. (b) Two QCL ridges switch their functions. Voltage across 775 μm long ridge is kept to 18.5 V corresponding to lasing cavity. Control cavity bias rise from 13.5 V to 14.94 V leads to 4 GHz continuous tuning.

cavity rise up to about 51mV/module, however single mode lasing behavior still maintained. This phenomenon distinctly demonstrates that two individual Fabry-Pérot metallic cavity optically coupled to each other forming a "super cavity". When the bias of control-cavity is increased from 13.5 V to 15.2 V, emission from the lasing-cavity is continuously tuned by 5 GHz as shown in figure 3.8(a). Secondly, the bias of two QCL ridges are swapped. 775 μm long ridge is biased to 18.6 V enabling emitting in single mode. When the bias of 685 μm long cavity is increased from 13.5 V to 14.94 V, emission from the lasing cavity is continuously tuned by 4 GHz as shown in figure 3.8(b) due to *detuned* intersubband absorption illustrated in figure 3.4. Temperature variation caused by device current increasing in control cavity is within 1 K, eliminating influence from temperature on refractive index.

There is a significant difference when comparing tuning induced by gain profile Stark shift to tuning caused by detuned absorption. In high performance devices with very large ratios between the upper and lower state lifetimes, the voltage essentially clamps to a constant value at threshold [125], limiting tuning range originating from

gain profile Stark shift. Thus current injected into active region is changing more than 50% in either single section or two section device to introduce sufficient Stark shift of the laser transition. On contrary, utilizing detuned intersubband absorption prohibits population inversion establish in the cavity. Alignment between different subbands involved in quantum transport of carriers are very sensitive to external bias so does carrier distribution among them. This explains the tuning phenomenon observed in this experiment only happened within a narrow bias range on control cavity.

3.4 Tuning Demonstration for single-mode THz QCLs (TUNDET202 Design)

Although using SARP172 active region, continuous electrical tuning of 5 GHz at liquid nitrogen temperature are first time demonstrated, there are two aspect further work can be done. Firstly at absorption type alignment, two subbands in injector are not in resonance with each other result in less efficient electron injection to desired subband. Secondly, Fabry-Pérot metal-metal waveguides do not select lasing mode thus single mode operation can only achieved by carefully choosing bias. More over far field beam pattern of metal-metal waveguide are highly diverge while applications like chemical sensing or spectroscopy request narrow emission pattern in far field. To improve this two aspects a new active region named as TUNDET202 with three well resonant tunneling injection resonant tunneling depopulation design enabling detuned intersubband absorption is introduced. A unique antenna-coupled distributed-feedback (DFB) metallic cavity that facilitates lateral optical coupling is utilized to achieve robust single mode operation as well as engineer far field radiation beam.

3.4.1 Detuned intersubband absorption in TUNDET202 design

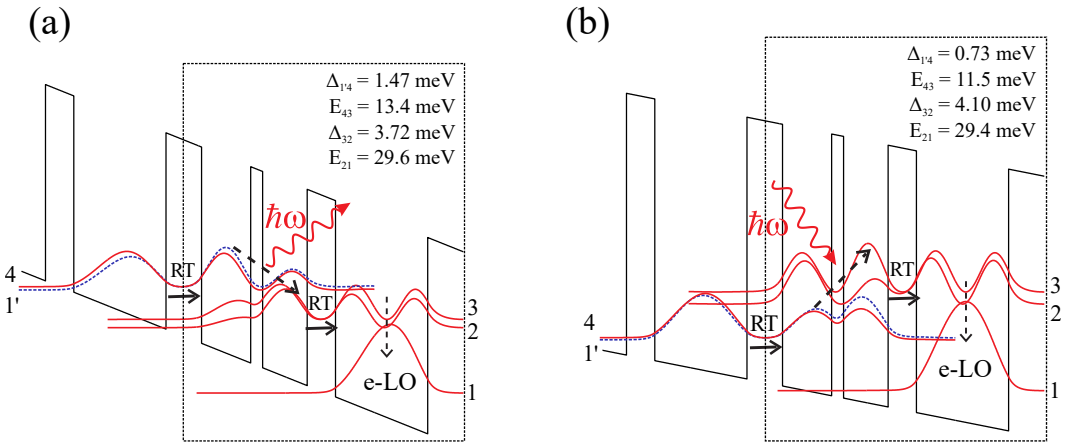

Figure 3.9: Band diagram of TUNDET202 design for emission and absorption alignment respectively. (a) Conduction band diagram at bias corresponding to peak gain (47mV/module) for a THz QCL structure named TUNDET202 that achieves gain from $3.2 - 3.7$ THz. Starting from the injector barrier on the left, layer thicknesses for the GaAs/$Al_{0.3}Ga_{0.7}As$ superlattice in nm are 5.4/8.5/2.3/9.3/6.8/17.5. The average doping in the active region is 6×10^{15} cm^{-3}. (b) Conduction band diagram at lower bias (18mV/module) for the same QCL structure. At this bias, upper laser subband 4 is aligned to phonon subband 2 in depopulation well. Fast LO-phonon scattering depopulates the doublet resulting in intersubband absorption from $3 \rightarrow (2, 4)$, at a frequency that is detuned from QCL's emission frequency.

Close to emission bias of 47 mV/module as shown in Figure 3.9(a), the TUNDET202 design realizes intersubband gain due to the $4 \rightarrow 3$ transition at frequencies in the vicinity of $\sim$ 3.3 THz. As illustrated in Figure 3.9(b), for the same design at a lower bias of 18 mV/module, when electrons are injected into the lower laser subband 3 by resonant-tunneling, the upper laser subband 4 is in alignment with the excited subband 2 in wide phonon well. Electrons have a long life time in lower laser subband since its wavefunction is spatially separated from ground subband's wavefunction. Hence electrons are accumulated in 3, while they are depopulated from subbands 4 and 2 owing to LO-phonon mediated relaxation.

The bandstructure is specifically designed to achieve intersubband absorption due

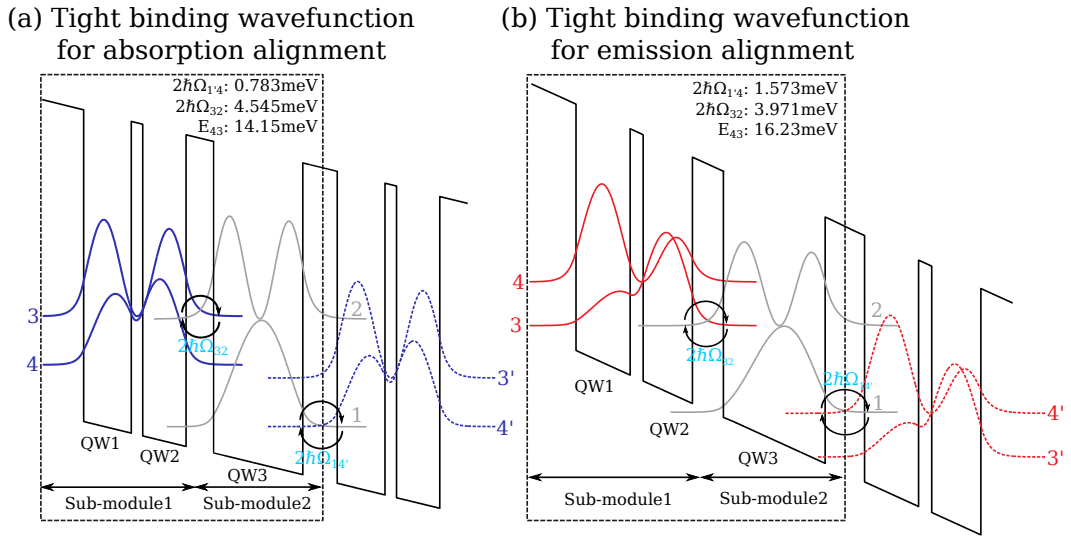

Figure 3.10: (a) Tight binding wavefunction of four level resonant tunneling injection resonant phonon depopulation design TUNDET202 at 48mV/module for emission alignment. One QCL module is splitted into two sub-modules across injector barrier and collector barrier. First sub-module starts from injector barrier (IB) consisting quantum well 1 and 2 and ends with collector barrier (CB). The other sub-module includes collector barrier, quantum well 3 and injector barrier of next module. (b) Tight binding wavefunction of TUNDET202 at 18mV/module for absorption alignment.

to $3 \rightarrow (2,4)$ at a frequency of ~ 2.8 THz, which is detuned by > 0.5 THz from the QCL's emission frequency. Also, the radiative oscillator strength for the absorption transition is kept large (~ 0.65), which necessitates choice of tighter tunneling injection anticrossings in the design as compared to conventional THz QCLs. An intersubband transition modifies the real-part of electric-susceptibility (refractive-index), but only at frequencies detuned from the frequency of the transition. Hence, the loss transition at 2.8 THz introduces changes in the refractive-index of the active medium within its gain bandwidth around 3.3 THz. At the same time, since the absorption transition is detuned, its effect on introducing intersubband loss (imaginary part of electric-susceptibility) at the QCL's emission frequency is negligible.

Density matrix formalism are also used to understand electron distribution among subbands in TUNDET202 design at different bias. TUNDET202 design are broken into two sub-module by injector barrier and collector barrier. Electron transport

across these two barrier are considered only through resonant tunneling as illustrated in figure 3.10

At design bias,illustrated in Figure 3.10(a), electrons are transport from level 1' to level 4 by RT and transport into lower lasing levels, electrons locate in level 3 resonant tunnel to level 2 and depopulate back to ground state 1' by fast LO phonon scattering. The time-evolution of DM for TUNDET202 at design bias is then written as:

$$\frac{\mathrm{d}}{\mathrm{d}t}\begin{pmatrix}\rho_{1'1'} & \rho_{1'4} & \rho_{1'3} & \rho_{1'2}\\ \rho_{41'} & \rho_{44} & \rho_{43} & \rho_{42}\\ \rho_{31'} & \rho_{34} & \rho_{33} & \rho_{32}\\ \rho_{21'} & \rho_{24} & \rho_{23} & \rho_{22}\end{pmatrix} = -\frac{i}{\hbar}\left[\begin{pmatrix} E_{1'} & -\hbar\Omega_{1'4} & -\hbar\Omega_{1'3} & 0\\ -\hbar\Omega_{1'4} & E_4 & 0 & -\hbar\Omega_{42}\\ -\hbar\Omega_{1'3} & 0 & E_3 & -\hbar\Omega_{32}\\ 0 & -\hbar\Omega_{42} & -\hbar\Omega_{32} & E_2\end{pmatrix}, \bar{\bar{\rho}}_{(1',4,3,2)}\right] + \begin{pmatrix} \frac{\rho_{22}}{\tau_{21}}+\frac{\rho_{44}}{\tau_{41}} & -\frac{\rho_{1'4}}{\tau_{d14}} & -\frac{\rho_{1'3}}{\tau_{d13}} & -\frac{\rho_{1'2}}{\tau_{d12}}\\ -\frac{\rho_{41'}}{\tau_{d14}} & -\frac{\rho_{44}}{\tau_{43}}-\frac{\rho_{44}}{\tau_{41}} & -\frac{\rho_{43}}{\tau_{d43}} & -\frac{\rho_{42}}{\tau_{d42}}\\ -\frac{\rho_{31'}}{\tau_{d13}} & -\frac{\rho_{34}}{\tau_{d43}} & \frac{\rho_{44}}{\tau_{43}} & -\frac{\rho_{32}}{\tau_{d32}}\\ -\frac{\rho_{21'}}{\tau_{d12}} & -\frac{\rho_{24}}{\tau_{d42}} & -\frac{\rho_{23}}{\tau_{d32}} & -\frac{\rho_{22}}{\tau_{21}}\end{pmatrix} \tag{3.7}$$

Tight binding wavefunction for TUNDET design at 18 meV/module is shown in figure 3.10 (b). Electrons are transport from subband 1' to subband 3 by resonant tunneling and scattered into both subbands 1 and 4 through LO phonon emission and absorption process respectively. electrons locate in subband 4 resonant tunnel to subband 2 and scattered back to ground state 1' efficiently through LO phonon

scattering. Time-evolution of DM for tight-binding biases at such bias then expressed as:

$$\frac{\mathrm{d}}{\mathrm{d}t}\begin{pmatrix} \rho_{1'1'} & \rho_{1'4} & \rho_{1'3} & \rho_{1'2} \\ \rho_{41'} & \rho_{44} & \rho_{43} & \rho_{42} \\ \rho_{31'} & \rho_{34} & \rho_{33} & \rho_{32} \\ \rho_{21'} & \rho_{24} & \rho_{23} & \rho_{22} \end{pmatrix} = -\frac{i}{\hbar}\left[\begin{pmatrix} E_{1'} & -\hbar\Omega_{1'4} & -\hbar\Omega_{1'3} & 0 \\ -\hbar\Omega_{1'4} & E_4 & 0 & -\hbar\Omega_{42} \\ -\hbar\Omega_{1'3} & 0 & E_3 & -\hbar\Omega_{32} \\ 0 & -\hbar\Omega_{42} & -\hbar\Omega_{32} & E_2 \end{pmatrix}, \bar{\bar{\rho}}_{(1',4,3,2)}\right]$$
$$+\begin{pmatrix} \frac{\rho_{22}}{\tau_{21}}+\frac{\rho_{44}}{\tau_{41}} & -\frac{\rho_{1'4}}{\tau_{d14}} & -\frac{\rho_{1'3}}{\tau_{d13}} & -\frac{\rho_{1'2}}{\tau_{d12}} \\ -\frac{\rho_{41'}}{\tau_{d14}} & -\frac{\rho_{44}}{\tau_{43}}-\frac{\rho_{44}}{\tau_{41}}+\frac{\rho_{33}}{\tau_{34abs}} & -\frac{\rho_{43}}{\tau_{d43}} & -\frac{\rho_{42}}{\tau_{d42}} \\ -\frac{\rho_{31'}}{\tau_{d13}} & -\frac{\rho_{34}}{\tau_{d43}} & -\frac{\rho_{33}}{\tau_{34abs}}+\frac{\rho_{44}}{\tau_{43}} & -\frac{\rho_{32}}{\tau_{d32}} \\ -\frac{\rho_{21'}}{\tau_{d12}} & -\frac{\rho_{24}}{\tau_{d42}} & -\frac{\rho_{23}}{\tau_{d32}} & -\frac{\rho_{22}}{\tau_{21}} \end{pmatrix} \tag{3.8}$$

In order to obtain carrier distribution in steady state solution of equation 3.7 and equation 3.8 are calculated by set left hand side of the equations equals to 0. Diagonal terms of matrix $\bar{\bar{\rho}}$ represent populations in each subband when assuming total population are normalized. Equation 3.3 to 3.6 are used again for obtaining intersubband susceptibility. Figure 3.11 reveals intersubband gain and loss profile corresponding to the transition indicated by dashed arrow in Figure 3.9(a) and Fig 3.9(b). The absorption frequency is detuned $\sim$ 0.5 THz away from lasing frequency, thus the χ' induced by absorption is negative when χ' induced by lasing transition is zero. As suggested in Figure 3.11(b), the intersubband absorption can lead to large change in real-part of susceptibility (refractive-index) at the QCL's emission frequency.

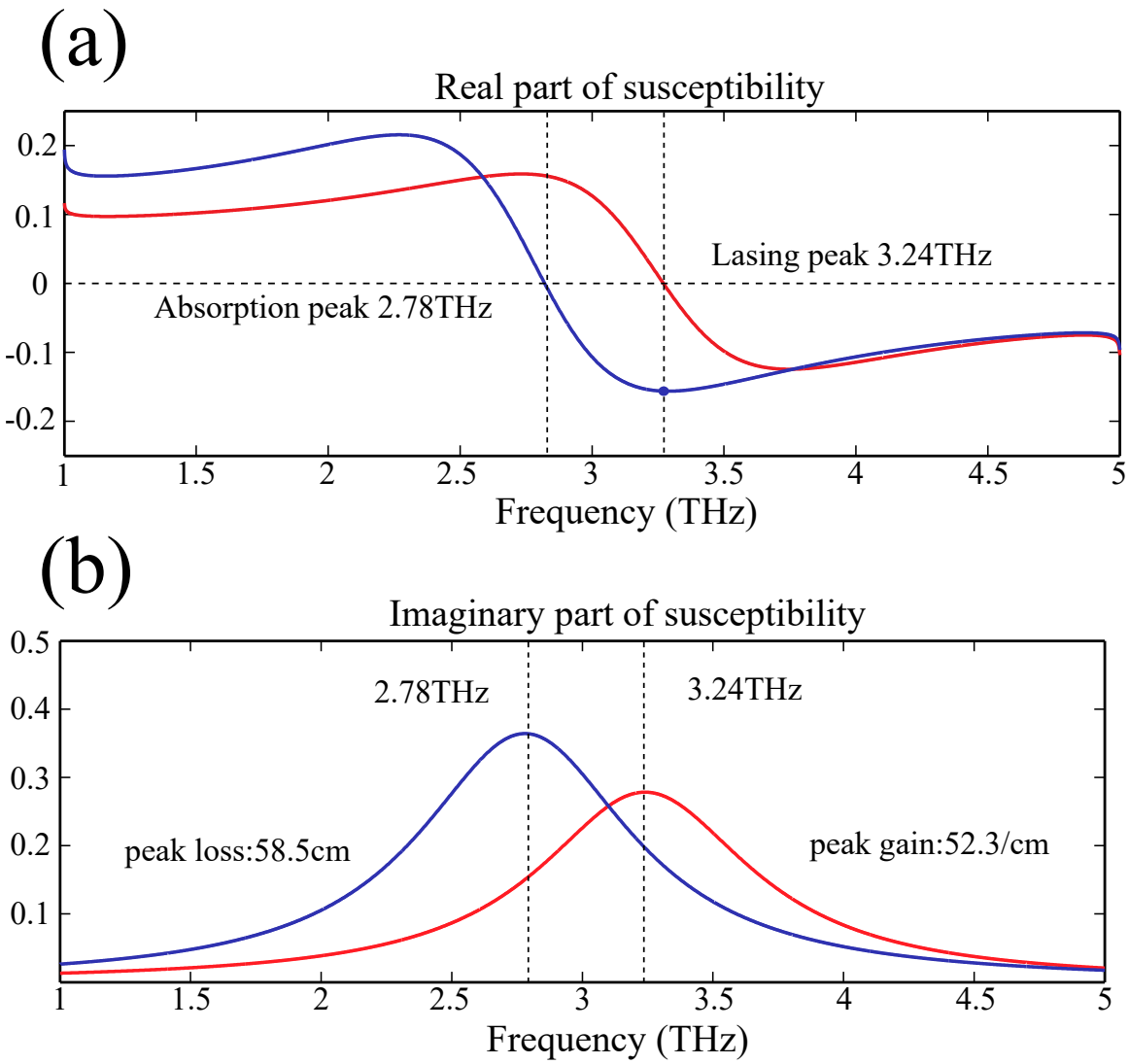

Figure 3.11: Both real and imaginary part of intersubband susceptibility induced by transition between radiative subbands for emission and absorption cases are illustrated. Detuned intersubband absorption have nonzero real part susceptibility hence modify refractive index at emission frequency. Electron distribution among subbands is calculated following [21]. Gain and loss profiles are assumed to be Lorentz shape with FWHM as 4 meV.

3.4.2 Experimental results: electrical tuning with coupled DFB microcavities

As shown schematically in figure 3.12(a), A specific coupled microcavity architecture based on metallic waveguides is developed to achieve tuning by utilizing the unique quantum-transport properties of the active region mentioned above. Two symmetric

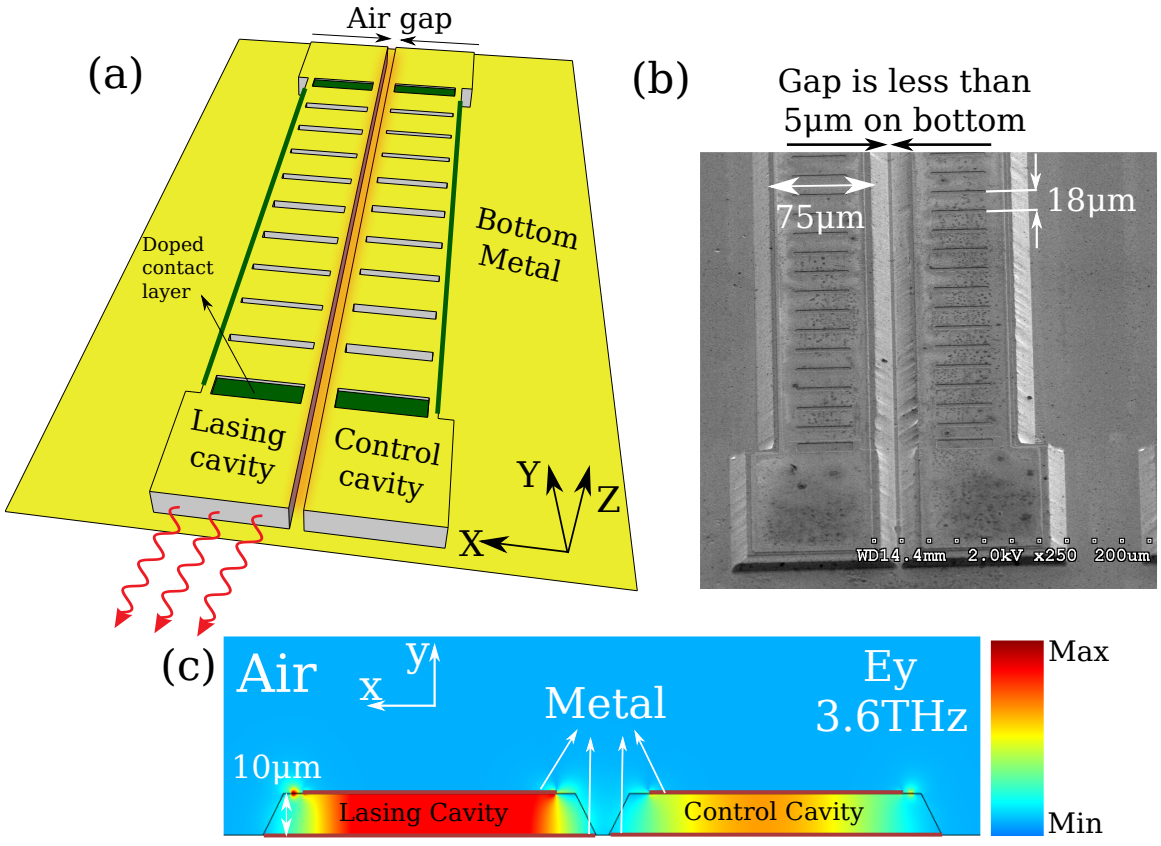

Figure 3.12: (a) A schematic illustrate coupled metallic cavity. Two symmetric distributed-feedback (DFB) QCLs is fabricated laterally close to each other. A narrow gap enable the coupled cavity electrically isolate to each other while optically coupled at THz regime. One QCL is bias above threshold and refer as lasing cavity, the other QCL is bias around absorption regime thus real part of electrical susceptibility in lasing cavity could be modified by changing control cavity bias. (b) SEM image of real device. (c) The optimal parameters of the coupled cavity were found by performing finite element two dimensional simulations using a commercial software (Comsol Multiphysics). Eigen-mode analysis indicating that two 75 μm ridges separating by 5 μmm gap on bottom with double metal waveguide can coupled by each other at 3.5 THz.

distributed-feedback (DFB) QCLs are designed on mask, and fabricated laterally adjacent to each other with a narrow gap ($\sim$ 5 μm at bottom) to form optically coupled-cavities, facilitated by the large lateral mode extent at THz frequencies. The DFB is based on antenna-feedback method that is described in Ref. [138]. Lateral loss boundary formed by a 50 nm thick heavily doped contact layer are only kept in outer edge to kill higher order lateral mode as well as enhance coupling strength. The

two DFB QCLs are electrically isolated and can be biased individually. As shown in Fig3.12(b), the width of each ridge is 75 μm and the length is 1.35 mm. One DFB cavity is biased to operated as a laser in the emission regime and is referred as "lasing cavity" while the other DFB cavity is biased in its absorption regime and is referred as the "control cavity". The measurements are performed in pulse mode in order

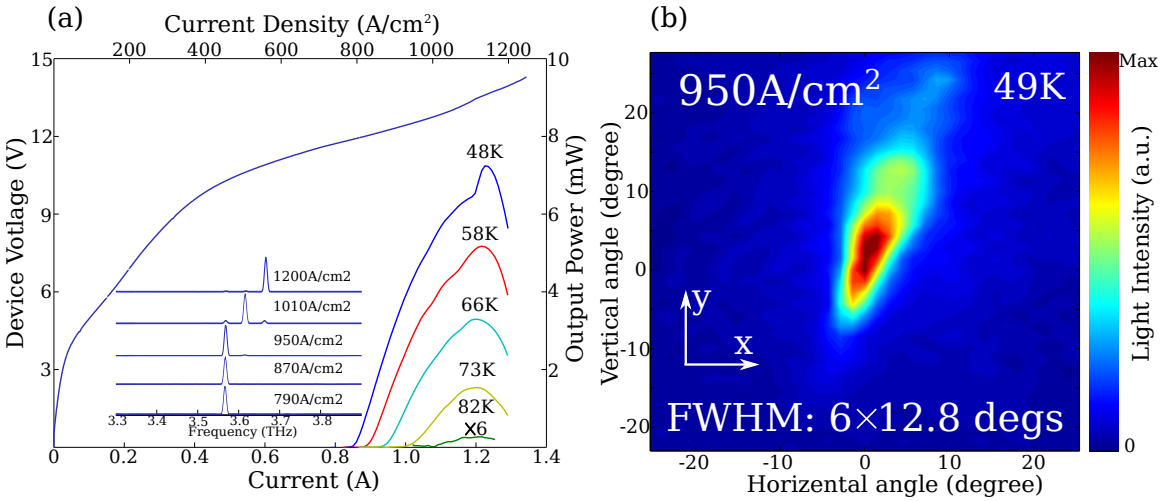

Figure 3.13: (a) Temperature depended LIV for lasing cavity when it is biased alone. Device is mounted inside a vacuum chamber and cooled by a electrically operated Stirling cryocooler. At 48 K threshold current density is 770 A/cm^2 and peak current density is 1140 A/cm^2. The peak optical power emitted from lasing cavity is 7 mW. The maximum operating temperature for the device is 82 K. Inserted beam pattern is measured at 48 K by pyroelectric detector placed 40 mm away from the device and scanned in both horizontal and vertical direction mechanically. Lasing cavity is biased at 950 A/cm^2 corresponding to lase at 3.568 THz in single mode. Insert of (a) Spectra taken at 48 K of lasing cavity at different current density. Laser is biased in pulse mode with pulse repetition rate of 100 KHz and pulse width of 200 ns. (b) Far field beam pattern measured at 49 K when device is bias at 950 A/cm^2. Pyroelectric detector [1] are placed $\sim$ 40 mm away from THz QCL facet and mechanically scanned by a step of 1 mm. A FWHM of 6×12.8 degree indicating lasing mode in lasing cavity is extended in both vertical and horizontal direction.

to prevent large change of device temperature and the failure of bonding wire. I-V, L-I, emission spectrum and far field beam pattern of lasing cavity are measured at 48 K when operating inside a Stirling cryocooler. The light emitted from the QCL is detected by a pyroelectric detector then peak output power is calibrated through an

absolute power meter. Illustrated in Fig 3.13(a) at 48 K threshold current density is 770 A/cm^2 while peak current density is 1140 A/cm^2. When bias at lasing cavity's peak current density a optical output power of 7 mW is obtained. As depicted in insert of Figure 3.13(a) spectra of lasing cavity are plotted from threshold all the way beyond the peak. From threshold to about 950 A/cm^2, the QCL lasing at single mode at 3.568 THz. If further increase bias lasing cavity emit at three frequency 3.568 THz, 3.616 THz and 3.664 THz. When bias around peak and beyond, 3.664 THz peak become dominant mode for lasing cavity. This phenomenon can be attributed to lack of doped contact layer on inner side of lasing cavity. The spectra are characterized by a commercial Fourier-transform-infrared spectrometer (FTIR) equipped with a DTGS pyroelectric detector and a Silicon beamsplitter. The measured spectrum resolution is limited by 0.0618 cm^{-1} (1.856GHz). Far-field beam patterns from lasing cavity at 950 A/cm^2 measured using a pyroelectric detector located $\sim$ 40 mm away from the QCL and mechanically scanned over $\pm 30^\circ$ in both horizontal and vertical directions. Observed beam has a full width half maximum of 6×12.8 degrees. This two dimensional narrow radiation pattern implies that such mode extend significantly in both vertical and horizontal direction.

A pair of symmetric DFB QCLs are fabricated laterally adjacent to each other with a narrow gap (~ 5 μm on bottom) to form optically coupled-cavities, facilitated by the large lateral mode extent at THz frequencies. The two ridges are electrically isolated and can be biased independently. Tunable THz QCL device is mounted inside a vacuum chamber and cooled down to 48 K by a Stirling cryocooler (Sunpower). THz radiation is emit out of vacuum chamber via a TPX window, and collected by FTIR. Through out measurement both FTIR and dewar are continuously pumped. A temperature sensor (Lakeshore) is mounted neighboring to the device to monitor temperature in real time. During tuning experiment a pulser(AVTECH) generate a pulse chain of 50 kHz repetition rate and 200 ns pulse width supplies constant

voltage upon lasing cavity. Simultaneously, another pulser generate another pulse chain whose repetition rate is also 50 kHz however its pulse width is doubled to 400 ns. By properly adjusting relative phase between these two pulse chains, each 200 ns wide pulse will embedded inside the 400 ns wide pulse. Bias conditions are visualized and monitored by oscilloscope (Agilent) throughout all measurements.

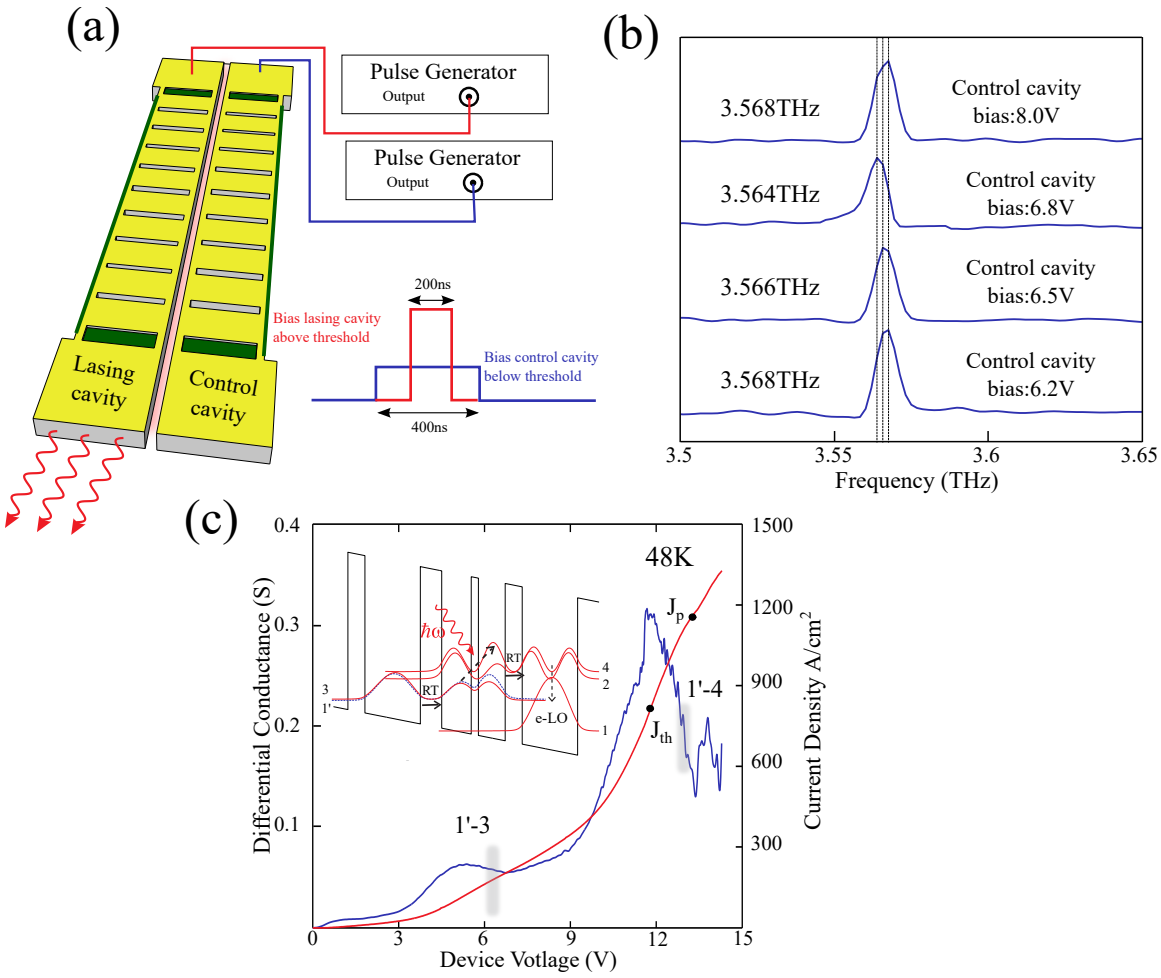

Figure 3.14: (a)Schematic of tuning measurement set-up. One of the laser in coupled cavity system is biased above threshold and its bias keeping as a constant during tuning experiment. Control cavity bias varies enable intersubband absorption to change resonant frequency in lasing cavity.Both QCL ridges are biased in pulse mode to prevent heating issue. (b) Spectra measured from FTIR demonstrate that continues 4 GHz tuning in lasing cavity when changing control cavity bias from 6.2V to 6.8V. (c) Differential conductance plot suggest that tuning happened at the bias when subband 1' resonant with subband 3 thus detuned intersubband absorption leads to the frequency change.

During tuning experiments the bias of of the lasing cavity is kept at 950 A/cm^2 where it lases at single mode as shown in insert of Figure 3.13(a). The control-cavity is biased below lasing threshold throughout all experiments, thus it only contributes to intersubband absorption. When the bias of control-cavity is increased from 6.2 V to 6.8 V, emission from the lasing-cavity is continuously tuned by 4 GHz as shown in fig 3.14(b). When further increase bias in control cavity, the emission peak shift back to original resonant frequency. This is because further increase in bias misaligns all subbands, due to which both energy separation and carrier distribution change dramatically. Temperature variation caused by device current increasing in control cavity is within 1 K, eliminating influence from temperature on refractive index. Following the analysis in ref [67], G-V (differential conductance versus voltage) characteristics is plotted in Fig 3.14(c). The differential-conductance G (slope of the I-V curve) highlights some of the key transport characteristics of TUNDET202 design. Each conductance peak could be associated with a specific resonant-tunneling alignment that facilitates current flow across the superlattice. The resonance condition leads to a local maxima in the I-V curve, which corresponds to a local minima in the G-V curve. Tuning happened when control cavity bias is around 6.5 V which matches the bias range within which differential conductance have a drop. Since before design bias there is no subband alignment other than 1' to 3 can lead to resonant tunneling. The bias range we observe tuning clearly correspond to the band diagram illustrated in insert of Figure 3.14(c).

3.5 Conclusions and Summary

In conclusion, a new tuning method for THz QCLs is demonstrated, which utilizes susceptibility change induced by detuned intersubband-absorption. Unlike cavity-pulling induced by intersubband gain, the tuning phenomenon occurs within a very

narrow voltage range that induces tuning, which is a significant advantage of our tuning method. For SARP172 device, two QCL ridges with metal-metal waveguide are mounted and characterized. Electrical tuning for a 2.2 THz QCL up to 5 GHz are firstly demonstrated at liquid nitrogen temperature. For TUNDET202 active region, two closely placed antenna DFB with very narrow far field emission pattern are fabricated and characterized. 2D narrow beam from lasing cavity is a strong evidence that lasing mode is extended laterally thus two antenna DFB formed a super-cavity. The lasing cavity could be kept at a fixed voltage, which allows this method to tune a THz QCL even if it is operating at high-temperatures. Electrical-tuning of 4 GHz for a $\sim$ 3.6THz QCL is demonstrated for the first time at 48 K.

Chapter 4

Broadband Refractive Index Sensor Based on THz QCL Arrays

4.1 Introduction

4.1.1 Applications of THz sensing, existing techniques, and challenges

It has long been known that the THz/far-infrared region of the spectrum ($\nu \sim 1-10$ THz, $\lambda \sim 30-300$ μm, photon energy $h\nu \sim 4-40$ meV) is ideal in many ways for chemical and biological sensing, imaging, and spectroscopy [42]. Many molecular species have very strong characteristic THz rotational and ro-vibrational transitions (both inter and intra-molecular), and hence could be "fingerprinted" with THz spectroscopy. While the vibrational modes that show up in infrared (IR) or MIR are usually localized within specific regions of a molecule, the THz modes involve collective motions of all atoms in a molecular structure, and hence each vibrational mode has a distinct spectral signature unlike in IR. THz sensing could be applied to cell biology [143] for example, since biomolecular THz spectra changes when they are

bound in various ways to water molecules, due to a change in their conformation and function. The extreme sensitivity of THz to solid forms of materials and the presence or absence of water in these materials has obvious applications in process engineering, crystal engineering, pharmaceutical quality control and identification of counterfeit drugs. Currently, all THz spectroscopy is done with non-linear THz sources that generate low average THz power of the order of 10 μW that makes these systems very complex and expensive. Because of low source power and high THz attenuation in liquids (of the order of $100 - 1000$ cm^{-1} [60]), liquid-phase THz spectroscopy is significantly more challenging, and therefore considerably underdeveloped.

4.1.2 Existing QCL Based Optical Sensors

Laser based chemical sensors can be realized in a large number of modalities, and sense the absorption or refractive-index of the analyte at a single or range of frequencies. For gas sensing, absorption spectroscopy is most common, however, chemicals in condensed and liquid phase are sensed using evanescent-wave techniques that affords sensitive detection with small sample volumes. For spectroscopic evanescent-wave sensing of liquid and solids, however, more complex techniques such as attenuated total reflectance infrared spectroscopy (ATR-IR), or scattering-type scanning near-field optical microscopy (s-SNOM) are often utilized. In gaseous phase, tunable-diode and intracavity laser absorption spectroscopy (TDLAS and ICLAS) respectively are commonly used techniques. Photoacoustic spectroscopy (PAS) can be used for gases, solids, or liquids. Most of these techniques require, either a broadly tunable laser source with single-mode operation and good beam quality, or need a high-power broadband source in combination with a spectrometer. MIR QCLs have now reached a level of maturity that MIR sensors based on most of the above mentioned techniques have recently been demonstrated, such as s-SNOM, PAS, ICLAS. Simpler liquid-phase sensors based on direct absorption have also been demonstrated [17, 26].

Development of THz QCL based sensors, however, is far from where MIR QCL based sensors stand because of the challenges associated with cryogenic cooling, and lack of methods for electrical tuning owing to the microcavity configuration of metal-metal cavities used for THz QCLs. Only few reports for absorption based sensors with THz QCLs have been published, such as the recent result in Ref. [30]. A quartz enhanced photo-acoustic sensor employing a single-mode quantum cascade laser for gas sensing purpose is another example of QCL based sensor [16, 106]. As opposed to chemical sensing, some work has been reported toward development of THz radar imaging with QCLs [127, 99].

4.1.3 Overview of the proposed sensing scheme with DFB QCL arrays

THz QCLs [134, 108] are required to be cryogenically cooled although they can now operate above 160 K when designed to emit in the frequency range of $\nu \sim 2-5$ THz. For sensor development, stable frequency and high average power mandates single-mode cw operation. However, such THz QCLs can only operate up to temperatures of $80-100$ K and the cw power output is of the order of 1 mW above liquid-Nitrogen temperature. THz QCLs have additional challenges. Their cavities confine the optical mode in sub-wavelength dimensions and hence the commonly used external-cavity tuning technique is not applicable with the low-loss metallic cavities. The lack of electrical methods to tune frequency and low output power make it difficult to devise a sensing scheme with THz QCLs based on intensity interrogation because of challenges related to interference and noise, and more so when spectroscopic sensing is desired by utilizing an array of single-mode QCLs that operate at different frequencies, which will then involve challenges with beam combining and intensity calibration.

This work seeks to overcome the aforementioned limitations of present THz QCLs and proposes a scheme to realize highly practical and affordable, yet sensitive and

functional THz spectroscopic sensor instrument with a small footprint for condensed or liquid-phase sensing with small sample volumes.The key idea is to utilize pairs of single-mode distributed-feedback (DFB) THz QCLs at an array of frequencies. One QCL of each pair (i. e. the *sensing* QCL) then probes the complex refractive-index of the analyte in reflection mode. Depending on the sensitivity desired, the analyte could very well be present at a distance of few meters from the cryocooler in which QCLs are mounted. The reflected signal couples back into the lasing cavity and thus shifts its resonant-frequency. The shift in the resonant frequency is indicative of the refractive index of the analyte, and is down-converted to microwave regime by mixing the optical mode of the sensing QCL with another *reference* QCL using intracavity frequency mixing [34]. The recently demonstrated antenna-DFB scheme [138, 137] is utilized to enable strong optical coupling of reference and sensing QCLs, which would otherwise be very weak due to the microcavity geometry of metal-metal THz QCL cavities. Frequency interrogation (i. e. measurement in frequency shift due to analyte) is inherently immune to noise and interference but typically requires a spectrometer. However, the fact that "electronic" mixing still works at THz frequencies, integrated/on-chip mixing is possible without the need of expensive photonic components. This could be used to efficiently down-convert the sensed THz signal to microwave frequency region. Hence, all that is needed to record the sensed data is a microwave spectrum analyzer working below 5 GHz, and a low-cost handheld spectrum analyzer would work appropriately. The need for expensive THz detectors as well as a THz spectrometer is completely eliminated, whereas the functionality attained can be similar to other advanced spectroscopy techniques.

4.2 Description of the sensing scheme

The best performing THz QCLs are implemented in parallel-plate metallic cavities [135] similar to microstrip transmission lines at microwave frequencies, owing to low optical loss in metals at long wavelengths [71]. Whereas metallic ridge cavities are excellent for THz mode-confinement, their spectral and modal characteristics make it difficult to implement many techniques that are used for conventional diode lasers. First, such lasers excite several lateral and longitudinal modes simultaneously, invariably leading to multi-mode lasing across the gain bandwidth, which is typically up to 0.5 THz around the designed frequency. Second, THz QCLs with such ridge-cavities have very poor diffractive beam patterns due to the sub-wavelength dimension of the emitting facets [7]. To achieve single-mode lasing and radiation in a narrow beam, distributed-feedback (DFB) has been implemented in various ways by implementing periodic photonic structures lithographically in such cavities. Different types of DFB THz QCLs have been developed such as the ones with a first-order [96], second-order [79], third-order [10] gratings respectively.

The proposed work requires to implement a pair of coupled DFB lasers that emit at almost similar frequency (within lithographic variations that could result in a frequency difference of few GHz). One QCL will be termed as the *sensing QCL* and the other as the *reference QCL*. There are two primary requirements. First, the two DFBs should lead to emission in different directions. This is because the sensing QCL emits radiation towards analyte, a fraction of which is then reflected back into the same cavity and hence alters the resonant frequency of the QCL as a function of the complex refractive-index of the analyte. The resonant-frequency of the second QCL should, however, remain unaffected by the presence of the analyte, and hence it should radiate in a different direction. The second requirement is that both QCL cavities need to have strong optical coupling. This aspect is discussed in the subsequent section. For the proposed sensor, we choose to implement a second-order

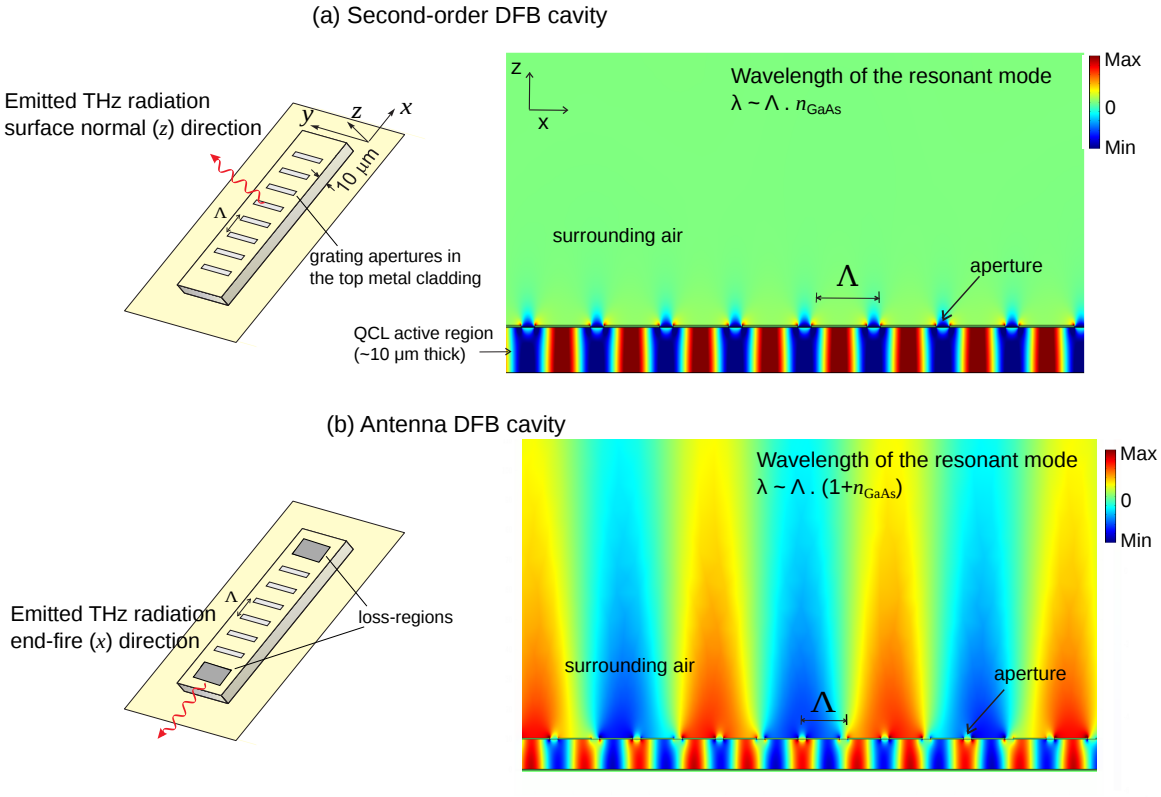

Figure 4.1: Second-order DFB and Antenna DFB metallic cavities for single-mode THz QCLs emitting in different directions. (a) Three-dimensional schematic of a conventional second-order DFB THz QCL [79] in which the second-order Bragg diffraction from a periodic grating in the top-metal cladding leads to distributed-feedback inside the cavity for a wavelength of the mode such that $\lambda_{\mathrm{GaAs}} \equiv \lambda_0/n_{\mathrm{GaAs}} \approx \Lambda$ where Λ is the lithographically introduced grating period and λ_0 is the free-space wavelength of the resonantly excited DFB mode. The dominant TM polarized (E_z) electric-field for the (designed) lowest-loss second-order DFB resonant mode is plotted along x, calculated using a finite-element electromagnetic solver [2]. (b) Similar schematic of an *antenna-DFB* cavity that was recently demonstrated [138, 137]. For a grating period Λ, a mode with $\lambda_0 = (n_{\mathrm{GaAs}} + 1)\Lambda$ is excited for air as the surrounding medium. This periodicity couples a surface-plasmon mode propagating in air on top of the metal-cladding of the laser cavity, to the guided field inside the cavity such that a large fraction of standing-wave exists as evanescent-field on top of the cladding. The dominant TM polarized (E_z) electric-field for the (designed) lowest-loss antenna DFB resonant-mode is plotted along x.

DFB cavity similar to that in Ref. [79] and an antenna-DFB cavity similar to that in Ref. [138, 137]. The schematic and optical mode-shapes of the lowest-loss DFB resonant-cavity mode for each of the cavities are shown in Fig. 4.1. The emission from the second-order DFB QCL is in surface-normal (z) direction whereas the emission from the antenna-DFB QCL is in the end-fire (x) direction.

4.2.1 Strong optical coupling between longitudinally adjacent DFB cavities

In the proposed scheme, the shift in resonant-frequency of the sensing THz QCL is recorded, which is then indicative of the refractive-index of the analyte at that frequency. As shown subsequently, this shift in the resonant frequency is of the order of $\sim 1 - 1000$ MHz, and hence could be measured by a microwave spectrum analyzer so long as frequency could be downconverted to a microwave regime. The reference THz QCL serves the required purpose of downconversion. The optical field from the sensing QCL is coupled strongly to the reference QCL, by aligning the cavities longitudinally on the mask. As the field leaks into the adjoining coupled cavity, intracavity non-linear mixing in the QCL gain medium produces a microwave difference frequency signal, that could then be extracted from the bias terminals of each QCL, or could even be picked from a free-standing coaxial connector inside the vacuum dewar inside which the QCLs are mounted for cooling. This is because the microwave signal thus generated will also be radiated from each of the QCL cavities inside the cryocooler dewar compartment.

In the proposed sensing scheme, one of the cavities is a second-order DFB cavity and the other is an antenna-DFB cavity. As described later, either of the cavities could be utilized as a sensing cavity, and then the other one becomes the reference cavity. The primary reason for choosing antenna-DFB scheme instead of some other DFB scheme (such as first-order DFB [96, 136] or third-order DFB [10]) is that a

large fraction of the optical field exists as standing-wave on top of the antenna-DFB cavity, that significantly enhances the coupling efficiency into the adjoining coupled cavity. While the longitudinal absorbing regions [33] (as illustrated in Fig. 4.1b) are needed for correct operation of the antenna-DFB cavity, they are not to be used for the second-order DFB cavity to enhance coupling. This is because for optical field to couple from antenna-DFB to second-order DFB cavity (and vice-versa), the second-order DFB cavity must radiate from its end-facets as well, which will not happen if absorbing regions are utilized. For this reason, the phase of reflection from the end-facets needs to be taken into account for design of second-order DFB cavity as in Ref. [79].

The coupling strength are all performed by commercial available Finite element solver COMSOL[2]. Simulation details about obtaining electromagnetic field, Eigen-frequency, optical coupling strength are focused on section 4.3. This this section we only talk about simulation result regrading enhance optical coupling between adjacent cavities. For the coupling calculation, the length of antenna DFB and second-order DFB were chosen to be 1.3 mm and 0.6 mm respectively and the cavities were separated by 100 μm. The choice of these dimensions and cavity-spacing is somewhat arbitrary and hence flexible. However, the shorter the length of the second-order DFB cavity, the greater is the coupling because larger field exists at its end-facets. The center frequencies between antenna DFB and second-order DFB was detuned by 0.8 GHz by choice of grating periods for simulation. Note that the difference in frequency of reference and sensing QCLs needs to be known beforehand, but need not be a certain value for each pair of QCLs (so long as it is less than 5 GHz for it to be measurable by a low-cost microwave spectrum analyzer). The sensing data is the *shift* in the resonant-frequency of the sensing QCL when analyte is introduced. As shown in Fig. 4.2 the field coupling from antenna DFB to second-order DFB is significant. Although it is difficult to estimate the non-linear conversion efficiency,

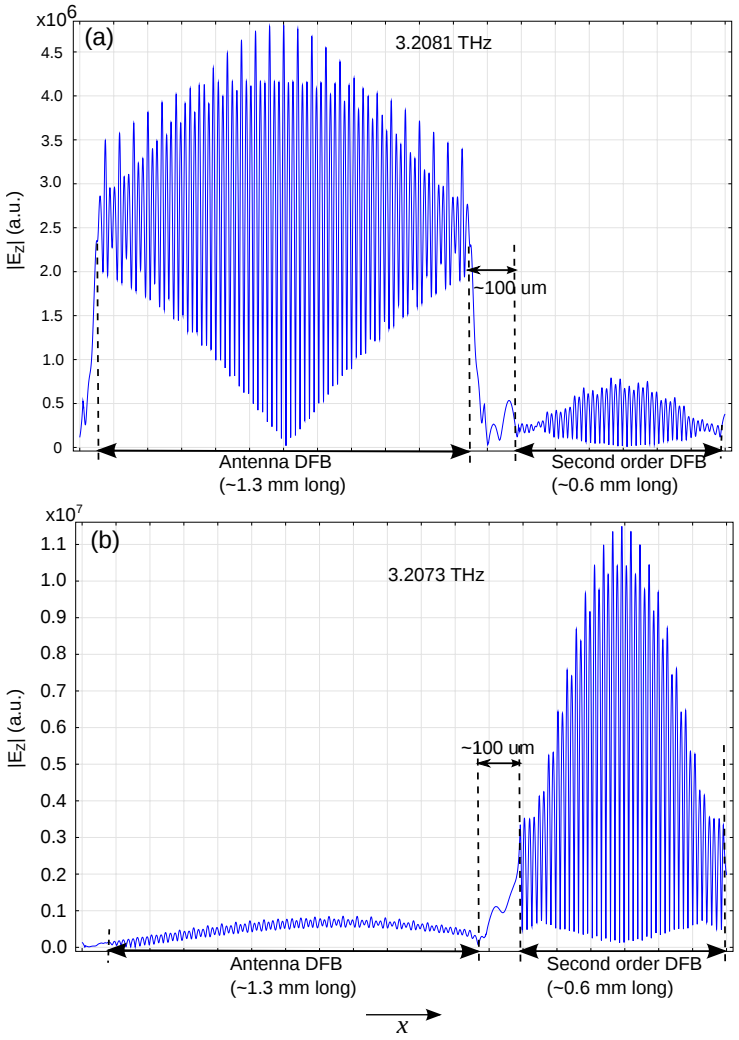

Figure 4.2: Coupling between sensing cavity and reference DFB cavities. Finite-element simulation for demonstrating the optical coupling between sensing and reference DFB cavity. The results from a finite-element two-dimensional simulation (assuming cavities of infinite width) are shown. The optical field for the lowest-loss resonant-cavity modes for respective cavities are plotted along the length of the cavities. The cavities are aligned longitudinally (i. e. in x direction) with a spacing of 100 μm between the end-facets. The antenna-DFB cavity is $\sim$ 1.3 mm long and is designed with grating period $\Lambda = 21$ μm, with absorbing regions of length 40 μm at both ends (see the schematic in Fig. 4.1). The second-order DFB cavity is $\sim$ 0.6 mm in length and is designed with $\Lambda = 26.6$ μm, without any absorbing regions. For the chosen grating periods, the resonant-modes for each cavity occur at frequencies separated by $\sim$ 0.8 GHz. The TM field $|E_z|$ is extracted from the center location of cavity's height and is plotted as a function of longitudinal dimension. (a) When the mode is localized within the antenna-DFB, significant field couples in to the second-order DFB cavity. The peak amplitude of the electric-field in second-order DFB cavity is $\sim$ 15% of that in the antenna-DFB cavity. (b) When the mode is localized within the second-order DFB cavity, its coupling to antenna DFB is smaller at $\sim$ 8%, but still significant.

it is well known that strong intracavity mixing occurs in THz QCL cavities [34, 18]. A microwave-signal produced as a result of the intracavity mixing (designed to be < 5 GHz) will appear on the biasing terminal of both DFB cavities, although it will be stronger on the biasing terminal of the second-order DFB QCL because of the larger coupled field inside second-order DFB cavity compared to the antenna-DFB cavity. This microwave signal can be extracted by a bias-T in the external coaxial connectors of the cryocooler. Alternatively, an open coaxial connector could be placed inside the cryocooler compartment that will pick up the radiated microwave signal in the compartment.

4.2.2 The sensing architecture

A surface-emitting second-order DFB QCL in combination with antenna-DFB QCL placed face-to-face forms the vital element of proposed sensor architecture, which is described in Fig. 4.3. Each pair of DFB QCLs will be designed with proper geometry and grating period so that their nominal emission frequency is almost the same. However, taking standard fabrication/lithographic variations into account, it is expected that the lasing frequency of the two QCLs in each pair could be within few GHz of each other. An array of single-mode DFB THz QCLs on a semiconductor chip of typical dimension 2 mm $\times$ 2 mm will be mounted inside a Stirling cryocooler that is cooled down to ~ 70 K. This will allow operation of QCLs in continuous-wave (cw), which is possible for present active-region designs. Note that multiple such chips with QCLs processed from different active regions could be simultaneously mounted, with the capacity to cover the entire THz spectral region in which cw operation above ~ 60 K is available for single-mode QCLs, which is approximately the frequency region of $2 - 4.5$ THz. Relatively low-cost cryocoolers, such as the Cryotel GT model from Sunpower, Inc.,[6] are now available with relatively modest electrical-power requirements and small weight that can allow operation with a portable setup.

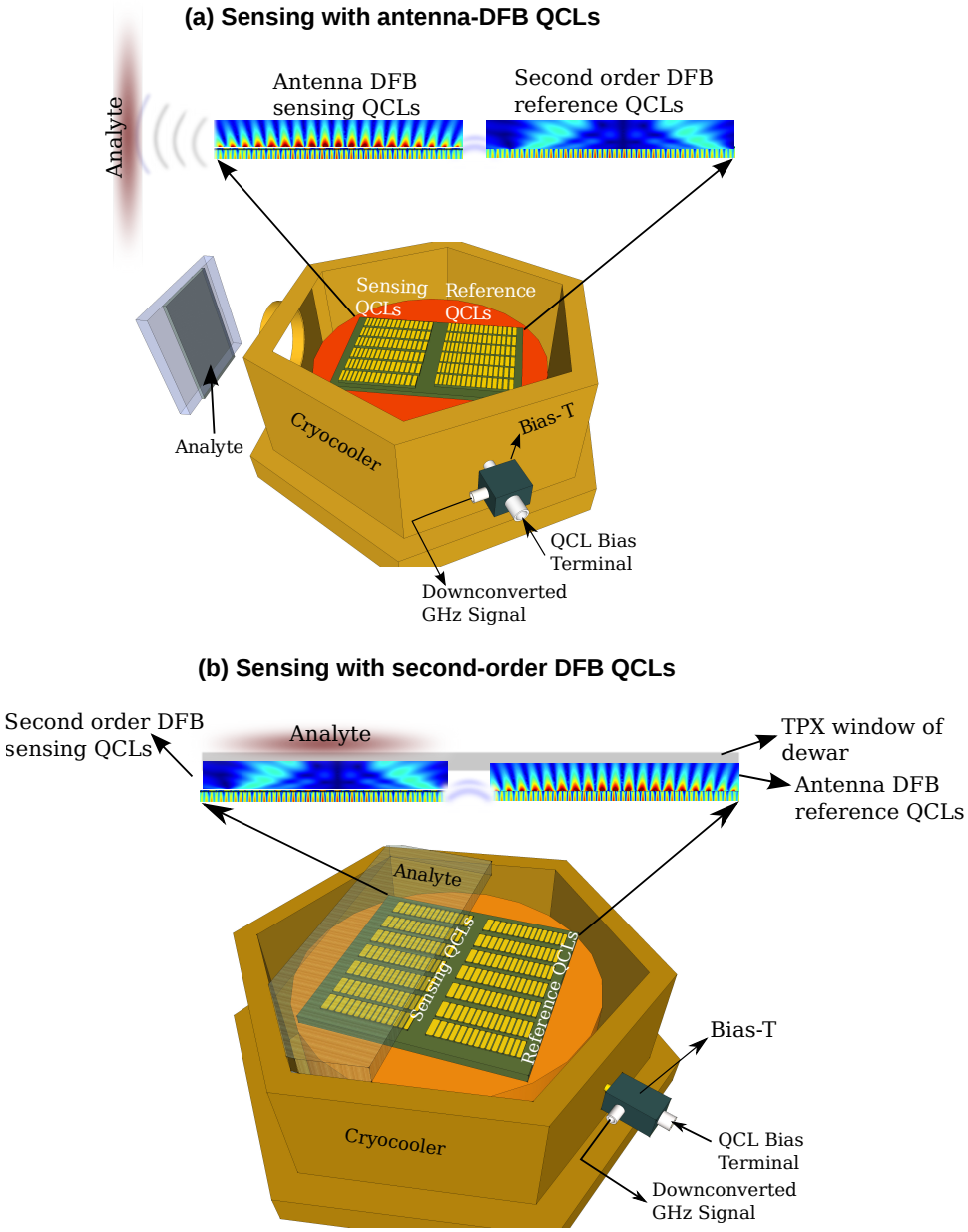

Figure 4.3: Proposed architecture of the THz sensor instrument. Two sensing schemes are possible: (a) In this scheme, antenna-DFB QCL emitting in the end-fire direction works as a sensing cavity while surface-emitting second-order DFB acts as a reference cavity. The radiation from the sensing QCL is partially reflected back into the cavity, and the amplitude and phase of the reflected wave changes the resonant-frequency of the sensing QCL according to the complex refractive index of the analyte. Since emission from the second-order DFB is in surface-normal direction, the resonant-frequency of reference QCL is not impacted by the properties of the analyte. (b) In this scheme, the second-order DFB QCL works as a sensing cavity while antenna-DFB QCL works as reference cavity. For this reason, the analyte is now to be placed vertically above the second-order DFB QCLs. The remainder of the operation with this scheme is similar to (a); however, the response characteristics for this scheme are different than that of the antenna-DFB scheme as discussed in main text.

'n' pairs of sensing and reference QCLs will be designed for emission at discrete frequencies f_n by lithographically implementing the appropriate grating periods. QCLs will be located on chip such that only the sensing QCL out of each pair will be affected by analyte during operation. The analyte in condensed or liquid phase will be placed outside the dewar in a channel or vial made of a material such as high-density polyethylene (HDPE) or polymethylpentene (TPX) with low THz absorption. Similarly, the dewar's window will be made of TPX or HDPE. The resonant-frequency of n-th sensing QCL depends sensitively on the complex refractive-index of the analyte at frequency f_n. THz field from sensing and reference QCLs are mixed in the QCL cavities itself. For intracavity mixing, cavities are placed adjacent to each other longitudinally and are kept electrically isolated. The microwave beat signal (generally in an order of GHz) will be relayed outside the dewar and can be extracted by a bias-T in the external coaxial connector and measured by microwave spectrum analyzer. The frequency of the microwave signal from n-th pair of QCLs is representative of the refractive-index of the analyte at frequency f_n. Each pair of QCLs could be electrically cycled and hence, the dielectric response of the analyte could be measured at the entire range of frequencies in which the QCLs are implemented for broadband sensing. The speed of cycling through the spectral range is dependent on measurement speed of the microwave spectrum analyzer, and the entire measurement could potentially be done within a time-frame of couple of seconds for scheme consisting of tens of pairs of DFB QCLs. Finally, sensing of the analyte in a standoff scheme is also possible because of the reflection mode sensing scheme. The scheme shown in Fig. 4.3(a) is more amenable in this situation because antenna-DFBs emit radiation in an extremely narrow beam ($\sim 5 \times 5^\circ$ [138]), and hence, relatively high-sensitivity should be obtainable for distances in the range of few meters. However, note that, as shown subsequently, sensitivity calculations were performed for the case in which analyte is placed in proximity of the cryocooler. The finite-element model used for

numerical calculations in this work cannot estimate the results for standoff-sensing due to memory limitations for full-wave electromagnetic modeling of large geometries.

4.3 Finite-element Electromagnetic Simulations

In order to find shift of resonant frequency with and without analyte, a commercial finite element Electromagnetic solver COMSOL 4.4 is used to calculate electromagnetic mode eigen frequency [2]. Details of eigenmode simulation are illustrated below:

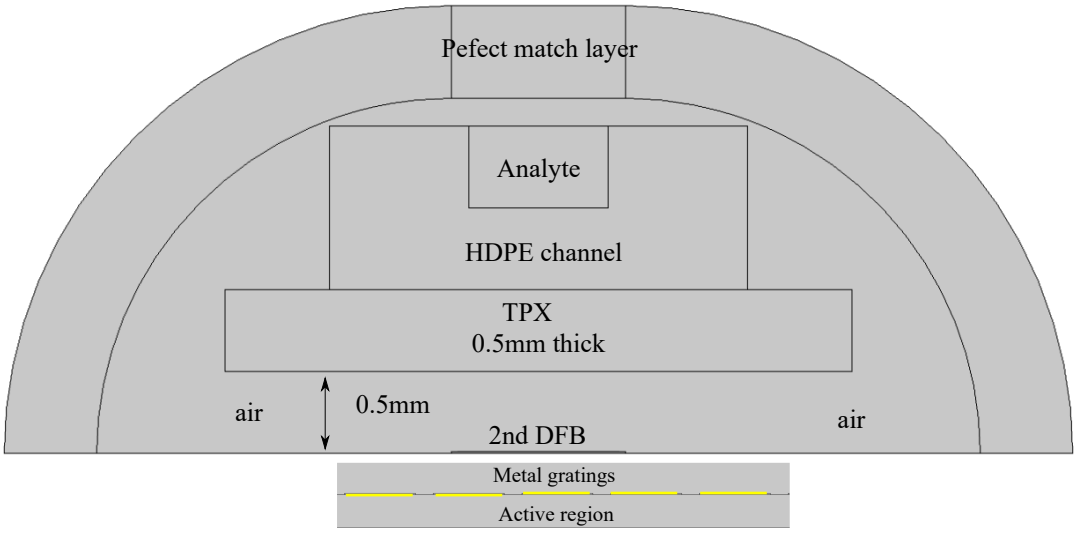

Figure 4.4: Geometry used for 2^{nd} order DFB eigen frequency simulation.

A $\sim$ 1.2 mm long 2^{nd} order DFB is build use COMSOL GUI, there are 40 μm longitudinal doped contact act as loss section. A 4mm long, 0.5mm thick TPX layer is build to represent TPX window of cryocooler vacuum chamber. On top of TPX layer is a micro-fluid channel made of HDPE. The analyte is filled within HDPE channel, which in our case is ice water. The HDPE channel is 1 mm wide and 0.5 mm high. HDPE and TPX refractive index is set as 1.54 and 1.46 receptively. As shown in figure 4.4, HDPE, TPX and air are all set to be lossless. COMSOL default setting for outer most boundary is perfect electric conductor (PEC). Mathematically this boundary condition requires electric filed intensity vanish to zero at the boundary.

Physically outer boundary act as perfect mirror for all frequency incident electromagnetic field. This boundary condition will lead to result does not make physical sense. Thus a perfect match layer whose imaginary part of permittivity increase gradually along radius direction on two side and along vertical direction on top. The gradually increase imaginary part in perfect match layer enabling absorb electromagnetic field completely without severe reflection. Running eigen frequency solver for above men-

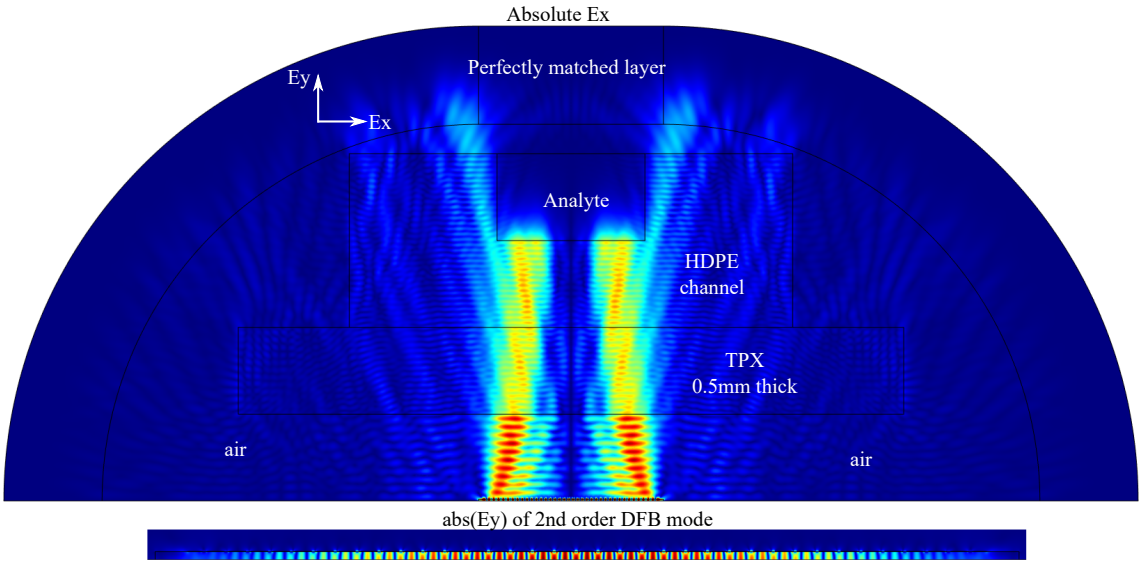

Figure 4.5: Absolute Ex field for 2^{nd} order DFB mode. Bottom insert plot $|E_y|$ for same mode

tion geometry. Simulation result is reveal in figure 4.5. Plotted $|E_x|$ filed showing two lobe in far field indicating that lower 2^{nd} DFB photonic bandedge mode is excited [79]. Single lobe operation can achieve by adding a π shifter on center of normal 2^{nd} order DFB, however this won't change physics for proposed sensor. Insert on bottom of figure 4.5 illustrate $|E_y|$ of same mode which is fundamental $2^{nd} order DFB mode$. By varying permittivity of analyte and solving eigen frequency for the same mode, we can investigate relation between analyte's permittivity and DFB QCL's resonant frequency for a specific geometry.

To numerically investigate how the analyte's permittivity modify antenna DFB resonant frequency, similar eigen frequency simulation had been done. Unlike 2^{nd}

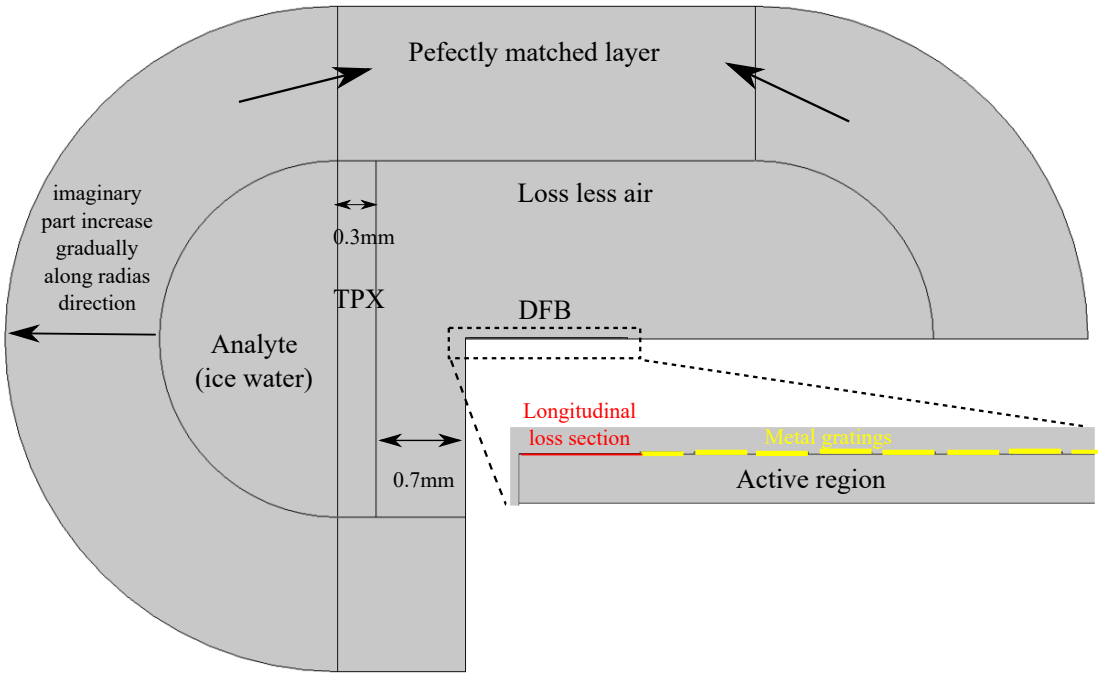

Figure 4.6: Geometry used for antenna DFB eigen frequency simulation.

order DFB which is surface emitting, electromagnetic field emit from every aperture of antenna DFB constructive combined in longitudinal direction. Thus both TPX window and analyte should put on horizontal direction as shown in 4.6. Same type perfect matching layer is defined in simulation to avoid reflection from outer boundary. Not only that some simplification had been made for antenna DFB simulation because the use of HDPE channel significantly increase geometry while the memory need to finish simulation grow dramatically with geometry dimension. To balance simulation speed and accuracy, HDPE channel is abandon in antenna DFB eigen frequency without change sensing physics.

The $|E_y|$ of antenna DFB mode is plotted in figure 4.7. Field intensity in perfect match layer showing that this layer efficiently absorb incident electromagnetic wave before they reach PEC outer boundary. There is a interesting difference between E_y field on TPX side and air side. On TPX side E_y field behaving like a standing wave due to left propagate EM wave interference with reflected EM wave from TPX/air

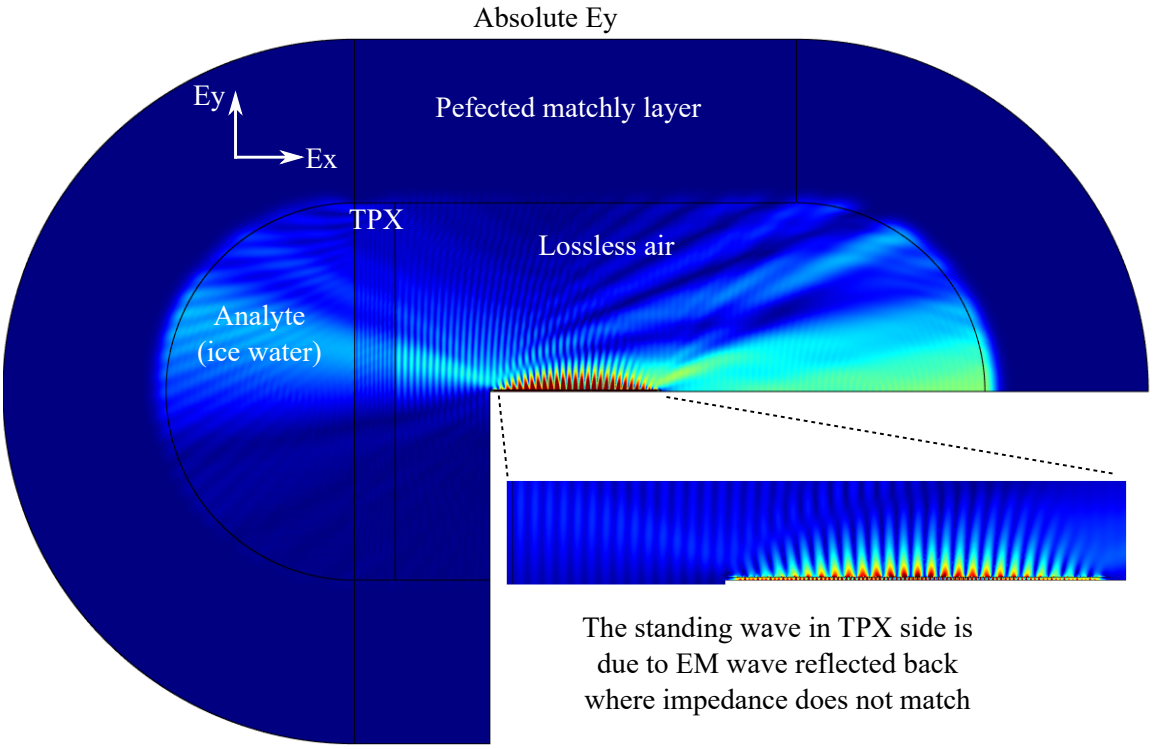

Figure 4.7: $|E_y|$ field for antenna DFB mode. Bottom insert plot $|E_y|$ for same mode close to antenna DFB facet

interface and TPX/analyte interface due to impedance mismatch.

4.4 Results and Discussion

The frequency shift of the sensing QCL due to the presence of analyte contains information about the THz response of the analyte due to its complex refractive index. To measure the frequency shift accurately, without the need of a high-resolution THz spectrometer and a sensitive THz detector, the frequency of the sensing QCL could be downconverted to a microwave beat signal by mixing it with optical field of a reference QCL. The amplitude of the microwave signal does not contain any useful information, and hence this scheme is insensitive to intensity fluctuations in the DFB QCLs. Finite-element simulation of a sensing-DFB QCL in presence of analyte for realistic dimensions corresponding to the sensing architecture in Fig. 4.3 are presented

in Fig. 4.8. When antenna DFB is utilized as sensing QCL, the distance between DFB facet to TPX window of dewar is assumed to be 1mm while TPX window thickness is taken as 300 um. For the case second order DFB acting as sensing QCL, the distance between DFB surface to TPX window of dewar is assumed to be 0.5 mm while TPX window thickness is kept as 300 um. In both cases analyte are assumed to be placed on the surface of TPX window. The QCL cavity is enlarged by a dashed red line at the bottom of the geometry since its height is very small compared to the scale of the simulated geometry. The simulation is illustrated in two-dimensions which should be a good approximation for the fundamental lateral mode propagation that is preferentially excited [79]. The sensing scheme presented here is applicable to analytes with volume as small as 1 mm^3. Also, it is suitable for solids and liquids alike, even though liquids absorb THz radiation strongly. For example, water has THz attenuation in the range of ~ 200 cm^{-1} at room-temperature [60], which would make absorption spectroscopy through liquid samples prohibitively challenging. However, the proposed sensing scheme does not require light to propagate through a lossy analyte; instead reflection happens at analyte/TPX interface which attributes to the shift in resonant-frequency of the sensing QCL. This fact makes this sensing scheme highly sensitive even for very loss materials at THz regime. For the same reason, the scheme could be utilized for standoff sensing and spectroscopic detection as well, especially when antenna-DFB is the sensing QCL because of its very narrow beam pattern [138], which will lead to little loss in intensity even for meter-scale distances from the cryocooler.

4.4.1 Sensor's performance and detection sensitivity

The shift in resonant-frequency under external optical feedback of Fabry-Pérot cavity is modeled by Land-kobayashi theory [62]. The resonant-frequency shift is a function of both the amplitude and the phase of the reflected wave. Complex nonlinear

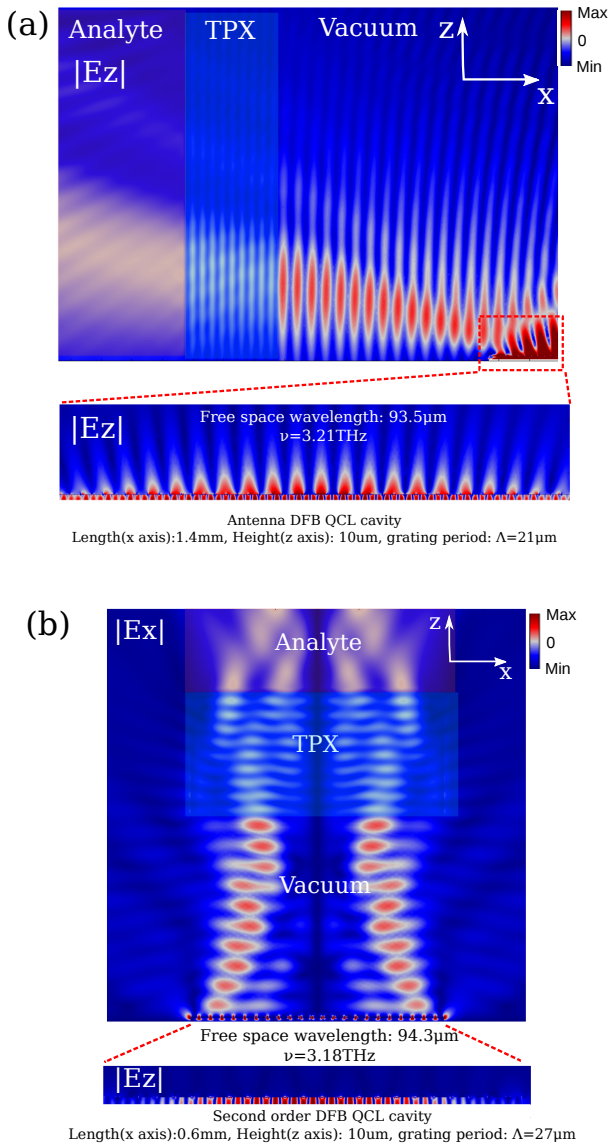

Figure 4.8: Finite-element simulations of the sensing scheme. Electric field intensity for the resonant-cavity DFB mode (which is also the lowest loss mode, and hence the lasing mode) is plotted. The electric-field reduces by an order of magnitude at the interface of the TPX/analyte boundary from its value inside the laser's cavity, and thereafter it decays rapidly (within a distance of few hundred microns) in the analyte. The dewar's TPX window is assumed to be 0.3 mm thick with a refractive index of 1.46. (a) Antenna-DFB cavity (1.4 mm long) with grating period, $\Lambda = 21$ μm (emitting at 3.21 THz) is used as a sensing QCL. The grating period is chosen arbitrarily to show a typical simulation result. Analyte is placed 1 mm away from the facet of antenna-DFB QCL in the longitudinal direction. (b) Second-order surface-emitting DFB cavity (0.6 mm long) with grating period, $\Lambda = 27$ μm (emitting at 3.18 THz) is used as a sensing QCL. Emitted far-field beam pattern of second-order DFB has two lobes for the structure used in this simulation. Single lobed far-field pattern can be achieved by introducing a 180° phase-shifter at the center of the cavity [79]. Analyte is placed at a vertical distance of 0.8 mm from the surface of the second-order DFB QCL.

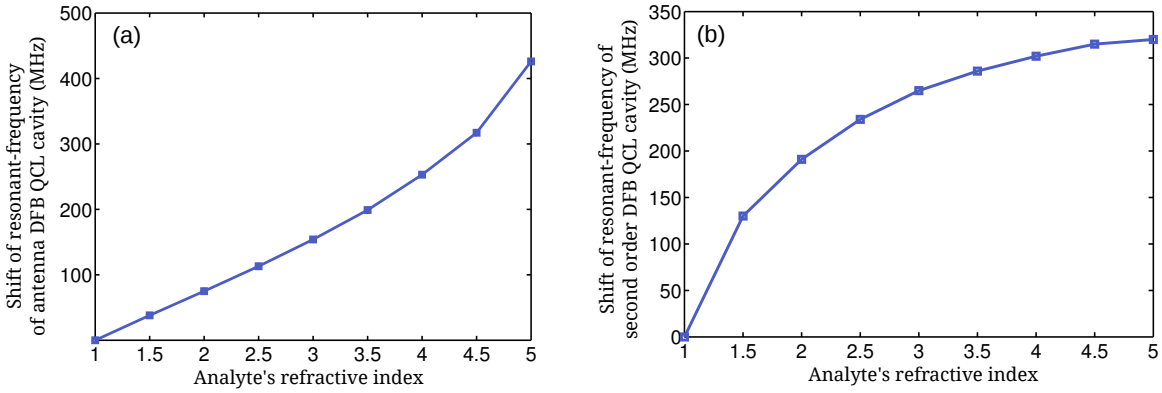

Figure 4.9: Fabry-PérotQCL cavity under external optical feedback. Symbol R_1 represents the internal reflectivity at the end-facets and Φ_1 indicates the change in phase for reflected wave. In presence of an external reflector (analyte) placed outside one of the end-facets, its effect on the cavity can be modeled with a superposition of an additional reflected-wave with reflective R_2 and phase Φ_2 at corresponding facet (in the week feedback regime). The feedback-oscillation condition for the cavity is now modified by both R_2 and phase Φ_2, and hence, the resonant-frequency of the cavity is dependent on the phase and amplitude of the field coupled back into the cavity due to the external feedback mechanism.

dynamics of laser system under optical feedback of of a Fabry-Pérot cavity could be calculated analytically. While for DFB QCLs optical feedback is not only happened at end-facets but also from every aperture. Especially for second order DFB, since second order DFB emitting THz wave from surface and analyte is supposed to put on top of DFB cavity, thus reflected THz wave is coupled back into metallic cavity mainly from each aperture instead of end-facets. This inherent difference make quantitative modeling DFB laser dynamics based on by Land-kobayashi theory beyond scope of this paper. However Land-kobayashi theory provides useful qualitative insight about optical feedback regime. The optical feedback level is measured by so-called feedback parameter C [62]. It can be calculated as

$$C = \frac{\kappa \cdot L \cdot \sqrt{1+\alpha^2}}{l \cdot n} \tag{4.1}$$

where α is the QCL linewidth enhancement factor, L is the distance between QCL facet to analyte, l is the QCL cavity length, n is the resonant mode refractive index and factor κ is given by:

$$\kappa = \frac{\varepsilon}{\sqrt{A}} \frac{1 - R_1}{\sqrt{R_1}} = \varepsilon \sqrt{R_{ext}} \frac{1 - R_1}{\sqrt{R_1}} \tag{4.2}$$

where A is the power attenuation in the external cavity, R_{ext} is the power reflectivity of the analyte which is determined by its dielectric constant, and R_1 is the reflectivity of the cavity's out coupling facet illustrated in Fig 4.9. The coefficient $\varepsilon \ll 1$ is introduced to account for possible mode overlap mismatch between back-reflected light and lasing mode. THz QCL linewidth enhancement factor is experimentally measured [8, 52], and it is found to be less than 0.5. For our calculation we assume it as 0.5. Output facet reflectivity R_1 is taken as 0.8 [73, 71] due to subwavelength confinement of metal-metal cavity. In antenna-DFB case, laser cavity is 1.4 mm long while distance between analyte and output facet is 1.3 mm mm. In second order DFB case, laser cavity is only 0.6 mm long and the distance between laser surface to analyte is 0.8 mm. Thus feedback parameter C is 0.02 and 0.03 for antenna-DFB and second-order DFB respectively, when mismatch coefficient ε is assumed to be 0.5. In reality, ε will be much smaller since there is a large modal mismatch between guided and propagating waves for THz QCLs with metal-metal cavities, which is also the reason for high end-facet reflectivities. Even under variation of reflected optical geometry in the QCL laser array, that is to say distance between laser facet to analyte depends on particular position of a QCL cavity in the array, feedback parameter remains significantly less than 0.1 for all scenarios. This fact indicates that proposed sensing scheme will operate in a very weak feedback regime for all cases.

Since it is difficult to obtain analytical estimation, or intuitive interpretation of the resonant-frequency shift for DFB cavity,finite-element simulations are needed to cal-

culate the expected shift in the resonant-frequency of the sensing QCL as a function of the analyte's refractive-index. Owing to the weak feedback regime, the resonant-frequency of the DFB QCL cavity is primarily shifted due to changes in feedback oscillation condition, rather than carrier dynamics and related change in the refractive index of the DFB cavity due to the active gain medium. Hence, finite-element simulation should capture such a shift in the resonant-frequency very accurately.

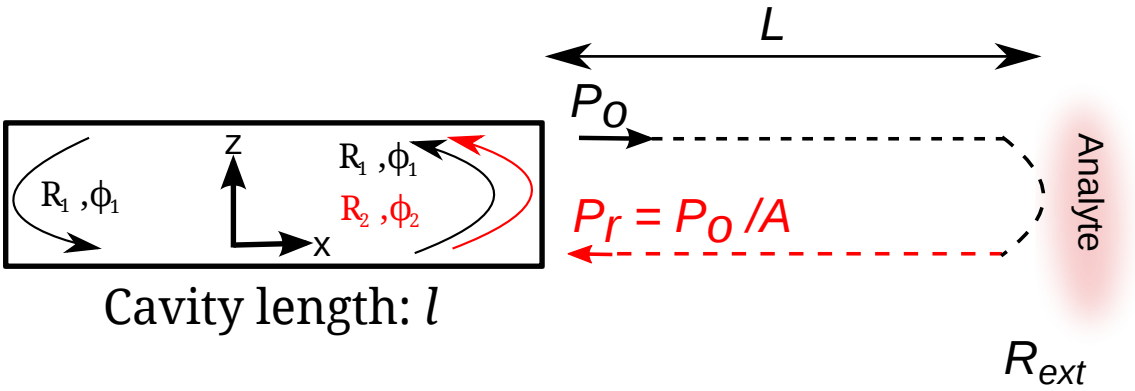

Figure 4.10: Sensor output as a function of analyte's refractive-index.he THz sensor relays a microwave beat signal at its output port, the frequency of which determines the effect of the analyte on the sensing DFB QCLs and is a measure of the complex refractive index of the analyte at the lasing frequency of the QCL. The figure shows the computed shift in the resonant-frequency of a sensing QCL operating at $\sim$ 3 THz as a function of the refractive index of the analyte. The imaginary part of the index is kept 0. However, similar result would be obtained if the imaginary part of the index was changed instead. In general, the shift in the resonant-frequency is a function of the complex refractive index. (a) Simulation geometry is exactly same as it in Fig. 4.8(a) in which the antenna-DFB is the sensing cavity. Real part of analyte's refractive index is changed from 1 to 5 while the imaginary part is kept as 0. When the refractive index is 5, the resonant-frequency of the antenna-DFB mode is shifted by $\sim$ 410 MHz compared to the case when the analyte's refractive index is unity. (b) Second-order DFB is used as sensing cavity and simulation geometry is exactly same as that in Fig. 4.8(b). When the analyte's refractive index is 5 the resonant-frequency of the antenna-DFB mode is shifted by $\sim$ 330 MHz compared to the case when the analyte's refractive index is unity.

A systematic study of resonant-frequency shift corresponding to analyte's refractive-index (when assumed to be real) is performed for both second-order and antenna-DFB sensing schemes. The sensing QCL cavity is designed to excite a resonant-cavity mode

at $\sim$ 3 THz (chosen arbitrarily). When the analyte's refractive index is increased from 1 to 5, resonant-frequency of the antenna-DFB sensing cavity is shifted by $\sim$ 440 MHz while resonant-frequency of a second-order DFB sensing cavity is shifted by $\sim$ 320 MHz. The computed plots are shown in Fig. 4.10. To explain sensitivity of the sensing scheme, a slope $\delta f/(\delta n_{\mathrm{r}}/n_{\mathrm{r}}) \equiv \delta f/\mathrm{RIU}$ can be defined where δf is the shift in resonant-frequency, and $\delta n_{\mathrm{r}}/n_{\mathrm{r}}$ is often-termed as the refractive-index unit (RIU), or the fractional change in the refractive index. For the second-order DFB as sensing QCL, $\delta f/\mathrm{RIU}$ ranges from $100-250$ MHz, whereas for the antenna-DFB as sensing QCL, $\delta f/\mathrm{RIU}$ ranges from $150-500$ MHz approximately depending on operating frequency of the sensing QCL.

The ultimate sensitivity of the proposed scheme will be determined by the linewidth of the THz QCLs being used for sensing. Linewidth of free-running QCLs is typically in the range of $1-10$ MHz [14, 12] when electrical or thermal instabilities are not corrected; however, when the frequency is stabilized (which could be done by locking the frequency of the QCL to a microwave reference oscillator [31]), a long-term linewidth of the order of 10 kHz could be achieved. It may be noted that both the reference and sensing QCLs could potentially be biased using the same voltage-supply (because they are from the same active region, and will have similar threshold characteristics), and hence, most likely the linewidth of the microwave beat signal will be significantly smaller than free-running linewidth of individual QCLs because of cross-correlation in frequency jitter of each of the QCLs. For very high-resolution measurements, the THz QCLs could be phased-locked (as opposed to frequency locked) to a microwave reference oscillator, in which case output THz linewidth of the QCL mimics the linewidth of the microwave reference and a linewidth of the order of $\sim$ 10 Hz could be achieved [56]. The simulation results from Fig. 4.10 suggest that that ppm (part-per-million) RIU level sensitivity might be obtainable if the linewidth of the beat signal is in the kHz range. For frequency and phase-locked QCLs, even better

sensitivities could perhaps be realized.

Laser-based refractive-index sensors that do obtain very high sensitivities and can detect better than ppm RIU (fractional change in refractive index) are typically based on optical-resonance effect of coupled-cavities, and hence are "narrowband" sensors that often target a specific resonance feature of the analyte at a single frequency [105]. In contrast, the proposed sensor can obtain the simulated performance over a broad range of frequencies, only limited by the availability of QCLs at the desired frequency. For specific frequencies, phase-locked QCLs could significantly better the sensitivity by additional three orders of magnitude; however, that will most likely be practically feasible for a few frequencies only rather than a broad range of frequencies due to more complicated set-up for phase-locking. It is also important to know that frequency and phase-locking of QCLs can be done with an all-microwave setup that requires commonly available microwave components, and hence still keeps the cost of the proposed THz sensor instrument low.

To illustrate an example of sensing the imaginary part of refractive index of an analyte, the frequency-shift for sensing QCLs is estimated for ice-water as analyte, and is plotted for ice-water at different temperatures in Fig. 4.11. According to Ref. [60], permittivity of ice at 2.5THz is $3.15-0.4906i,\ 3.15-0.4544i,\ 3.15-0.4187i$ respectively for $-15°C,\ -30°C,\ -60°C$. Fig. 4.11 shows the resonant-frequency shift for antenna-DFB and second-order DFB sensing QCLs for these three cases. The minimum resolution for the computed resonant-frequency of the QCL by the finite-element solver was $\sim$ 1 MHz, hence no data is computed at smaller ranges. However, as long as the intrinsic linewidth of the beat-signal is smaller than 1 MHz this sensing scheme could detect much smaller changes in complex refractive-index of the analyte.

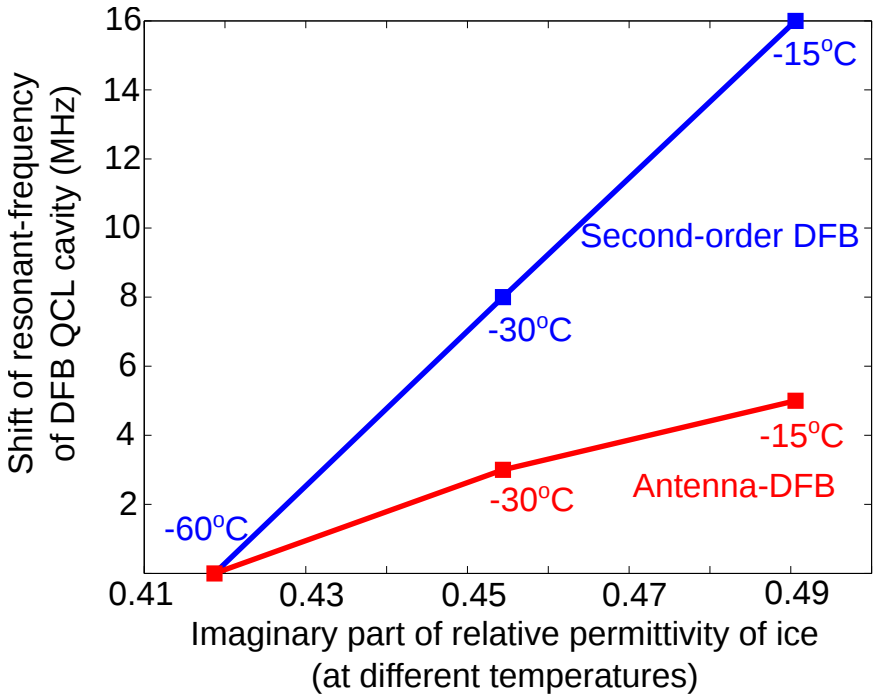

Figure 4.11: Computed sensor output for ice-water at different temperatures at 2.5 THz. As an illustration of the sensing scheme, the geometry described in Fig. 4.8 is used for obtaining the output of the sensing scheme. For the simulations, the grating period of the sensing QCL cavity is chosen to excite a resonant-cavity mode at 2.5 THz. As shown in Ref. [60], imaginary part of complex permittivity for ice-water varies from 0.4187 to 0.4906 for the shown range of temperatures, the real part remains as 3.15 at all temperatures. When second-order DFB is used as sensing cavity, its resonant frequency is shifted by 16 MHz when ice-water's temperature decreases from $-15°C$ to $-60°C$. The shift of resonant-frequency for an antenna-DFB sensing QCL for the same parameters is smaller, and is computed to be 5 MHz.

4.5 Conclusions

In conclusion, here we propose and investigate a novel THz QCL-based spectroscopic sensing scheme, that can probe the complex refractive index of an analyte at a broad range of THz frequencies. The analyte could be in condensed or liquid-phase, may have large THz absorption, and be located in ambient conditions. The analyte does not require any preparation for sensing, even ultra-small volumes of the analyte could be sensed effectively.The broadband THz sensor consisting of arrays of single-mode QCLs cooled inside a portable Stirling cryocooler could be realized, in which the

output signals are microwave frequencies corresponding to each QCL, that are proportional to the shift in the resonant-frequency of the respective single-mode QCLs in presence of the analyte. The proposed scheme could therefore be used for spectroscopic identification and detection of chemical and biological samples, with the potential of standoff sensing and detection as well. No THz detectors or movable parts are required, because the active region of the QCL acts by itself as a non-linear detection medium. The sensing scheme is inherently immune to intensity fluctuations of laser's output or other interference effects because it relies on measurement of the shift in the resonant-frequency of the QCLs. Better than ppm RIU (refractive-index unit) sensitivities could be attained across the broad-frequency range. The sensing scheme is general and versatile, and could potentially be applied to semiconductor lasers operating at shorter wavelengths as well.

Chapter 5

Resonant-Phonon THz Quantum Cascade Detectors

For THz researches sensitive THz detectors are equal important, if not more, as THz source. A variety of THz detectors are available with wide-ranging characteristics [112] These THz detector include bolometer [111], Golay cells, and pyroelectric detectors [1]. For bolometer, two types bolometer are used in THz research, first one is liquid-Helium cooled solid-state bolometers [4, 5] that are among the most sensitive THz detector,the other type is consider less-sensitive room-temperature microbolometers [19]. Resonant frequencies of the two-dimensional plasma in FETs increase with the reduction of the channel dimensions and can reach the THz range for sub-micron gate lengths. Nonlinear properties of the electron plasma in the transistor channel can be used for the detection and mixing of THz frequencies. [70, 37] Not only in field transistors, two dimensional electronic fluid at Schottky-diode interface can also used for detection, mixing and multiplication in THz regime.[37, 119] Room-temperature THz detectors based on field-effect transistors and Schottky-diodes have recently become attractive as they have been demonstrated to detect frequencies above 2 THz (their sensitivity diminishes rapidly at higher THz frequencies). These detectors are

broadband detectors thus that are used in conjunction with passive filters for THz regime detection. Since there is no semiconductor has such a narrow bandgap suitable for THz detection, first semiconductor based THz detector utilize impurity whose energy very close to either conduction band or valence band edge. First impurity Far-IR/THz detector was demonstrated in 1965 which was a Gallium doped Germanium detector for $40 - 120$ μm. [101] This type of detector only work at liquid helium temperature due to very low dopant activation energy, however they have very high sensitivity. [45] Narrow band detectors based on low-dimensional semiconductors have also been developed, which do not require spectral filtering, but at the same time, need to be designed according to the desired detection frequency. Among these, the primary types of detectors are the quantum-well photodetectors (QWPs) [53] and the quantum-dot photodetectors (QDPs) [121].

5.1 Quantum-Well and Quantum-Cascade photodetectors

Detection by intersubband transitions were extensively investigated by Levine *et al.* at AT&T Bell lab as well as Harwit and Harris at Stanford University. They did a systematic study on absorption and Stark shift of intersubband transition in GaAs/AlAs superlattice [88, 55] These result lead to invention of first quantum well infrared photodetector (QWIP) by Levine *et al.* in 1987 [87], 7 years earlier than first demonstration of intersubband laser at 1994 [39]. Since then many other researcher made important contribution in develop high performance QWIPs, important work including hole based QWIPs comparable detect normal incident Infrared light [85], and low dark current QWIPs [84]. Progress and summary of QWIPs can be found in Levine's excellent review paper [86] and H.C.Liu's comprehensive book chapter [92].

Working principle is illustrated in Fig5.1.

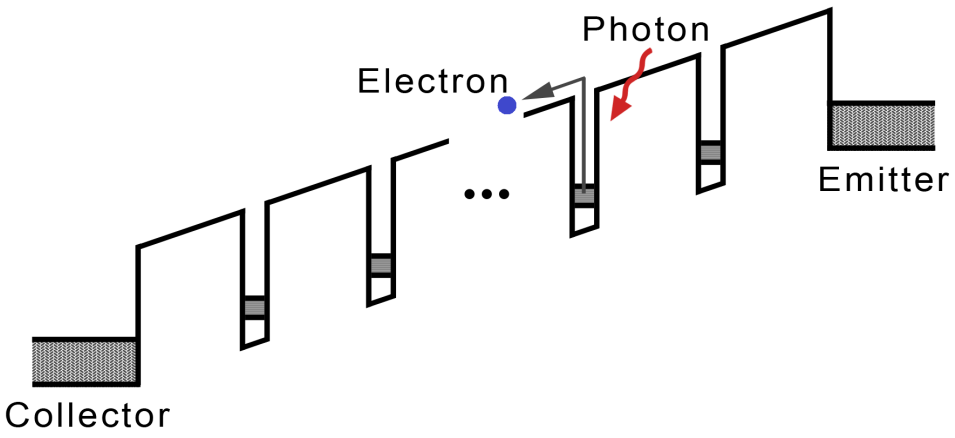

Figure 5.1: Schematic of QWIP working principle (Figure download from Wikipedia website [3]) Originally electrons are confined within quantum well, after absorbing an incident photon electrons escape from bound state to continuum and contribute to current.

The basic elements of a QWIP are single quantum wells, which are separated by thick barriers. The quantum wells' thickness is carefully designed to have one confined state inside the well and a first excited state which aligns with the top of the barrier. The barriers are chosen to be very wide to minimize quantum tunneling between the quantum wells. Typical QWIPs consists of 20 to 50 quantum wells. When a bias voltage is applied across the QWIP, the entire conduction band is tilted. Without light the electrons confined within quantum wells in the ground state. When the QWIP is illuminated with light of the similar or higher energy as the intersubband transition energy, an electron is excited. Once the electron is in an excited state, it can escape into the continuum efficiently and be measured as photocurrent.

The idea of quantum cascade detector (QCD) was initiated from measurements of photocurrents in QCLs by Hofstetter *et al.* [58]. Hofstetter's experiment utilized a mid-infrared QCL; however later others also recognized the same approach was also promising for THz detection [51]. Unlike QWIPs for which applied bias is essential, QCDs operate in photovoltaic mode. At THz regime, photon energy is very low (3 THz = 100 μm = 12.3 meV corresponding to a temperature of $\sim$ 140 K). In

conventional QWIP, the shallow barrier height will lead to a lot of thermally activated electrons in continuum higher in conduction band, burying the photocurrent in thermal noise. A good way to solve this problem is "tailoring" the transport path of electrons i.e make electron tunneling through high barriers. This concept lead to first experimental demonstration of of a THz QCD at Faist's group [50]. The maximum operating temperature of THz QCDs demonstrated so-far is 50 K when a THz QCL emitting at 87 μm for 350 μW power was used as light source[51]. This temperature is significantly higher than those conventional THz QWIPs which need to cooled down below 10 K. [53, 93].

5.2 Theoretical Framework for QCD Design

Although both quantum cascade laser and quantum cascade detector utilize intersubband transitions, there are significant different focus when design them. This section describe general physics of intersubband transition and noise mechanism in photodetectors. This work focus on electron intersubband transition based design with n doped GaAs/$Al_xGa_{1-x}As$ material system. Modeling of electron behavior in photodetector based on single-particle in one single band of the electronic structure of bulk semiconductor. Thus all theoretical framework will be done with effective mass approximation. The description below roughly follow the book by Helm [57] and the book written by Weber *et al.* [130].

5.2.1 Absorption Coefficient in Quantum-Wells

According to Bloch description of the electronic structure of bulk semiconductor crystal the single electron conduction band wavefunction $\psi_i(r)$ is considered as product of a fast varying function $u_\nu(r)$ with lattice periodicity and a slowing varying envelop

function $f_i(r)$

$$\psi_i(r) = f_i(r)u_\nu(r) \tag{5.1}$$

for bulk semiconductor $f_i(r)$ is just simple plane wave:

$$f_i(r) = e^{ik_i \cdot r} \tag{5.2}$$

In the quantum well case, an external potential due to material composition or/and electric field is presence, the envelop function $f_i(r)$ is solved from Schrodinger equation

$$\frac{-\hbar^2}{2m^*} \bigtriangledown^2 f_i(r) + V(r)f_i(r) = E_i f_i(r) \tag{5.3}$$

For the case of semiconductor superlattice, material composition modulation only exist in growth direction thus we can separate variable for $f_i(r)$.

$$f_{i,k_{||}}(r) = \frac{1}{\sqrt{A}} e^{ik_{||} \cdot \rho} \varphi_i(z) \tag{5.4}$$

where $1/\sqrt{A}$ is normalization factor for wavefunction and A is area of the device. Now 5.3 can separate variables:

$$\frac{-\hbar^2}{2m^*} \frac{d^2}{dz^2} \varphi_n(z) + V(z)\varphi_n(z) = E\varphi_n(z) \tag{5.5}$$

total energy eigenvalues are given by

$$E_{n,k_{||}} = E_n + \frac{\hbar^2 k_{||}^2}{2m^*} \tag{5.6}$$

E_n is depend on external potential $V(z)$ and solved from 5.5 Electron-photon interaction Hamiltonian is defined as

$$H_{e-photon} = \frac{e}{2m^*}(A \cdot p + p \cdot A) \tag{5.7}$$

where e is elementary charge, m^* is electron effective mass, A is electromagnetic scalar potential and p is momentum operator. Rate for an electron absorb an incident THz photon and transition form initial state to final state calculated by Fermi's golden rule

$$W_{i\to f} = \frac{2\pi}{\hbar}|\langle\psi_i|H'|\psi_f\rangle|^2\delta(E_f - E_i - \hbar\omega) \tag{5.8}$$

Since light source is enough far away, the incident electromagnetic wave can correctly describe by plane wave, thus electric field as function of position and time is

$$E(r,t) = E_0 e cos(q \cdot r - \omega t) = \frac{E_0 e}{2}(e^{i(q\cdot r-\omega t)} + e^{-i(q\cdot r-\omega t)}) \tag{5.9}$$

where q is propagation vector and e is polarization vector perpendicular to q. We choose a gauge which electric filed is produced by $E = \frac{-\partial A}{\partial t}$, thus now electrical potential A expressed as

$$A(r,t) = \frac{E_0 e}{\omega} sin(q \cdot r - \omega t) = \frac{iE_0 e}{2\omega} e^{i(q\cdot r-\omega t)} + c.c \tag{5.10}$$

Since wavelength is of the order of 100μm while one module length of a quantum cascade structure is of the order of tens nanometer, we can apply dipole approximation. Under dipole approximation, A and p commute, now interaction Hamiltonian becomes

$$H_{e-photon} = \frac{e}{m^*} A \cdot p \tag{5.11}$$

Inserting 5.11 back to 5.8, we obtain

$$W_{i\to f} = \frac{2\pi}{\hbar}\frac{e^2E_0^2}{4m^{*2}\omega^2}|\langle\psi_i|\mathbf{e}\cdot\mathbf{p}|\psi_\mathbf{f}\rangle|^\mathbf{2}\delta(\mathbf{E_f}-\mathbf{E_i}-\hbar\omega) \tag{5.12}$$

$\mathbf{e}$ inside the matrix element $\langle\psi_i|\mathbf{e}\cdot\mathbf{p}|\psi_\mathbf{f}\rangle$ is polarization vector while e on numerator is elementary charge. Applying 5.4 into matrix element $\langle\psi_i|\mathbf{e}\cdot\mathbf{p}|\psi_\mathbf{f}\rangle$

$$\langle\psi_i|\mathbf{e}\cdot\mathbf{p}|\psi_\mathbf{f}\rangle = \mathbf{e}\cdot\langle\mathbf{u}_\nu|\mathbf{p}|\mathbf{u}_{\nu'}\rangle\langle\mathbf{f_n}|\mathbf{f_{n'}}\rangle + \mathbf{e}\cdot\langle\mathbf{u}_\nu|\mathbf{u}_{\nu'}\rangle\langle\mathbf{f_n}|\mathbf{p}|\mathbf{f_{n'}}\rangle \tag{5.13}$$

now optical matrix element split into two types. [40] The first term describe interband transitions and second part is intersubband transitions. This fact can be seen as following, momentum operator p change parity of $u_{\nu'}$, if band indices ν, ν' of initial and final band are identical $\langle u_\nu|p|u_{\nu'}\rangle$ gives zero. Thus first term is non-zero only when band indices ν, ν' of initial and final band are different. Second term in 5.13 is non-zero only if initial and final states are in same band, $\nu=\nu'$ yield $\langle u_\nu|u_{\nu'}\rangle = 1$. The remaining part of intersubband electron-photon interaction now is $\langle\psi_i|\mathbf{e}\cdot\mathbf{p}|\psi_\mathbf{f}\rangle = \mathbf{e}\cdot\langle\mathbf{f_n}|\mathbf{p}|\mathbf{f_{n'}}\rangle$, f_n and $f_{n'}$ are envelop of initial and final subbands. Writing envelop function f_n in explicit form and evaluates matrix element,

$$\langle f_{n,k_{||}}|e\cdot p|f_{n',k'_{||}}\rangle = e_z\delta_{k'_{||},k_{||}}\int dz\varphi_n^*(z)p_z\varphi_{n'}(z) \tag{5.14}$$

This result is the well known intersubband selection rule. Intersubband transition only allowed optical transition if the electric field has polarization parallel to semiconductor superlattice growth direction. To simplify the formula we introduce notation $\langle n|p_z|n'\rangle = \int dz\varphi_n^*(z)p_z\varphi_{n'}(z)$. Now introduce dimensionless oscillation strength $f_{nn'}$ and applying well known commutation relation between momentum operator $\widehat{p}$ and

position operator $\widehat{z}$

$$f_{nn'} = \frac{2}{m^* \hbar \omega_{n'n}} |\langle n|p_z|n'\rangle|^2 = \frac{2m^* \omega_{n'n}}{\hbar} |\langle n|z|n'\rangle|^2 \tag{5.15}$$

summing over all final states n', oscillation strength obeying sum rule

$$\sum_{n'} f_{nn'} = 1 \tag{5.16}$$

Simple matrix electron-photon interaction 5.14 make calculate absorption coefficient possible. Absorption coefficient α is defined as ratio between electromagnetic energy being absorbed per volume per unit time and the intensity of incident light I. It is more convenient to define two dimensional absorption coefficient α_{2D} by defining ratio between absorbed energy per area (A) per unit time and the incident light intensity I. Now 2D absorption coefficient α_{2D} is dimensionless while 3D absorption coefficient α_{3D} has the unit inverse length (m^{-1}).

Summing over all possible initial and final states n and n', 2D absorption coefficient is then written as

$$\alpha_{2D} = \frac{\hbar\omega}{IA} \sum_{nn'} \sum_{k_{||}} \frac{2\pi}{\hbar} |\langle n|\frac{e}{m^*} A \cdot p|n'\rangle|^2 f(E_n(k_{||}))(1 - f(E_{n'}(k_{||})))\delta(E_{n'}(k_{||}) - E_n(k_{||}) - \hbar\omega) \tag{5.17}$$

where $f(E_n)$ is Fermi-Dirac distribution measuring possibility of a states occupied by an electron at particular electron temperature T_e. Inserting 5.10,5.13,5.14,5.15 as well as the relation $I = \varepsilon_0 c n \frac{E_0^2}{2}$ into 5.17 and replace the summation over all in-plane momentum by a 2D integral leads to

$$\alpha_{2D} = \frac{\pi e^2}{\varepsilon_0 c n \omega m^{*2}} \sum_{n,n'} \frac{2}{(2\pi)^2} \int d^2 k_{||} |\langle n|p_z|n'\rangle|^2 f(E_n)(1 - f(E_{n'}))\delta(E_{n'} - E_n - \hbar\omega) \tag{5.18}$$

Applying parabolic in plane dispersion the integral over all in plane momentum can be calculated as analytically expression. Also δ function is replaced by a Lorentzian with Full-width-half-maximum (FWHM) of 2Γ. Electron-photon interaction matrix element is expressed by oscillation strength defined in 5.16. Now 2D absorption coefficient is [51]

$$\alpha_{2D} = \frac{e^2 K_B T_e}{2\varepsilon_0 c n \hbar} \sum_{n,n'} f_{n,n'} \ln \left(\frac{1 + e^{\frac{E_F - E_n}{K_B T_e}}}{1 + e^{\frac{E_F - E_{n'}}{K_B T_e}}} \right) \frac{\Gamma/\pi}{(E_{n'} - E_n - \hbar\omega)^2 + \Gamma^2} \tag{5.19}$$

5.2.2 Figures of Merit for Photodetectors

In this subsection, some important figure of merits for photodetectors are introduced. The description of this section are roughly follow the book by Schneider and Liu [116], review paper by Rogalski [112], and dissertation by Graf [51]

Photodetectors transform incident light into electric signals, which are suitable for further signal processing. Photodetectors roughly divided into two categories namely thermal detector and photon detector. This section focus on second category. Photon detector convert photons in to electrons and "measure" generated electrons between two metal contact of the device. The number of generated electrons per number of photons reaching the detector surface per unit time determines detector efficiency. This quantity is overall quantum efficiency:

$$\eta_{tot} = \frac{N_e}{N_p} \tag{5.20}$$

It is more convenient to use macroscopic quantities like radiation power and current instead of counting number of particles. Spectral responsivity $\mathcal{R}$ which is the ratio between electrical current and illumination power are widely used. Current flow through the device can be expressed as $I = \frac{eN_e}{\tau}$ where e is elementary charge, N_e is number of electrons generated during time period τ. Illumination power in terms

number of photons is $P_i = \frac{h\nu N_p}{\tau} = \frac{hc}{\lambda\tau}N_p$, h and Planck's constant and $h\nu = \frac{hc}{\lambda}$ is photon energy. Thus spectral responsivity is now defined as

$$\mathcal{R} = \frac{I}{P_i} = \frac{\lambda e}{hc}\frac{N_e}{N_p} = \frac{\lambda e}{hc}\eta_{tot} \tag{5.21}$$

Unlike total quantum efficiency η_{tot} which is overall effect of incident photon in all wavelength, spectral responsivity change proportional to wavelength for a constant η_{tot}. The total quantum efficiency η_{tot} can be described as a product of several specific quantum efficiency and probability regarding the working principle of the photon detector.

$$\eta_{tot} = \eta_{abs} p_e \tag{5.22}$$

η_{abs} is absorption efficiency which is the ratio between photon be absorbed by photodetector over total number of photon incident on detector surface. This efficiency can also be expressed by absorption coefficient defined previously 5.19 as $\eta_{abs} = 1 - e^{N\alpha_{2D}}$. Another crucial factor is escape probability p_e, this quantity measures the what is the fraction of electrons contribute to current once excited by absorbed an photon. In the case of quantum cascade structure, a period is repeated multiple times, escape probability p_e should divided by a factor of N where N is the number of period. For QWIPs there is some gain mechanism like photo conductive gain $g = \frac{p_e}{Np_c}$ with capture possibility p_c.

All measurement are inevitable affected by various noise mechanism. A detector will generate electrical signal related to incident light intensity however there will also be signal has no correlation with incident radiation. Commonly used term signal-to-noise-ratio S/N describe relative intensity of these two quantities.

$$S/N = \frac{I_{signal}}{I_{noise}} \tag{5.23}$$

For photodetector, the term "Noise Equivalent Power" NEP is also widely used. NEP is defined as the power of incident radiation needed to generate a signal strength as produced by noise source.

$$NEP = \frac{P}{S/N} \qquad (I_{moise} = \mathcal{R} \cdot NEP) \tag{5.24}$$

NEP depend on surface area of the detector as well as detector's bandwidth. Normalize NEP respect to surface area A and bandwidth Δf, which lead to the definition of detectivity $\mathcal{D}^*$

$$\mathcal{D}^* = \frac{\sqrt{A\Delta f}}{NEP} \tag{5.25}$$

inserting 5.24 back into 5.25 we obtain the relation between detectivity $\mathcal{D}^*$ and responsivity $\mathcal{R}$.

$$\mathcal{D}^* = \frac{\mathcal{R}\sqrt{A\Delta f}}{I_{noises}} \tag{5.26}$$

Value of $\mathcal{D}^*$ normally expressed in units of $cm\sqrt{Hz}/W$, this unit is also called "Jones" in honor to R.Clark Jones [61].

5.2.3 Noise Mechanisms

There are different noise mechanism limit the performance of photodetectors mainly include $1/f$ noise, Johnson noise and shot noise. $1/f$ noise is universal noise source to all physical and electrical processes, since all frequency we are considering here are high enough to suppress $1/f$ noise, therefore it will be neglected in discussion.

Johnson noise also called as thermal noise origin from Brownian motion of charged particle activated by kinetic energy in resistive device. Johnson noise's spectral power density is flat and defined as

$$p_{noise,J} = 4k_B T\Delta f \tag{5.27}$$

where k_B is Boltzmann constant, Δf is the bandwidth of detector. For an ohmic device with resistance R, a well known voltage and current spectral nose density expressed as

$$\begin{aligned} i^2_{noise,J} &= \frac{4k_BT\Delta f}{R} \\ v^2_{noise,J} &= 4k_BTR\Delta f \end{aligned} \tag{5.28}$$

If Johnson noise the dominant noise mechanism, Johnson noise detectivity is defined as [51]

$$\mathcal{D}^*_j(\nu) = \mathcal{R}(\nu)\sqrt{\frac{R_0A}{4k_BT}} \tag{5.29}$$

In device like QWIPs, it operate under cryogenic cooling, thus Johnson noise contribution is negligible compared to dark current noise. In conventional QCDs which are photovoltaic type photodetectors, Johnson noise is important since the absence of dark current at cryogenic temperature.

The mean square noise current generated by dark current I_{dark} can be described as

$$i^2_{noise,dark} = ueg_{noise}I_{dark}\Delta f \tag{5.30}$$

where e is element charge, constant u related to nature of noise mechanism, it equals 2 for generation mechanism and equals 4 origin from generation-recombination noise [13]. Expression for noise gain g_{noise} can be found in different literature. [91, 90, 89, 139] Hence, the dark current limited detectivity $\mathcal{D}^*_{dark}$ is

$$\mathcal{D}^*_{dark}(\nu) = \frac{\mathcal{R}(\nu)}{\sqrt{ueg_{noise}J_{dark}}} \tag{5.31}$$

Current introduced by incident light, ambient light as well as black body radiation of the environment produce noise in the same way as dark current noise. Photo current noise is treated in the same way as dark current, by replacing dark current density

$J_{dark} = I_{dark}/A$ with current density introduced from background illumination J_{BG}.

$$J_{BG} = e\int \eta(\lambda)\frac{d\Phi_{BG}(\lambda)}{d\lambda}d\lambda = e\int \eta(\nu)\frac{d\Phi_{BG}(\nu)}{d\nu}d\nu \tag{5.32}$$

where η is total quantum efficiency is defined as 5.20, and $\frac{d\Phi_{BG}(\nu)}{d\nu}$ is the background photon flux spectral density. For background radiation emitted by the black body radiation at temperature T_{bb} and a full cone of view (FOV) angle Θ, its emission can be expressed as

$$K(\nu, T_{bb})d\nu = \frac{2h\nu^3}{c^2}\frac{d\nu}{e^{\frac{h\nu}{k_B T_{bb}}} - 1} \tag{5.33}$$

Hence now background photon flux spectral density is given by the formula

$$h\nu \cdot \frac{d\Phi_{BG}(\nu)}{d\nu} = \pi \sin^2(\frac{\Theta}{2}) \cdot K(\nu, T_{bb}) \tag{5.34}$$

Inserting 5.33,5.34 back to 5.32 and replace J_{dark} in 5.31 with J_{BG}we obtain background limited detectivity

$$\mathcal{D}^*_{BLIP}(\nu) = \frac{\mathcal{R}(\nu)}{\sqrt{ue^2 g_{noise}\int \eta(\nu')\frac{d\Phi_{BG}(\nu')}{d\nu'}d\nu'}} \tag{5.35}$$

As different noise source are statistically independent, they can add up quadratically [51]

$$i^2_{noise} = \sum_{\zeta} i^2_{noise,\zeta} \tag{5.36}$$

Thus total detectivity under influence of Johnson noise, dark current noise and photo current noise is

$$\mathcal{D}^*_{tot}(\nu) = \frac{\mathcal{R}(\nu)}{\sqrt{\frac{4k_B T}{R_0 A} + ue^2 g_{noise}(J_{dark} + \int \eta(\nu')\frac{d\Phi_{BG}(\nu')}{d\nu'}d\nu')}} \tag{5.37}$$

5.3 Design of THz QCDs based on resonant-phonon depopulation

The two primary characteristics of infrared detectors is the response time that determines their speed, and their sensitivity that determines the smallest optical power that could be detected. The NEP of commercially available room-temperature pyroelectric detectors is typically $\sim$ 1nW/$\sqrt{Hz}$ ($\mathcal{D}^* \sim 10^8 Jones$) and the response time is in the range of tens of μs to ms. [1] Liquid-Helium cooled bolometers can achieve NEP of $\sim$ 1pW/$\sqrt{Hz}$ ($\mathcal{D}^* \sim 10^11 Jones$) , but most bolometers typically have a much slower response (except fast superconductor bolometers whose response time is sub-nanosecond). The work on semiconductor based QWPs and QDPs is primarily attractive because of their inherently fast (sub-ns) response times, and the ease of fabrication in which focal-plane array-type geometries could easily be realized. Whereas THz QWPs show excellent NEPs (similar to that of cooled bolometers), they only work at temperature close to that of liquid-Helium [53]. THz QDPs on the other hand, could work at temperatures above that of liquid-Nitrogen [121], however their NEP is similar to that of the room-temperature pyroelectric detectors.

The idea of photovoltaic mode QWIPs was firstly introduced by Schneider at 1993 [115]. He proposed the use of asymmetrical quantum well structure effectively producing an internal bias field. The proposed device can operate at photovoltaic mode that is to say without external bias. Schneider theoretically showing that such mode leads to optimized operation under high photon fluxes or long integration times in the Mid-IR wavelength range ($8 - 12\mu$m). Later in 1993, Schonbein, Schneider *et al.* reported experimental result of successfully operate photovoltaic QWIPs in GaAs/AlGaAs material system at 77K for 10μm with a peak detectivity of 5.1 $\times$ 10^9Jones [117]. Same group characterized identical device at room temperature in 1996 for very high speed response, measured rise and decay time is 12 ps and 65

ps respectively. This result verify intersubband transition based photodetector have very short response time.

The idea of photovoltaic type quantum well detector was further developed after the invention of quantum cascade laser. At 2004, not far from first THz quantum cascade laser was demonstrated, photovoltaic photodetectors in quantum cascade structure was experimentally demonstrated in both Mid-IR and THz range. [50, 47]

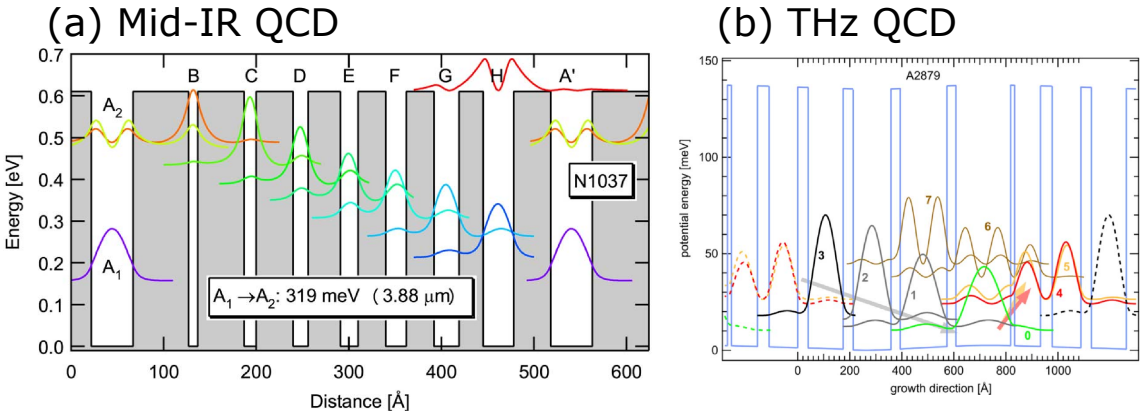

Figure 5.2: (a) Typical band diagram for Mid-IR QCD [49]. QW A is the active QW, which is degenerately doped QWs B-H form the electron extraction cascade and remain undoped. The transport from the A_2 in active QW into the cascade is ensured through resonant tunneling between and the ground state of QW B. This design strategy allows a very thick barrier between the active QW and the extractor. Due to this thick barrier, the interaction between active QW and intermediate extractor levels is reduced, which increases the device resistance without lowering the escape probability. To achieve an efficient electron extraction through phonon assisted scattering, the energy difference between the individual extractor states should be close to the longitudinal optical phonon energy E_{LO} (36meV for GaAs and 32meV for $In_{0.53}Ga_{0.47}As$). (b) Typical band diagram for THz QCD. [49] Unlike degenerate doping for Mid-IR QCD, doping density for THz QCD is very low $\sim 6 \times 10^15/cm^3$. Instead of intra-well transition in active QW for Mid-IR QCD, THz QCD utilize inter-well transition. Main reason for this design strategy is push parasitic subbands away to reduce unexpected electron transport channel. Since THz photon ($\sim$ 15 meV) energy is smaller than Phonon energy (36 meV for GaAs), miniband type transport is used to extract electrons.

Typical band diagrams for Mid-IR and THz quantum cascade detector are showing in 5.2 Mid-IR QCD use resonant phonon design to efficiently extract electrons while THz QCD have to use miniband for electron extraction due to THz photon

energy is much smaller than LO phonon energy in III-V compound semiconductor. Room temperature detection had already experimentally demonstrated for Mid-IR QCD [49], high frequency response up to 30 GHz limited by external electrical circuit also demonstrated for Mid-IR QCD. [51] THz QCD only work up to about 50 K [51],THz QCD with best temperature performance only have a detectivity $\mathcal{D}^*$ in the order of 5×10^7 Jones at 10 K.

5.3.1 Phonon-scattering based relaxation for photoexcited electrons

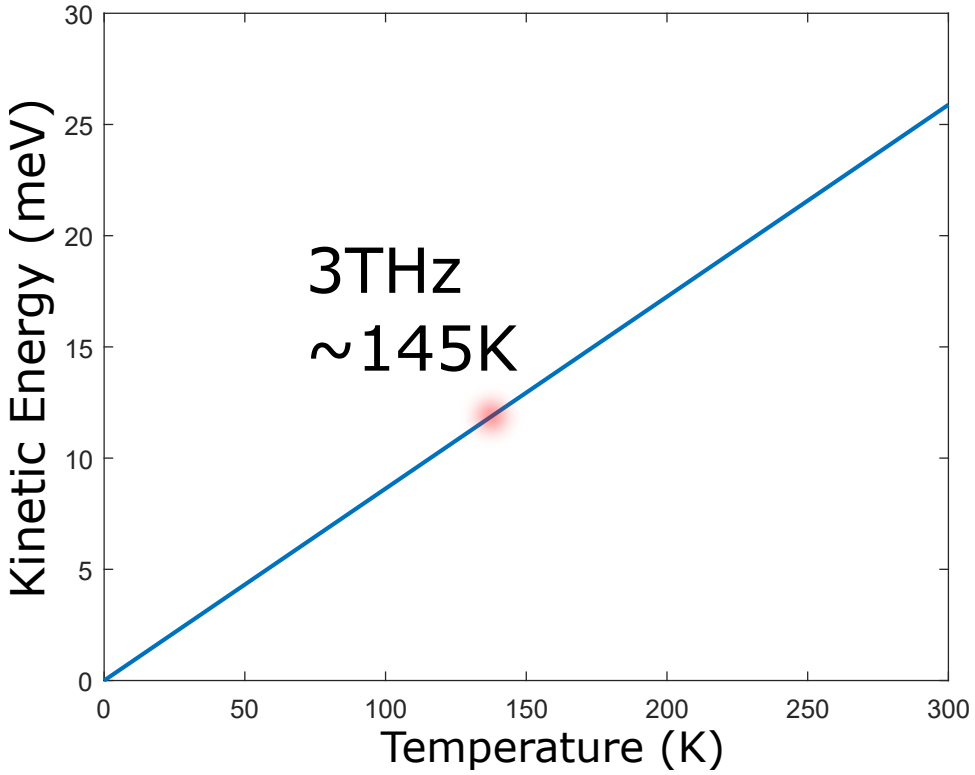

Figure 5.3: Temperature versus Kinetic energy calculated as $E_k = k_B \cdot T$ unit in meV

Showing in previous sections, to our best knowledge, there is a lack of THz semiconductor photodetectors with high sensitivity, quick response time can work at high temperatures. Existing photodetectors need liquid-Helium cooling that results in high

operation costs. However, state of art compact Stirling Cryocoolers can already cool semiconductor devices down to about $\sim$ 45 K. Given above the trade-offs between different types of THz detectors, it is clear that a THz detector that could achieve high temperature operation($\geq$ 45 K), sub-ns response times, and shows sensitivity (NEP) better than pyroelectric detector would be the ideal technology to make a significant impact for THz applications. The difficulty of increasing maximum operation temperature falls into the fact that kinetic energy of electron is k_BT. While the separations between subbands in 5.3 for electron extraction are about $4-5$ meV hence when temperature is more than 50 K, electrons have high enough kinetic energy to backfill higher subbands instead of transport to lower subbands. This simple analysis qualitatively explain the limitation of maximum operation temperature for miniband THz QCD. Experimental result indicate that when device temperature is more than 50 K, Signal current in THz QCD illustrated in 5.3(b) buried in noise current.

For increasing maximum operation temperature of THz QCLs, a critical challenge is to efficiently depopulate electrons from the lower radiation subband. Hence, the depopulation mechanism of elastic scattering within miniband is replaced by fast electron-LO phonon scattering successfully significant increase maximum operation of THz QCL. [68]. Till today, all active region designs for QCLs that could operate at more than 150 K utilize resonant -phonon depopulation. Thus a straight forward solution to increase THz QCD operation temperature might be to use resonant-phonon depopulation as a strategy for relaxation and extraction of photoexcited electrons..

To design resonant phonon (RP) THz QCD, electric field (bias) has to add in order to gap energy difference between E_{LO} and E_{photon} thus electron transport can be accomplished in a cascade scheme. Schematic of resonant phonon THz QCD working principle is illustrated in Figure5.4.

Separation between subband u and l equals to photon energy which the device aim to detect. while l and i' should close to LO phonon energy, thus enable fast electron-

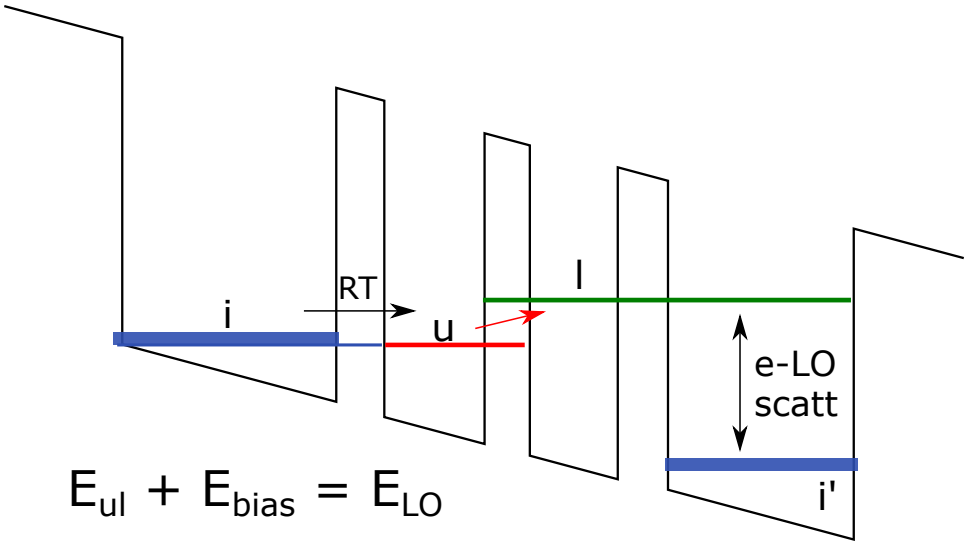

Figure 5.4: Schematic of resonant phonon THz QCD working principle. Electron in ground state is injected to u by resonant tunneling (RT), while separation between l and i' equals to LO phonon energy, fast electron-LO phonon scattering depopulate l making it almost unoccupied. Hence electron population in u is significantly more than population in l. Electrons in u can absorb a THz photon and transit to l, and then depopulated back into l' thus transport to next module by resonant tunneling. This extra channel after illuminating THz phonon leads to increase of current flow through the device making such scheme a photodetector.

LO phonon scattering efficiently depopulation l. Quantum well thickness should carefully chosen thus when l is efficiently depopulated, u have to in resonant with ground state of previous module making population in u is more than l. Such a transport is not possible for zero-bias QCDs. The electron-phonon lifetimes ($\tau_{l\rightarrow i'} \sim 0.2$ ps in Figure 5.4) in such superlattices could be made two orders of magnitude faster than other non-radiative transport mechanisms such as interface roughness and impurity scattering. This directly translates into a two orders of magnitude improvement in responsivity. This working principle make RP QCD different from "conventional" QWIPs and "conventional" QCD.

Although similar to QWIP, RPQCD is biased and have a large dark current, fundamental difference in electron transport leads different noise nature. For QWIPs excited electron finally escape to continuum, their transport described by classical

drift-diffusion model. A comprehensive analysis in current noise and photo noise in quantum cascade laser [110, 109] pointed that current noise in quantum tunneling transport for quantum cascade semiconductor superlattice is severely diminished. In QCL, spectral density $K_I(\omega)$ of the current noise, obeys a scaling relation with respect to the number of cascade gain stages N, derived as equation 111 in [110] this relation is

$$N^2 K_I(\omega, I/I_{th}, N) = N'^2 K_I(\omega, I/I_{th}, N') \tag{5.38}$$

according to above expression, current noise spectral density when expressed as a function of I/I_{th} scale with $1/N^2$. Since electron is not free when transport through superlattice, thus Johnson noise within the superlattice does not coupled to outside circuit. Hence, operating a RPQCD with a large dark current does not proportionally increase current noise in the circuit. The noise current is of the order of $\sqrt{2qI_{dark}\Delta f}/N$ instead of the typical value of $\sqrt{2qI_{dark}\Delta f}$for photodiode and QWIPs where Δf is the electrical bandwidth of the external measurement setup. Typical number of cascaded stage is about 200, thus the factor $1/N$ reduce current noise by two orders of magnitude.

In summary, qualitative analysis above showing that fast electron-phonon scattering can increase photocurrent thus responsivity $\mathcal{R}$ by two orders of magnitude, however large dark current by same mechanism does not increase current noise proportionally. Current noise is dumped by a factor of N due to quantum tunneling nature of electron transport where N is number of cascaded stage.

5.3.2 Intersubband selection rule, and gratings for normally incident photodetection

The formula derived in section 5.2.1, equation 5.14 shows that intersubband transitions only couple light whose polarization along semiconductor growth direction.

Maxwell equation require that polarization of electromagnetic field much normal to photon propagate direction, thus only light propagate parallel to growth plane can coupled into semiconductor superlattice. For intersubband semiconductor superlattice photodetector , photon can only coupled from facet. In Mid-IR QCD, people polish device facet to 45° to implement multi-pass geometry to increase absorption efficiency. However similar strategy is very difficult to apply on THz quantum cascade detector. THz photon have a typical free space wavelength of ~ 100 μm corresponding to ~ 28 μm in GaAs. It is impractical to growth such thick semiconductor superlattice, thus optical mode is confined in vertical direction by metal in sub-wavelength scheme. It is shown in [73] that due to sub-wavelength confinement in superlattice growth direction, facet reflectivity can more than 0.9. Thus external THz photon is very difficult to couple into metallic cavity. Besides weak optical coupling, focusing THz light on facet is also extremely challenge.

Rigid analysis showing that [118], devices with distributed feedback through second-order Bragg metal gratings allow strong emission normal to the metallic grating surface. Due to time reversal symmetry for propagation of electromagnetic wave second -order Bragg metal grating can also efficiently couple normal incident light back into cavity. Hence, second order Bragg diffraction grating can be used for normal incident THz photodetector.

Figure 5.5(a) is stem plot of eigen mode for 2^{nd} order DFB grating with 25 μm periodicity and 80 percent duty cycle. There is a photonic band gap of about 0.3 THz between 3.45 THz and 3.75 THz. The two modes closest to photonic band gap are fundamental longitudinal mode, their field distribution are illustrated in figure 5.5 (b) and (c). Lower photonic bandgap edge mode illustrated in 5.5(b) is also refer as non-radiative mode [140]. The term origin from the fact that if gratings repeated to infinity (physically equals to periodic boundary condition is applied), this mode does not radiate any electromagnetic wave to far field. Upper photonic bandgap edge

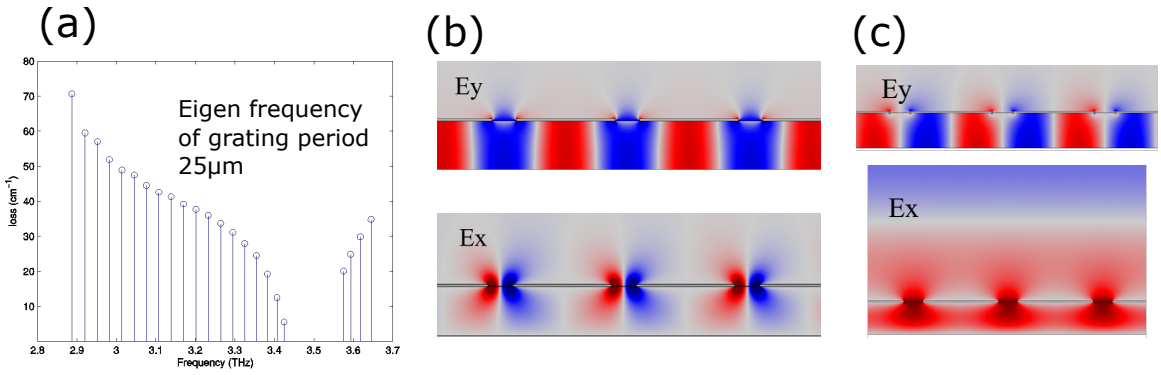

Figure 5.5: (a) Loss stem plot for eigen mode for 2^{nd} order Bragg gratings with grating period 25 μm and duty cycle of 0.8 calculated by COMSOL. Note that there is a photonic bandgap between 2.4 THz to 2.6 THz. (b) E_y (vertical direction) and E_x (horizontal direction) fields close to grating aperture for the lower photonic bandgap edge mode. (c)E_y (vertical direction) and E_x (horizontal direction) field intensity for the upper photonic bandgap edge mode.

mode showing in 5.5(c) is also refer as radiative mode, since E_x filed from every aperture constructively combined in far field.

For a THz QCL with 2^{nd} order Bragg diffraction grating without further photonic engineering, upper photonic band edge mode will not excited since its higher radiative loss make it less likely excited than lower photonic band edge mode. For a photodetector any mode showing in figure 5.5(a) can coupled some THz radiation back into metallic cavity. However coupling efficiency can have several orders of magnitude difference. Favorable mode which can couple normal incident light most efficiently is fundamental longitudinal mode showing in 5.5(b) and (c). The difference in radiation loss also make these two modes have different qualify factor and bandwidth. Qualify factor can be considered as number of oscillation a photon undergo in a cavity before escape. The higher radiation loss is , the lower quality factor will be. Since $\Delta f \propto \frac{1}{\text{Q}}$, higher band edge mode have larger bandwidth than lower band edge mode. The bandwidth of each mode that can lead to normal incident photon diffracted into active region is a major concern when aim to detect radiation from narrow bandwidth source like THz QCL. When QCL emission frequency does not lie within bandwidth

of any optical mode, incident light can not diffracted into photodetector active region.

5.3.3 Design of the superlattice active region

Borrowing the concept leads from temperature-robust THz QCLs [78], we design the THz QCD that utilizes resonant-tunneling assisted carrier injection and resonant-phonon assisted carrier depopulation and relaxation in the semiconductor superlattice.

The detail description of this active region is described in section 3.4. Electrical tuning due to intersubband absorption has already proofed that TUNDET202 design at corresponding bias as shown in figure 5.6 can absorb THz photon. The question remaining is whether photon response is large enough to detect under normal illumination condition. Another main focus of this work is proof that such detector capable work at enough high temperature which can achieve by using Stirling cryocooler instead of liquid helium.

5.4 Measurement Techniques and Experiments

To characterize RPQCD both broadband glow bar source or narrow band high intensity laser source are candidate. Practically narrow band THz QCL source have supreme advantage. Broadband thermal source have a very wide radiation angle and very low spectra power density. Focus such light on a small detector surface ($300\mu\text{m} \times 300\mu\text{m}$ need expensive off-axis parabolic mirror Also for demonstrated detectivity $5 \times 10^7 Jones$, broadband thermal source's emitted power is too low to detect. Thus a THz QCL named as RTRP2W102 is chosen as THz radiation source.

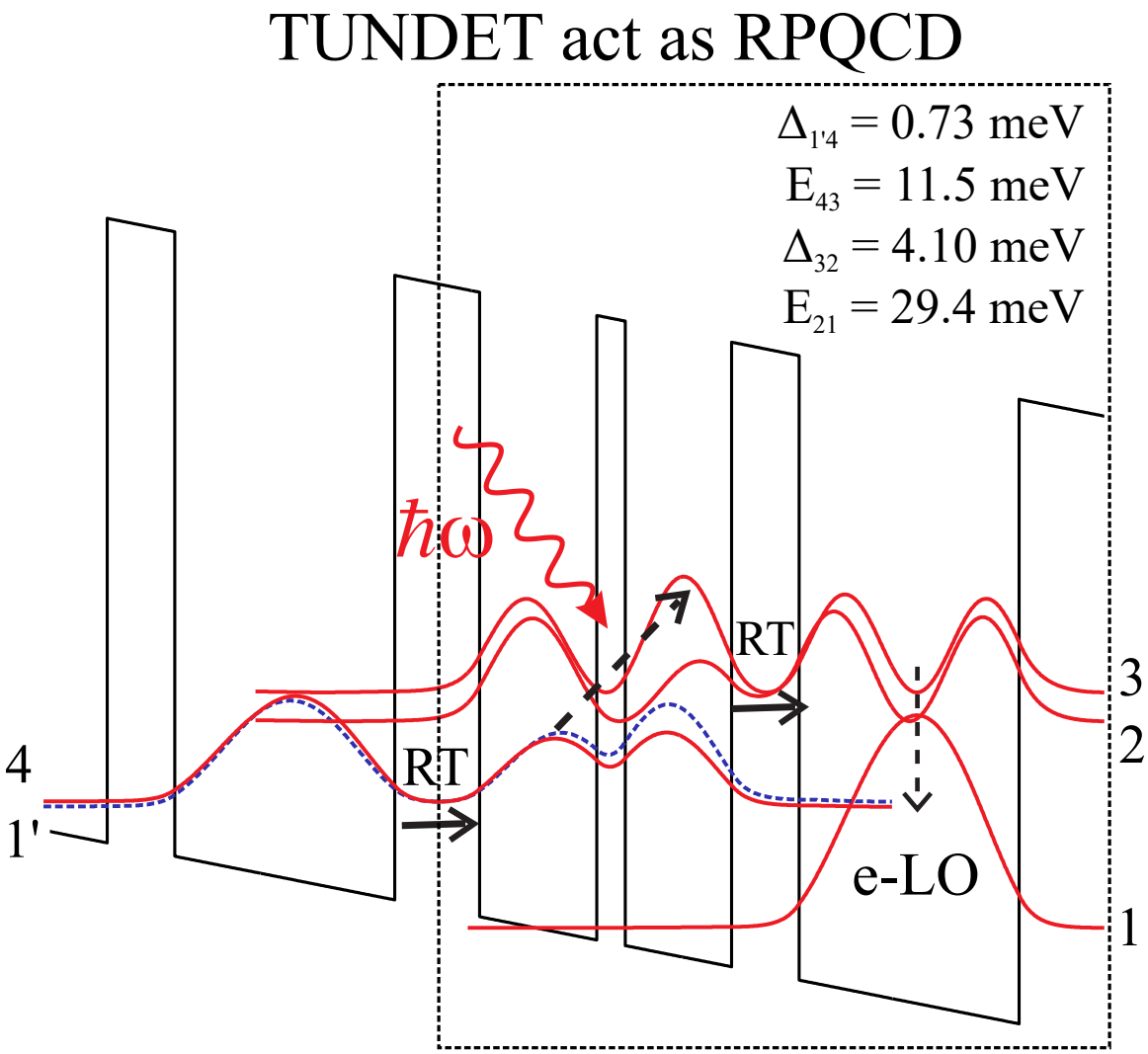

Figure 5.6: Conduction band diagram at bias corresponding to RPQCD type transport (18mV/module) for a THz QCL structure named TUNDET202. Starting from the injector barrier on the left, layer thicknesses for the GaAs/$Al_{0.3}Ga_{0.7}As$ superlattice in nm are 5.4/8.5/2.3/9.3/6.8/17.5. The average doping in the active region is 6×10^{15} cm^{-3}. At this bias, upper laser subband 4 is aligned to phonon subband 2 in depopulation well. Fast LO-phonon scattering depopulates the doublet resulting in intersubband absorption from $3 \rightarrow (2, 4)$, at a frequency that is detuned from QCL's emission frequency.

5.4.1 Characterization of THz QCL as a light source for the QCD

The design detail of this active region is beyond scope of this section and can be found in [65] A 120μm wide $\sim$ 1 mm long RTRP3W102 THz QCL ridge is mounted on a

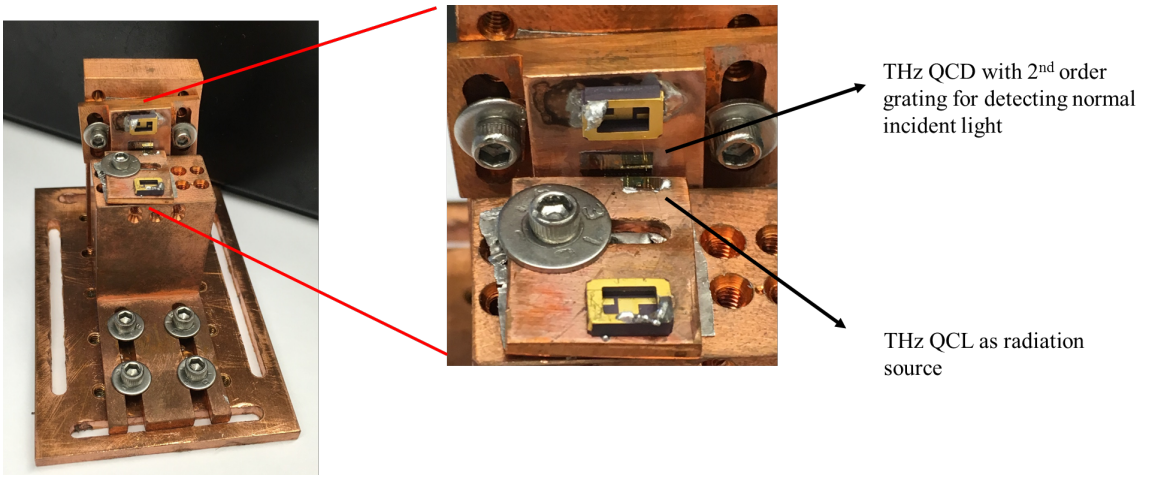

Figure 5.7: Designed copper mount for RPQCD detecting normal incident THz photon.

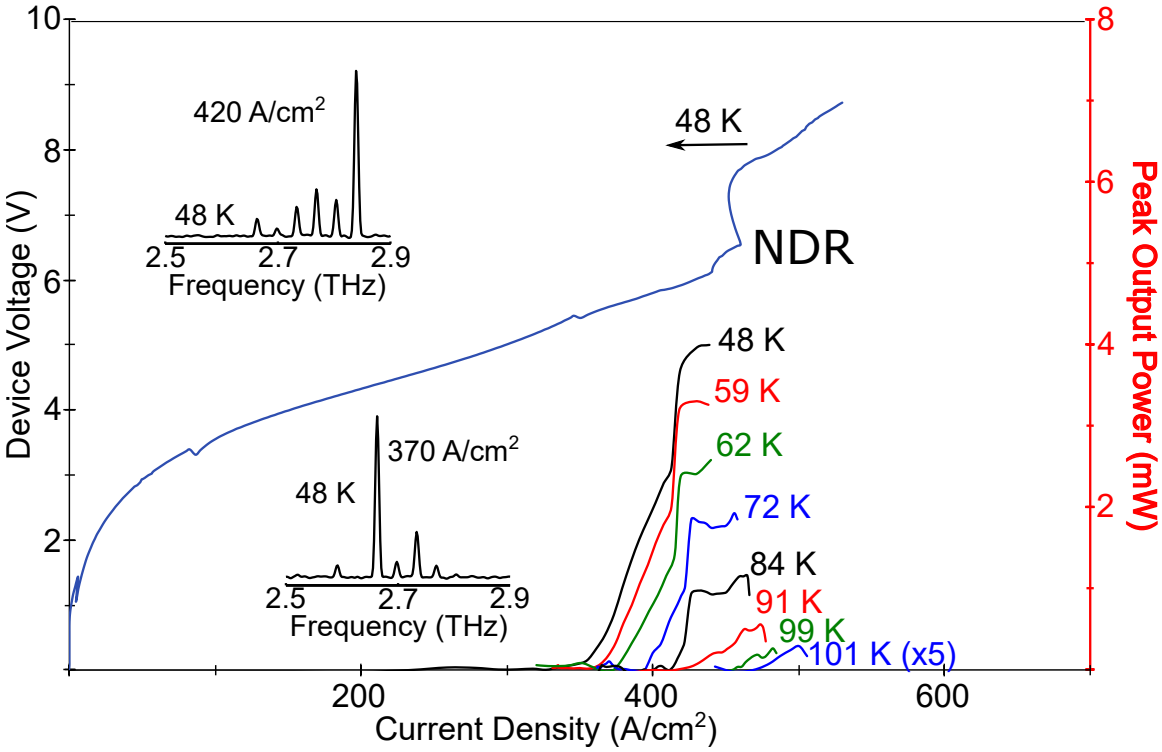

Figure 5.8: Pulsed IV, temperature dependent LI and spectra of RTRP3W102 design

copper chip with Indium. The device is cooled down to 48 K by a Stirling cryocooler. Threshold current density is $\sim 370\text{A/cm}^2$ while peak current density is $\sim 420\text{A/cm}^2$. At 48 K, peak output power in pulse mode is measured by a THz power meter is about 4 mW. From threshold to peak current density, the laser lase at multi-mode.

Around threshold current density, the main emission frequency is 2.65 THz while at around peak current density main peak is blue shift to about 2.85 THz.

5.4.2 New measurement technique for QCDs with large dark current

Density matrix analysis showing that photocurrent in design RPQCD is about 4-5 orders of magnitude smaller than dark current. Direct measurement of the photon response does not showing any response.

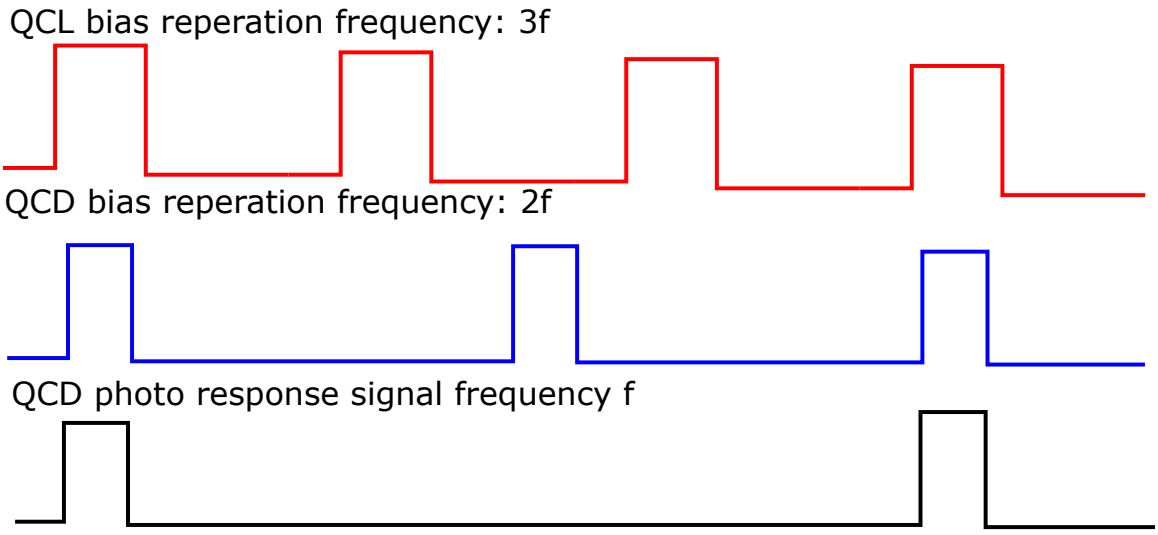

Figure 5.9: Measurement technique for RPQCD Photo Response. Photon response frequency is shifted away from dark current frequency

Without illuminate any THz radiation, current density flow through the device at QCD bias is in the order of 100A/cm^2. The photon response current density is in the order of mA/cm^2. This experiment aiming at capture increase in current density which is -100 dB small than noise. A straight forward solution is to shift signal frequency away from noise frequency and then use either filter or phase sensitive detection technique to measurement the signal at its frequency. Since QCL and QCD are all biased in pulse mode to minimize device heating and avoid electron become "hot" comparing to lattice temperature. QCL and QCD are biased by two synchro-

nized pulse train at different frequency, for example QCL is biased by a pulse whose repetition frequency is $3f$ while QCD bias's repetition rate is only $2f$. This the overlap of these two signal is only repeated by a frequency of f. By using this technique, QCD bias frequency (which is also dark current reparation rate) is shifted by f from QCD photon response time. Applying phase sensitive measurement technique thus trig a lockin amplifier whose bandwidth is only 0.02 Hz at frequency f, this technique able to detect single in an environment S/N down to -120 dB

Other signal processing steps may potentially further increase signal strength. Note that raw signal including noise at frequency $2f$ while signal's frequency is f. A low noise low pass filter whose cut off frequency is about f can efficiently filter noise away. Since our bias repetition rate is below 100 KHz, such kind low pass filter can made by only use passive components thus minimize the effect from LPF's own noise. Besides attenuation noise, amplifying signal itself may also leads to higher sensitivity measurement. However since amplifier is a active component, an amplifier with very low noise should carefully chosen to minimize its own noise which will finally contribute to total measurement noise.

5.4.3 Experimental results

QCL (RTRP3W102) and RPQCD are mounted as shown in figure 5.7. The whole set up then mount to copper cold tip of a Sunpower Stirling cryocooler and be cooled down to about ~ 48 K. QCL ridge is 1150 μm long and 120 μm wide. It is fabricated in metal-metal waveguide geometry. RPQCD has a surface area of 300 μm $\times$ 300 μm. Metal grating (Ti/Cu/Au) with a periodicity of 32 μm and duty cycle of 80% act as 2^{nd} order Bragg diffraction gratings. Before measure photon response pulsed IV of individual devices are measured with a pulse repetition rate of 100 KHz and pulse width of 200 ns.

The Figure 5.10 (a) illustrates pulsed IV for the QCL. Figure 5.10 (b) shows the

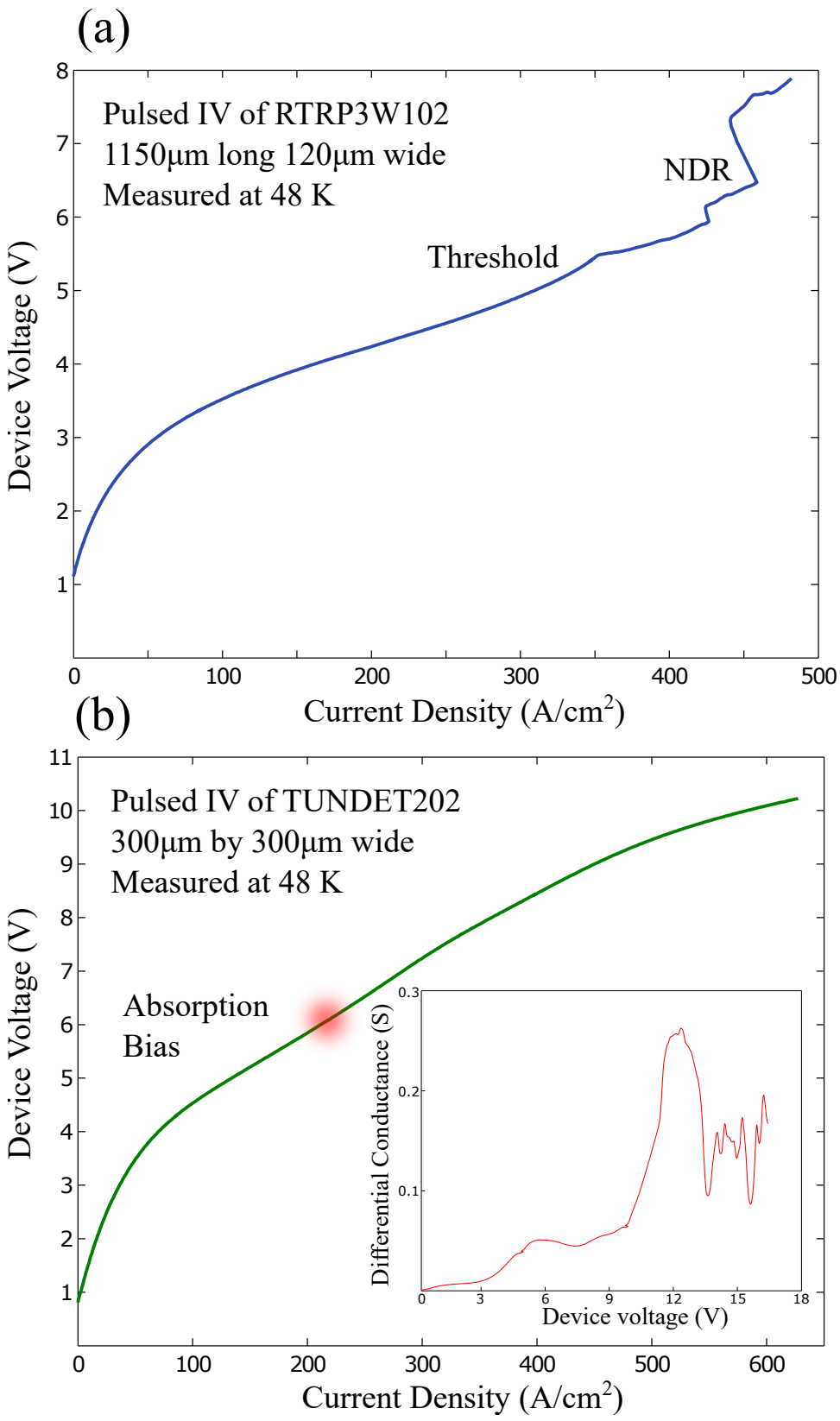

Figure 5.10: Pulsed IV and individual QCL and QCD

pulsed IV for QCD device, and the insert in (b) is differential conductance versus device voltage. This curve is related to quantum transport of certain design. The drop in a differential conductance peak corresponds to resonance of two subbands. For TUNDET202 design, first resonance of two subbands is illustrated in figure 5.6. The resonance corresponds to a device voltage between $6-8$ V This conductance peak is not very sharp due to small ($\sim$ 0.7 meV) anticrossing gap. Anticrossing gap measures interaction strength of two resonant subbands. Coherent resonant tunneling can be understood as a dumped oscillator. Carriers oscillate across potential barrier back and forth at Rabi frequency [73], the oscillation will be dumped by various scattering process. Rabi frequency is proportional to anticrossing gap $f_{\text{Rabi}} \propto \Delta_{\text{anticrossing}}/\hbar$. If Rabi frequency is much higher than total scattering rate, resonant tunneling will make carrier equally distributed between two subbands. Since anticrossing gap between subband 4 and subband $1'$ are not large enough, the drop in differential conductance curve is flat. Even though the drop is flat, absorption at desired frequency expect to be observed around $6-8$ V.

Photon response of QCD is measured in the way proposed in section 5.4.2. QCL is biased by a home made pulser with pulse train repetition rate of 90 KHz and pulse width of 500 ns. QCD is biased by AVTECH pulser at frequency of 60 KHz and pulse width of 300 ns.

Two types of measurement are performed. First QCD are fixed at different bias, QCL voltage is swept. Measurement result is showing in figure 5.11(a), start from about 6.5 V QCD have strong photo response. Photon current of QCD have two peaks when its bias is 10.82 V and 11.64 V respectively. Sharp peak in photon response eliminate the possibility that peak is due to electrical or thermal effect. During the experiments, QCD bias change from 5.6 V to about 8.4 V. Similar photon response curves are observed in all bias. It is clearly shown in figure 5.11(b) that photon response does not occur right after QCL start to lase. Second order Bragg diffraction

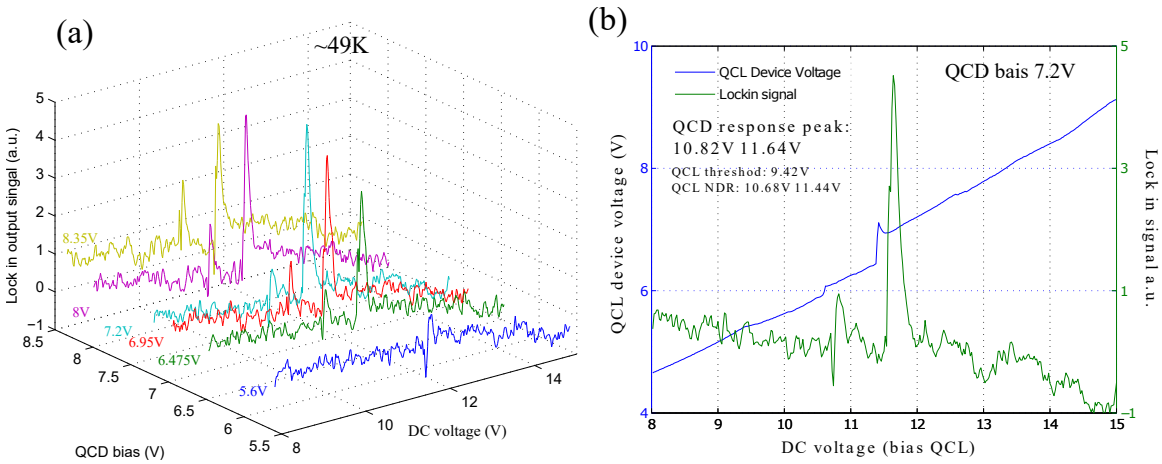

Figure 5.11: Photo response of RPQCD when QCD bias is fixed while QCL bias is swept.

gratings can explain observed result. Coupling frequency for different frequency can have server orders of magnitude difference. Emission frequency from QCL facet is depend on its bias. If at some bias QCL's emission frequency lie in bandwidth of any optical mode, part of incoming wave that coupled into QCD active region is significantly enhanced. QCD's photo response has two peaks when DC power supply

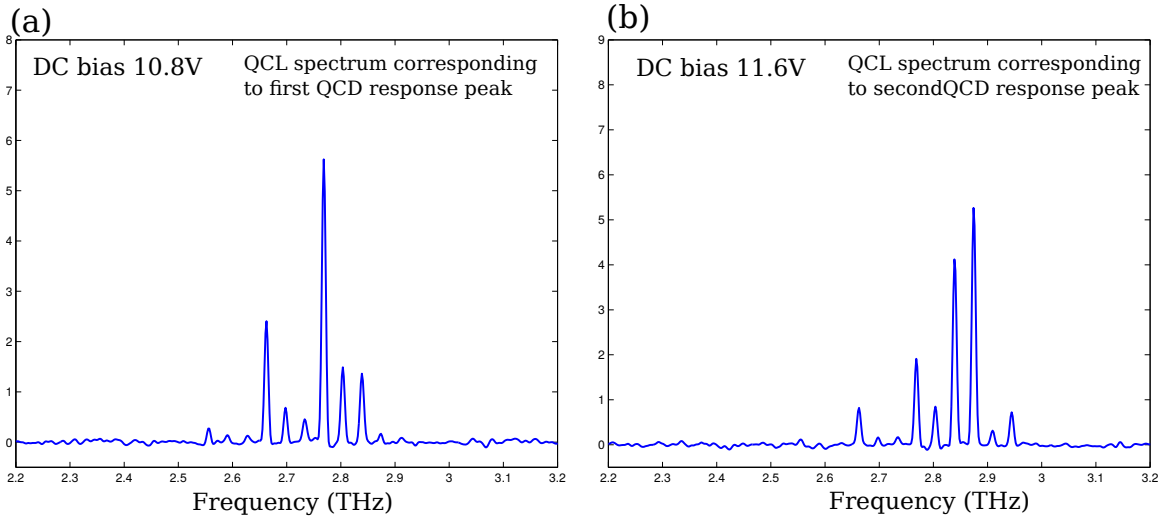

Figure 5.12: Spectrum of QCL at two bias where QCD have peak photo response

bias is 10.82 V and 11.64V. Figure 5.12 illustrated spectrum of QCL at 11.8V and 11.6V. The mode index for upper photonic band edge mode (field distribution shown in figure 5.5) simulated from 2D simulation is about $\sim$ 3.25. Thus resonant frequency

for upper photonic band edge mode is $\sim$ 2.87 THz. When DC power supply voltage is 11.6V, highest peak for QCL's emission frequency is lie between 2.8 THz to 2.9 THz, while when DC power supply voltage is 10.8V, highest emission frequency peak is below 2.8 THz however there are lower peak between 2.8 THz and 2.9 THz. Note that below upper photonic band edge mode frequency there is a photonic band gap of about 0.25 THz. Therefore part of incoming light that can coupled into active region is negligible if frequency lie in photonic band gap.

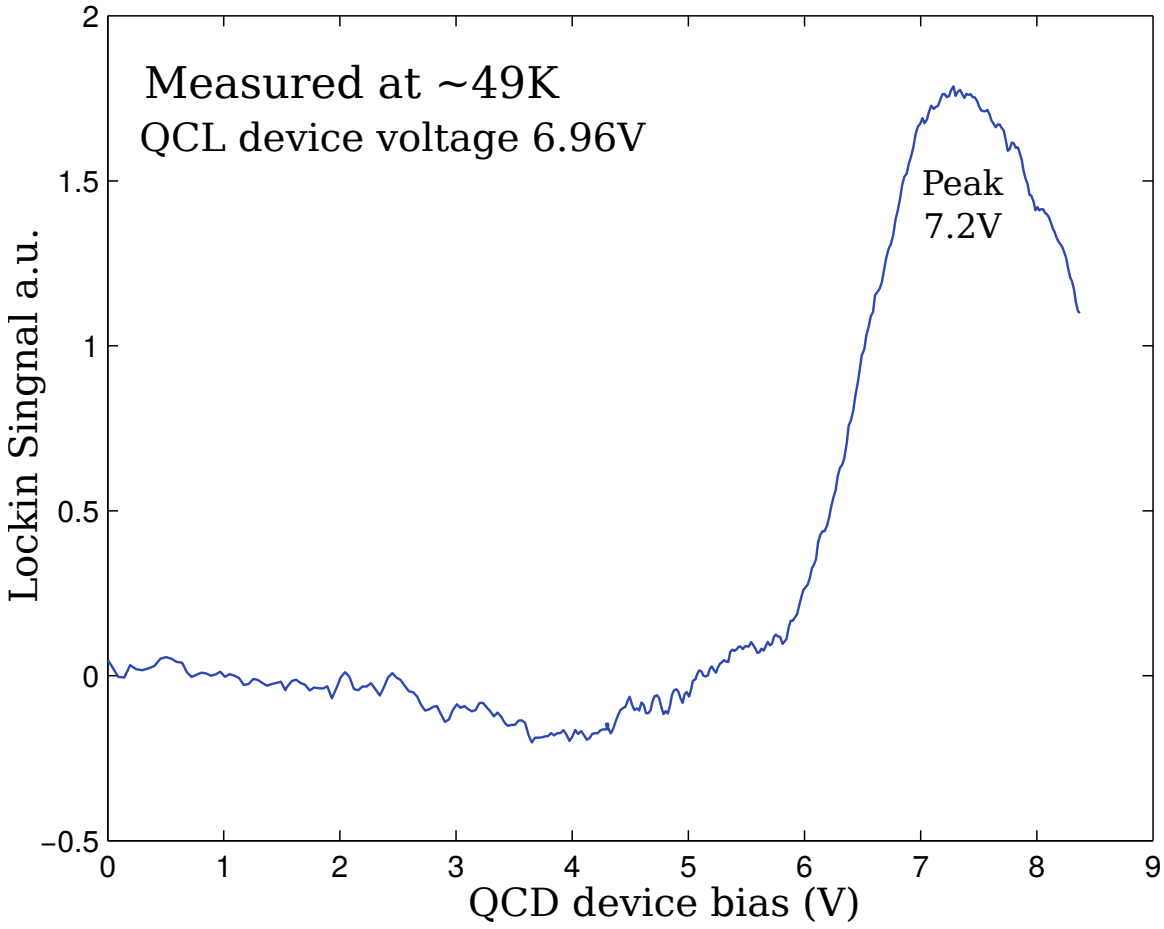

Figure 5.13: Photo response of RPQCD when QCL bias is fixed while QCD bias is swept.

Second type of measurement is done with fixed QCL bias. QCL's device bias is fixed to 7V while QCD's device bias change from 0V to about 8.5V. Figure 5.13 illustrate QCD's photo response curve. QCD start to have photo response when its

bias reach to about 6V. QCD has a peak response corresponding to its bias equals 7.2V. When further increase QCD bias its response from incident illumination start to decrease. The observed curve matches well with band diagram and differential conductance analysis. During all experiments temperature of the Stirling cryocooler's copper cold stage are monitored continuously. Temperature is increase slightly when either QCL or QCD bias is increased, however the variation of temperature is within 1 K.

5.5 Summary and Conclusions

A function generator generates a pulse train which has a repetition rate of 30 KHz and pulse width of 300 ns. The pulse train has an identical repetition rate and pulse width as that of photon response signal. When the current pulse has an amplitude of 100 mA, output from lockin amplifier has an amplitude of 1.722 mV. When QCD's photo response is at its peak, the amplitude of lockin amplifier output is about 2 μV. Because, lockin amplifier is considered to have a linear response with input signature's amplitude, we can estimate QCD's photo current to be 0.116 mA. To accurately measure the incident power reach QCD surface is very challenging, however, we can use a rough assumption which is all light coming out from QCL's facet reaches QCD surface. The output power at QCL's peak is 5 mW at 48 K. Under our bias condition, the duty cycle of QCL's bias is 4.5 percent, corresponding to an average output power of $\sim$ 230 μW. Thus, our QCD has a responsivity $\mathcal{R}$ of about 500 mA/W at 50 K. Since QCL's emitting aperture is deeply sub-wavelength with a height of 5 μm, the output beam shape should be really divergent. The assumption we use will lead to possibly a large underestimation of the QCD's responsivity.

In conclusion, a theoretical framework is developed in this thesis to analyze a THz quantum-cascade detector with the resonant-phonon depopulation scheme. The

proposed QCD design was grown by MBE and fabricated with metal-metal cavities. A measurement technique has been developed in order to extract small photocurrent signals from a large dark current, which is a characteristic of this type of photodetector. The measurement technique allows operation of the QCD in pulsed mode (i. e. continuous-wave operation is not required). The measure signal's amplitude could be several orders of magnitude smaller than the QCD's dark current. Although, promising preliminary results are demonstrated in this thesis, more work needs to be done done in order to show that such kinds of THz photodetector are suitable for highly sensitive THz detection (similar to liquid-Helium cooled bolometers) while still working at much higher temperatures (closer to that of liquid-Nitrogen).

Bibliography

[1] THz pyroelectric detectors Gentec [URL].

[2] COMSOL 4.4, a finite-element partial differential equation solver, (http://www.comsol.com).

[3] Quantun well infrared photodetector [URL].

[4] InSb hot electron bolometers QMC Instruments [URL].

[5] Silicon bolometers Infrared Laboratories [URL].

[6] Sunpower CryoTel GT [URL].

[7] A. J. L. Adam, I. Kašalynas, J. N. Hovenier, T. O. Klaassen, J. R. Gao, E. E. Orlova, B. S. Williams, S. Kumar, Q. Hu, and J. L. Reno. Beam patterns of terahertz quantum cascade lasers with subwavelength cavity dimensions. *Appl. Phys. Lett.*, 88:151105, 2006. [URL].

[8] T. Aellen, R. Maulini, R. Terazzi, N. Hoyler, M. Giovannini, J. Faist, S. Blaser, and L. Hvozdara. Direct measurement of the linewidth enhancement factor by optical heterodyning of an amplitude-modulated quantum cascade laser. *Appl. Phys. Lett.*, 89:091121, 2006.

[9] Doyeol Ahn. Calculations of hole–phonon scattering in strained-layer quantum wells. *Journal of applied physics*, 78(7):4505–4509, 1995.

[10] M. I. Amanti, M. Fischer, G. Scalari, M. Beck, and J. Faist. Low-divergence single-mode terahertz quantum cascade laser. *Nature Photonics*, 3:586–590, 2009. [URL].

[11] T. Ando, A. B. Fowler, and F. Stern. Electronic properties of two-dimensional systems. *Rev. Mod. Phys.*, 54:437, 1982.

[12] S. Barbieri, P. Gellie, G. Santarelli, L. Ding, W. Maineult, C. Sirtori, R. Colombelli, H. Beere, and D. Ritchie. Phase-locking of a 2.7-thz quantum cascade laser to a mode-locked erbium-doped fibre laser. *Nature Photonics*, 4:636, 2010.

[13] WA Beck. Photoconductive gain and generation-recombination noise in multiple-quantum-well infrared detectors. *Applied physics letters*, 63(26):3589–3591, 1993.

[14] A. L. Betz, R. R. Boreiko, B. S. Williams, S. Kumar, Q. Hu, and J. L. Reno. Frequency and phase-lock control of a 3 THz quantum cascade laser. *Opt. Lett.*, 30:1837, 2005.

[15] Stefan Birner, Tobias Zibold, Till Andlauer, Tillmann Kubis, Matthias Sabathil, Alex Trellakis, and Peter Vogl. Nextnano: general purpose 3-d simulations. *IEEE Transactions on Electron Devices*, 54(9):2137–2142, 2007.

[16] S Borri, P Patimisco, A Sampaolo, HE Beere, DA Ritchie, MS Vitiello, G Scamarcio, and V Spagnolo. Terahertz quartz enhanced photo-acoustic sensor. *Applied Physics Letters*, 103(2):021105, 2013.

[17] Markus Brandstetter, Tamara Sumalowitsch, Andreas Genner, Andreas E Posch, Christoph Herwig, Andreas Drolz, Valentin Fuhrmann, Thomas Perkmann, and Bernhard Lendl. Reagent-free monitoring of multiple clinically rele-

vant parameters in human blood plasma using a mid-infrared quantum cascade laser based sensor system. *Analyst*, 138(14):4022–4028, 2013.

[18] David Burghoff, Tsung-Yu Kao, Ningren Han, Chun Wang Ivan Chan, Xiaowei Cai, Yang Yang, Darren J Hayton, Jian-Rong Gao, John L Reno, and Qing Hu. Terahertz laser frequency combs. *Nat. Photonics*, 8(6):462–467, 2014.

[19] N. Butler, R. Blackwell, R. Murphy, R. Silva, and C. Marshall. Dual use, low cost microbolometer imaging system. *Proc. SPIE*, 2552:583, 1995.

[20] H. Callebaut. *Analysis of the electron transport properties in quantum cascade lasers*. PhD dissertation, Massachusetts Institute of Technology, Department of Electrical Engineering and Computer Science, 2006.

[21] H. Callebaut and Q. Hu. Importance of coherence for electron transport in terahertz quantum cascade lasers. *J. Appl. Phys.*, 98:104505, 2005. [URL].

[22] H. Callebaut, S. Kumar, B. S. Williams, Q. Hu, and J. L. Reno. Importance of electron-impurity scattering for electron transport in terahertz quantum-cascade lasers. *Appl. Phys. Lett.*, 84:645, 2004. [URL].

[23] F. Capasso, K. Mohammed, and A. Y. Cho. Sequential resonant tunneling through a multiquantum-well superlattice. *Appl. Phys. Lett.*, 48:478, 1986.

[24] Chun Wang I. Chan, Qing Hu, and John L. Reno. Ground state terahertz quantum cascade lasers. *Appl. Phys. Lett.*, 101:151108, 2012. [URL].

[25] Yia-Chung Chang and RB James. Saturation of intersubband transitions in p-type semiconductor quantum wells. *Physical Review B*, 39(17):12672, 1989.

[26] Yu-Chi Chang, Philip Wägli, Vincent Paeder, Alexandra Homsy, Lubos Hvozdara, Peter van der Wal, Joab Di Francesco, Nico F de Rooij, and Hans Peter

Herzig. Cocaine detection by a mid-infrared waveguide integrated with a microfluidic chip. *Lab on a Chip*, 12(17):3020–3023, 2012.

[27] Calvin Yi-Ping Chao and Shun Lien Chuang. Resonant tunneling of holes in the multiband effective-mass approximation. *Physical Review B*, 43(9):7027, 1991.

[28] AY Cho. Advances in molecular beam epitaxy (mbe). *Journal of crystal growth*, 111(1):1–13, 1991.

[29] S. L. Chuang. *Physics of Optoelectronic Devices*. Wiley Series in Pure and Applied Optics. John Wiley and Sons, New York, first edition, 1995.

[30] Luigi Consolino, Saverio Bartalini, Harvey E Beere, David A Ritchie, Miriam Serena Vitiello, and Paolo De Natale. Thz qcl-based cryogen-free spectrometer for in situ trace gas sensing. *Sensors*, 13(3):3331–3340, 2013.

[31] Andriy A Danylov, Alexander R Light, Jerry Waldman, Neal R Erickson, Xifeng Qian, and William D Goodhue. 2.32 thz quantum cascade laser frequency-locked to the harmonic of a microwave synthesizer source. *Optics express*, 20(25):27908–27914, 2012.

[32] G. Dehlinger, L. Diehl, U. Gennser, H. Sigg, J. Faist, K. Ensslin, D. Grützmacher, and E. Müller. Intersubband electroluminescence from silicon-based quantum cascade structures. *Science*, 290:2277, 2000. [URL].

[33] O. Demichel, L. Mahler, T. Losco, C. Mauro, R. Green, A. Tredicucci, J. Xu, F. Beltram, H. E. Beere, D. A. Ritchie, and V. Tamošinuas. Surface plasmon photonic structures in terahertz quantum cascade lasers. *Opt. Express*, 14:5335, 2006.

[34] Sukhdeep S Dhillon, Carlo Sirtori, Jesse Alton, Stefano Barbieri, Alfredo De Rossi, Harvey E Beere, and David A Ritchie. Terahertz transfer onto a telecom optical carrier. *Nature Photonics*, 1(7):411–415, 2007.

[35] Raymond Dingle, William Wiegmann, and Charles H Henry. Quantum states of confined carriers in very thin al x ga 1- x as-gaas-al x ga 1- x as heterostructures. *Physical Review Letters*, 33(14):827, 1974.

[36] L. A. Dunbar, R. Houdré, G. Scalari, L. Sirigu, M. Giovannini, and J. Faist. Small optical volume terahertz emitting microdisk quantum cascade lasers. *Appl. Phys. Lett.*, 90:141114, 2007.

[37] Mikhail Dyakonov and Michael Shur. Detection, mixing, and frequency multiplication of terahertz radiation by two-dimensional electronic fluid. *IEEE Transactions on Electron Devices*, 43(3):380–387, 1996.

[38] L Esaki and H Sakaki. New photoconductor. *IBM Tech. Discl. Bull*, 20(2456), 1977.

[39] J. Faist, F. Capasso, D. L. Sivco, C. Sirtori, A. L. Hutchinson, and A. Y. Cho. Quantum cascade laser. *Science*, 264:553–556, 1994. [URL].

[40] Jérôme Faist. *Quantum cascade lasers*. OUP Oxford, 2013.

[41] S. Fathololoumi, E. Dupont, C. W. I. Chan, Z. R. Wasilewski, S. R. Laframboise, D. Ban, A. Mátyás, C. Jirauschek, Q. Hu, and H. C. Liu. Terahertz quantum cascade lasers operating up to $\sim$ 200 K with optimized oscillator strength and improved injection tunneling. *Opt. Express*, 20:3866, 2012. [URL].

[42] J. F. Federici, B. Schulkin, F. Huang, D. Gary, R. Barat, F. Oliveira, and D. Zimdars. THz imaging and sensing for security applications–explosives, weapons, and drugs. *Semicond. Sci. Technol.*, 20:S266, 2005. [URL].

[43] R_ Ferreira and Gerald Bastard. Evaluation of some scattering times for electrons in unbiased and biased single-and multiple-quantum-well structures. *Physical Review B*, 40(2):1074, 1989.

[44] T Fromherz, E Koppensteiner, M Helm, G Bauer, JF Nützel, and G Abstreiter. Hole energy levels and intersubband absorption in modulation-doped si/si 1- x ge x multiple quantum wells. *Physical Review B*, 50(20):15073, 1994.

[45] Mikio Fujiwara, Takanori Hirao, Mitsunobu Kawada, Hiroshi Shibai, Shuji Matsuura, Hidehiro Kaneda, Mikhail Patrashin, and Takao Nakagawa. Development of a gallium-doped germanium far-infrared photoconductor direct hybrid two-dimensional array. *Applied optics*, 42(12):2166–2173, 2003.

[46] J. R. Gao, J. N. Hovenier, Z. Q. Yang, J. J. A. Baselmans, A. Baryshev, M. Hajenius, T. M. Klapwijk, A. J. L. Adam, T. O. Klaassen, B. S. Williams, S. Kumar, Q. Hu, and J. L. Reno. A terahertz heterodyne receiver based on a quantum cascade laser and a superconducting bolometer. *Appl. Phys. Lett.*, 86:244104, 2005.

[47] Laure Gendron, M Carras, Agnès Huynh, V Ortiz, C Koeniguer, and V Berger. Quantum cascade photodetector. *Applied physics letters*, 85(14):2824–2826, 2004.

[48] Laure Gendron, C Koeniguer, X Marcadet, and V Berger. Quantum cascade detectors. *Infrared physics & technology*, 47(1):175–181, 2005.

[49] Fabrizio R Giorgetta, Esther Baumann, Marcel Graf, Quankui Yang, Christian Manz, Klaus Kohler, Harvey E Beere, David A Ritchie, Edmund Linfield, Alexander G Davies, et al. Quantum cascade detectors. *IEEE Journal of Quantum Electronics*, 45(8):1039–1052, 2009.

[50] M. Graf, G. Scalari, D. Hofstetter, J. Faist, H. Beere, E. Linfield, D. Ritchie, and Giles Davies. Terahertz range quantum well infrared photodetector. *Appl. Phys. Lett.*, 84:475, 2004. [URL].

[51] Marcel Graf. *Design and characterisation of far-and mid-infrared quantum cascade detectors*. PhD thesis, Université de Neuchâtel, 2008.

[52] Richard P Green, Ji-Hua Xu, Lukas Mahler, Alessandro Tredicucci, Fabio Beltram, Guido Giuliani, Harvey E Beere, and David A Ritchie. Linewidth enhancement factor of terahertz quantum cascade lasers. *Applied Physics Letters*, 92(7):071106, 2008.

[53] X. G. Guo, J. C. Cao, R. Zhang, Z. Y. Tan, and H. C. Liu. Recent progress in terahertz quantum-well photodetectors. *IEEE J. Sel. Topics Quantum Electron.*, 19:8500508, 2013. [URL].

[54] M Hartig, S Haacke, B Deveaud, and L Rota. Femtosecond luminescence measurements of the intersubband scattering rate in al x ga 1- x as/gaas quantum wells under selective excitation. *Physical Review B*, 54(20):R14269, 1996.

[55] Alex Harwit and JS Harris Jr. Observation of stark shifts in quantum well intersubband transitions. *Applied Physics Letters*, 50(11):685–687, 1987.

[56] DJ Hayton, A Khudchenko, DG Pavelyev, JN Hovenier, A Baryshev, JR Gao, Tsung-Yu Kao, Qing Hu, JL Reno, and V Vaks. Phase locking of a 3.4 thz third-order distributed feedback quantum cascade laser using a room-temperature superlattice harmonic mixer. *Applied Physics Letters*, 103(5):051115, 2013.

[57] Manfred Helm. The basic physics of intersubband transitions. *Semiconductors and semimetals*, 62:1–99, 1999.

[58] Daniel Hofstetter, Mattias Beck, and Jérôme Faist. Quantum-cascade-laser structures as photodetectors. *Applied Physics Letters*, 81(15):2683–2685, 2002.

[59] Rita Claudia Iotti and Fausto Rossi. Nature of charge transport in quantum-cascade lasers. *Physical Review Letters*, 87(14):146603, 2001.

[60] J. H. Jiang and D. L. Wu. Ice and water permittivities for millimeter and sub-millimeter remote sensing applications. *Atmos. Sci. Let.*, 5:146, 2004. [URL].

[61] R Clark Jones. detectivity: the reciprocal of noise equivalent input of radiation. 1952.

[62] Deborah M Kane and K Alan Shore. *Unlocking dynamical diversity: optical feedback effects on semiconductor lasers*. John Wiley & Sons, 2005.

[63] RW Kelsall, RI Taylor, ACG Wood, and RA Abram. Matrix elements for hole-phonon scattering in a semiconductor quantum well. *Semiconductor Science and Technology*, 5(8):877, 1990.

[64] RW Kelsall, ACG Wood, and RA Abram. Phonon scattering and mobility of holes in a gaas/alas quantum well. *Semiconductor science and technology*, 6(9):841, 1991.

[65] S. Khanal. *Quantum Cascade Laser for THz Applications*. PhD dissertation, Lehigh University, Department of Electrical Engineering and Computer Science, 2016. to be published.

[66] S. Khanal, L. Zhao, S. Kumar, and J. L. Reno. Temperature performance of terahertz quantum-cascade lasers with resonant phonon active-regions. *J. Opt*, 16:094001, 2014. [URL].

[67] Sudeep Khanal, John L Reno, and Sushil Kumar. 2.1 thz quantum-cascade laser operating up to 144 k based on a scattering-assisted injection design. *Optics express*, 23(15):19689–19697, 2015.

[68] Sudeep Khanal, Le Zhao, John L Reno, and Sushil Kumar. Temperature performance of terahertz quantum-cascade lasers with resonant-phonon active-regions. *Journal of Optics*, 16(9):094001, 2014.

[69] Charles Kittel. *Introduction to solid state*. John Wiley & Sons, 1966.

[70] Wojciech Knap, Mikhail Dyakonov, Dominique Coquillat, Frederic Teppe, Nina Dyakonova, Jerzy Łusakowski, Krzysztof Karpierz, Maciej Sakowicz, Gintaras Valusis, Dalius Seliuta, et al. Field effect transistors for terahertz detection: physics and first imaging applications. *Journal of Infrared, Millimeter, and Terahertz Waves*, 30(12):1319–1337, 2009.

[71] S. Kohen, B. S. Williams, and Q. Hu. Electromagnetic modeling of terahertz quantum cascade laser waveguides and resonators. *J. Appl. Phys.*, 97:053106, 2005.

[72] R. Köhler, A. Tredicucci, F. Beltram, H. E. Beere, E. H. Linfield, A. G. Davies, D. A. Ritchie, R. C. Iotti, and F. Rossi. Terahertz semiconductor-heterostructure laser. *Nature*, 417:156–159, 2002. [URL].

[73] S. Kumar. *Development of terahertz quantum-cascade lasers*. PhD dissertation, Massachusetts Institute of Technology, Department of Electrical Engineering and Computer Science, 2007. to be published.

[74] S. Kumar. Recent progress in terahertz quantum cascade lasers. *IEEE J. Sel. Topics Quantum Electron.*, 17:38, 2011. [URL].

[75] S. Kumar, C. W. I. Chan, Q. Hu, and J. L. Reno. Two-well terahertz quantum-cascade laser with direct intrawell-phonon depopulation. *Appl. Phys. Lett.*, 95:141110, 2009. [URL].

[76] S. Kumar, C. W. I. Chan, Q. Hu, and J. L. Reno. A 1.8 THz quantum-cascade laser operating significantly above the temperature of $\hbar\omega/k_{\mathrm{B}}$. *Nature Physics*, 7:166, 2011. [URL].

[77] S. Kumar and Q. Hu. Coherence of resonant-tunneling transport in terahertz quantum-cascade lasers. *Phys. Rev. B*, 80:245316, 2009. [URL].

[78] S. Kumar, Q. Hu, and J. L. Reno. 186 K operation of terahertz quantum-cascade lasers based on a diagonal design. *Appl. Phys. Lett.*, 94:131105, 2009. [URL].

[79] S. Kumar, B. S. Williams, Q. Qin, A. W. M. Lee, Q. Hu, and J. L. Reno. Surface-emitting distributed feedback terahertz quantum-cascade lasers in metal-metal waveguides. *Opt. Express*, 15:113, 2007. [URL].

[80] Iman Kundu, Paul Dean, Alexander Valavanis, Li Chen, Lianhe Li, John E Cunningham, Edmund H Linfield, and A Giles Davies. Discrete vernier tuning in terahertz quantum cascade lasers using coupled cavities. *Optics express*, 22(13):16595–16605, 2014.

[81] L. Landau and E. Lifchitz. *Mecanique Quantique, Theorie Non Relativiste*, chapter 1, page 496. Harcourt Brace College Publishing, Fort Worth, first edition, 1967.

[82] A. W. M. Lee, B. S. Williams, S. Kumar, Q. Hu, and J. L. Reno. Tunable terahertz quantum cascade lasers with external gratings. *Opt. Lett.*, 35:910, 2010. [URL].

[83] S-C Lee and A Wacker. Theoretical analysis of spectral gain in a terahertz quantum-cascade laser: Prospects for gain at 1 thz. *Applied physics letters*, 83(13):2506–2508, 2003.

[84] B. F. Levine, C. G. Bethea, G. Hasnain, V. O. Shen, E. Pelve, R. R. Abbott, and S. J. Hsieh. High sensitivity low dark current 10 μm gaas quantum well infrared photodetectors. *Appl. Phys. Lett.*, 56:851, 1990.

[85] B. F. Levine, S. D. Gunapala, J. M. Kuo, S. S. Pei, and S. Hui. Normal incidence hole intersubband absorption long wavelength GaAs/$Al_xGa_{1-x}As$ quantum well infrared photodetectors. *Appl. Phys. Lett.*, 59:1864, 1991. [URL].

[86] BF Levine. Quantum-well infrared photodetectors. *Journal of applied physics*, 74(8):R1–R81, 1993.

[87] BF Levine, KK Choi, CG Bethea, J Walker, and RJ Malik. New 10 μm infrared detector using intersubband absorption in resonant tunneling gaalas superlattices. *Applied Physics Letters*, 50(16):1092–1094, 1987.

[88] BF Levine, RJ Malik, J Walker, KK Choi, and CG Bethea. Infrared intersubband absorption at 8.2 μm in doped superlattices of gaas/alas. In *Semiconductor Conferences*, pages 157–161. International Society for Optics and Photonics, 1987.

[89] BF Levine, A Zussman, SD Gunapala, MT Asom, JM Kuo, and WS Hobson. Photoexcited escape probability, optical gain, and noise in quantum well infrared photodetectors. *Journal of applied physics*, 72(9):4429–4443, 1992.

[90] BF Levine, A Zussman, JM Kuo, and J De Jong. 19 μm cutoff long-wavelength gaas/alxga1- xas quantum-well infrared photodetectors. *Journal of applied physics*, 71(10):5130–5135, 1992.

[91] H. C. Liu. Noise gain and operating temperature of quantum well infrared photodetectors. *Appl. Phys. Lett.*, 61:2703, 1992.

[92] HC Liu. Quantum well infrared photodetector physics and novel devices. *Semiconductors and semimetals*, 62:129–196, 1999.

[93] HC Liu, CY Song, AJ SpringThorpe, and JC Cao. Terahertz quantum-well photodetector. *Applied physics letters*, 84(20):4068–4070, 2004.

[94] Joaquin M Luttinger and Walter Kohn. Motion of electrons and holes in perturbed periodic fields. *Physical Review*, 97(4):869, 1955.

[95] Stephen Anthony Lynch, R Bates, DJ Paul, DJ Norris, AG Cullis, Z Ikonic, RW Kelsall, P Harrison, DD Arnone, and CR Pidgeon. Intersubband electroluminescence from si/sige cascade emitters at terahertz frequencies. *Applied physics letters*, 81(9):1543–1545, 2002.

[96] L. Mahler, A. Tredicucci, R. Köhler, F. Beltram, H. E. Beere, E. H. Linfield, D. A. Ritchie, and A. G. Davies. High-performance operation of single-mode terahertz quantum cascade lasers with metallic gratings. *Appl. Phys. Lett.*, 87:181101, 2005.

[97] O. Malis, L. N. Pfeiffer, K. W. West, A. M. Sergent, and C. Gmachl. Mid-infrared hole-intersubband electroluminescence in carbon-doped GaAs/AlGaAs quantum cascade structures. *Appl. Phys. Lett.*, 88:081117, 2006. [URL].

[98] Oana Malis, Loren N Pfeiffer, Kenneth W West, A Michael Sergent, and Claire Gmachl. Bound-to-bound midinfrared intersubband absorption in carbon-doped gaas/ algaas quantum wells. *Applied Physics Letters*, 87(9):091116, 2005.

[99] FP Mezzapesa, LL Columbo, M Brambilla, M Dabbicco, MS Vitiello, and G Scamarcio. Imaging of free carriers in semiconductors via optical feedback

in terahertz quantum cascade lasers. *Applied Physics Letters*, 104(4):041112, 2014.

[100] Daniel Mittleman. *Sensing with terahertz radiation*, volume 85. Springer, 2013.

[101] WJ Moore and H Shenker. A high-detectivity gallium-doped germanium detector for the 40–120μ region. *Infrared Physics*, 5(3):99–106, 1965.

[102] Sachiko Nakajima, Hiromichi Hoshina, Masatsugu Yamashita, Chiko Otani, and Norio Miyoshi. Terahertz imaging diagnostics of cancer tissues with a chemometrics technique. *Applied Physics Letters*, 90(4):041102, 2007.

[103] R. Nelander and A. Wacker. Temperature dependence of the gain profile for terahertz quantum cascade lasers. *Appl. Phys. Lett.*, 92:081102, 2008. [URL].

[104] K Ohtani, M Beck, and J Faist. Electrical laser frequency tuning by three terminal terahertz quantum cascade lasers. *Applied Physics Letters*, 104(1):011107, 2014.

[105] Vittorio MN Passaro, Benedetto Troia, M Notte, and F Leonardis. Chemical sensors based on photonic structures. 2011.

[106] Pietro Patimisco, Gaetano Scamarcio, Frank K Tittel, and Vincenzo Spagnolo. Quartz-enhanced photoacoustic spectroscopy: a review. *Sensors*, 14(4):6165–6206, 2014.

[107] GE Pikus and GL Bir. Symmetry and strain-induced effects in semiconductors. *J. Wiley, New York*, 1974.

[108] Q. Qin, B. S. Williams, S. Kumar, Q. Hu, and J. L. Reno. Tuning a terahertz wire laser. *Nature Photonics*, 3:732–737, 2009. [URL].

[109] Farhan Rana and Rajeev J Ram. Photon noise and correlations in semiconductor cascade lasers. *Applied Physics Letters*, 76(9):1083–1085, 2000.

[110] Farhan Rana and Rajeev J Ram. Current noise and photon noise in quantum cascade lasers. *Physical Review B*, 65(12):125313, 2002.

[111] P. L. Richards. Bolometers for infrared and millimeter waves. *J. Appl. Phys.*, 76:1, 1994.

[112] A. Rogalski. Infrared detectors: status and trends. *Prog. Quantum Electron.*, 27:59–210, 2003.

[113] Daryoosh Saeedkia. *Handbook of terahertz technology for imaging, sensing and communications*. Elsevier, 2013.

[114] Z Schlesinger, JCM Hwang, and SJ Allen Jr. Subband-landau-level coupling in a two-dimensional electron gas. *Physical review letters*, 50(26):2098, 1983.

[115] H Schneider. Optimized performance of quantum well intersubband infrared detectors: Photovoltaic versus photoconductive operation. *Journal of applied physics*, 74(7):4789–4791, 1993.

[116] Harald Schneider and Hui Chun Liu. *Quantum well infrared photodetectors*. Springer, 2007.

[117] C Schönbein, H Schneider, G Bihlmann, K Schwarz, and P Koidl. A 10 μm gaas/alxga1- xas intersubband photodetector operating at zero bias voltage. *Applied physics letters*, 68(7):973–975, 1996.

[118] M. Schubert and F. Rana. Analysis of terahertz surface emitting quantum-cascade lasers. *IEEE J. Quantum Electron.*, 42:257, 2006.

[119] Alexei Semenov, Oleg Cojocari, Heinz-Wilhelm Hubers, Fengbin Song, Alexander Klushin, and Anke-Susanne Muller. Application of zero-bias quasi-optical schottky-diode detectors for monitoring short-pulse and weak terahertz radiation. *IEEE Electron Device Letters*, 31(7):674–676, 2010.

[120] Peter H Siegel. Thz instruments for space. *IEEE Transactions on Antennas and Propagation*, 55(11):2957–2965, 2007.

[121] XH Su, J Yang, P Bhattacharya, G Ariyawansa, and AGU Perera. Terahertz detection with tunneling quantum dot intersublevel photodetector. *Applied physics letters*, 89(3):31117–31117, 2006.

[122] F. Szmulowicz. Derivation of a general expression for the momentum matrix elements within the envelope-function approximation. *Phys. Rev. B*, 51:1613, 1995. [URL].

[123] M. Tonouchi. Cutting-edge terahertz technology. *Nature Photonics*, 1:97–105, 2007. [URL].

[124] Dana Turčinková, Maria Ines Amanti, Fabrizio Castellano, Mattias Beck, and Jérôme Faist. Continuous tuning of terahertz distributed feedback quantum cascade laser by gas condensation and dielectric deposition. *Applied Physics Letters*, 102(18):181113, 2013.

[125] Dana Turčinková, Maria Ines Amanti, Giacomo Scalari, Mattias Beck, and Jérôme Faist. Electrically tunable terahertz quantum cascade lasers based on a two-sections interdigitated distributed feedback cavity. *Applied Physics Letters*, 106(13):131107, 2015.

[126] Takeya Unuma, Masahiro Yoshita, Takeshi Noda, Hiroyuki Sakaki, and Hidefumi Akiyama. Intersubband absorption linewidth in gaas quantum wells due to scattering by interface roughness, phonons, alloy disorder, and impurities. *arXiv preprint cond-mat/0208195*, 2002.

[127] Alex Valavanis, Paul Dean, Yah Leng Lim, Raed Alhathlool, Milan Nikolic, Russell Kliese, Suraj P Khanna, Dragan Indjin, Stephen J Wilson, Aleksan-

dar D Rakic, et al. Self-mixing interferometry with terahertz quantum cascade lasers. *IEEE Sensors Journal*, 13(1):37–43, 2013.

[128] A. Wacker. Transport in nanostructures: A comparison between nonequilibrium green functions and density matrices. *Adv. Solid State Phys.*, 41:199, 2001. [URL].

[129] A. Wacker, M. Lindskog, and D. O. Winge. Nonequilibrium green's function model for simulation of quantum cascade laser devices under operating conditions. *IEEE J. Sel. Topics Quantum Electron.*, 19:1200611, 2013. [URL].

[130] Eicke R Weber, RK Willardson, HC Liu, and Federico Capasso. *Intersubband transitions in quantum wells: physics and device applications*, volume 62. Academic press, 1999.

[131] L. C. West and S. J. Eglash. First observation of an extremely large-dipole infrared transition within the conduction band of a GaAs quantum well. *Appl. Phys. Lett.*, 46:1156–1158, 1985.

[132] Harald Willenberg, GH Döhler, and Jerome Faist. Intersubband gain in a bloch oscillator and quantum cascade laser. *Physical Review B*, 67(8):085315, 2003.

[133] B. S. Williams. *Terahertz quantum cascade lasers*. PhD dissertation, Massachusetts Institute of Technology, Department of Electrical Engineering and Computer Science, 2003.

[134] B. S. Williams. Terahertz quantum-cascade lasers. *Nature Photonics*, 1:517–525, 2007. [URL].

[135] B. S. Williams, S. Kumar, H. Callebaut, Q. Hu, and J. L. Reno. Terahertz quantum-cascade laser at $\lambda \approx 100$ μm using metal waveguide for mode confinement. *Appl. Phys. Lett.*, 83:2124, 2003. [URL].

[136] B. S. Williams, S. Kumar, Q. Hu, and J. L. Reno. Distributed-feedback terahertz quantum-cascade lasers with laterally corrugated metal waveguides. *Opt. Lett.*, 30:2909, 2005.

[137] C. Wu, S. Khanal, J. L. Reno, and S. Kumar. Single-mode thz quantum cascade lasers with ultra-narrow beam pattern. *presented at the International Quantum Cascade Lasers School and Workshop 2014, Policoro, Italy, Sept. 7–12*, 2014.

[138] Chongzhao Wu, Sudeep Khanal, John L Reno, and Sushil Kumar. Terahertz plasmonic laser radiating in an ultra-narrow beam. *arXiv preprint arXiv:1604.04977*, 2016.

[139] B Xing, HC Liu, PH Wilson, M Buchanan, ZR Wasilewski, and JG Simmons. Noise and photoconductive gain in algaas/gaas quantum well intersubband infrared photodetectors. *Journal of applied physics*, 76(3):1889–1894, 1994.

[140] G. Xu, R. Colombelli, S. P. Khanna, A. Belarouci, X. Letartre, L. Li, E. H. Linfield, A. G. Davies, H. E. Beere, and D. A. Ritchie. Efficient power extraction in surface-emitting semiconductor lasers using graded photonic heterostructures. *Nature Comm.*, 3:952, 2012. [URL].

[141] R. Q. Yang, J. M. Xu, and M. Sweeny. Selection rules of intersubband transitions in conduction-band quantum wells. *Phys. Rev. B*, 50:7474, 1994. [URL].

[142] A. Yariv. *Quantum Electronics*. John Wiley & Sons, New York, USA, 3 edition, 1989.

[143] Hailiang Zhang, Karen Siegrist, Kevin O Douglas, Susan K Gregurick, and David F Plusquellic. Thz investigations of condensed phase biomolecular systems. *Methods in cell biology*, 90:417–434, 2008.

[144] Hua Zhang, Giacomo Scalari, Jérôme Faist, L Andrea Dunbar, and Romuald Houdré. Design and fabrication technology for high performance electrical pumped terahertz photonic crystal band edge lasers with complete photonic band gap. *Journal of Applied Physics*, 108(9):093104, 2010.

[145] L Zhao, L Gao, and S Kumar. Resonant-tunneling transport of holes in terahertz GaAs/AlGaAs quantum cascade superlattice (submitted). In *OSA Proceedings on Advanced Solid-State Lasers*. Washington, DC: Optical Society of America, 2016.

[146] Le Zhao and Sushil Kumar. Design of a hole-based thz intersubband laser. In *Laser Science*, pages LW5G–3. Optical Society of America, 2013.

Vita

Le Zhao received the B.E degree from HuaZhong University of Science and Technology, Wuhan, China, in 2010, and M.S. degree from Lehigh University, Bethlehem, Pennsylvania. The bachelor degree is in Electronic Science and Technology and the master degree is in Physics. He will receive his Ph.D. degree in electrical engineering from Lehigh University, Bethlehem, Pennsylvania at September 2016.

His research focuses on intersubband transitions based devices for THz applications. He work on both theoretical and experimental aspects.